Metamaterials for Decoupling Antennas and Electromagnetic Systems

by

Mohammed M. Bait-Suwailam

A thesis
presented to the University of Waterloo
in fulfillment of the
thesis requirement for the degree of
Doctor of Philosophy
in
Electrical and Computer Engineering

Waterloo, Ontario, Canada, 2011

I hereby declare that I am the sole author of this thesis. This is a true copy of the thesis, including any required final revisions, as accepted by my examiners.

I understand that my thesis may be made electronically available to the public.

Abstract

This research focuses on the development of engineered materials, also known as *meta-materials*, with desirable effective constitutive parameters: electric permittivity ϵ_{eff} and magnetic permeability μ_{eff} to decouple antennas and noise mitigation from electromagnetic systems. An interesting phenomenon of strong relevance to a wide range of problems, where electromagnetic interference is of concern, is the elimination of propagation when one of the constitutive parameters is negative. In such a scenario, transmission of electromagnetic energy would cease, and hence the coupling between radiating systems is reduced. In the first part of this dissertation, novel electromagnetic artificial media have been developed to alleviate the problem of mutual coupling between high-profile and low-profile antenna systems. The developed design configurations are numerically simulated, and experimentally validated. In the mutual coupling problem between high-profile antennas, a decoupling layer based on artificial magnetic materials (AMM) has been developed and placed between highly-coupled monopole antenna elements spaced by less than $\lambda/6$, where λ is the operating wavelength of the radiating elements. The decoupling layer not only provides high mutual coupling suppression (more than 20-dB) but also maintains good impedance matching and low correlation between the antenna elements suitable for use in Multiple-Input Multiple-Output (MIMO) communication systems. In the mutual coupling problem between low-profile antennas, novel sub-wavelength complementary split-ring resonators (CSRRs) are developed to decouple microstrip patch antenna elements. The proposed design configuration has the advantage of low-cost production and maintaining the profile of the antenna system unchanged without the need for extra layers. Using the designed structure, a 10-dB reduction in the mutual coupling between two patch antennas has been achieved.

The second part of this dissertation utilizes electromagnetic artificial media for noise mitigation and reduction of undesirable electromagnetic radiation from high-speed printed-circuit boards (PCBs) and modern electronic enclosures with openings (apertures). Numerical results based on the developed design configurations are presented, discussed, and compared with measurements. To alleviate the problem of simultaneous switching noise (SSN) in high-speed microprocessors and personal computers, a novel technique based on cascaded CSRRs has been proposed. The proposed design has achieved a wideband suppression of SSN and maintained a robust signal integrity performance. A novel use of electromagnetic bandgap (EBG) structures has been proposed to mitigate undesirable electromagnetic radiation from enclosures with openings. By using ribbon of EBG surfaces, a significant suppression of electromagnetic radiation from openings has been achieved.

Acknowledgements

In the name of God the merciful, and the giver of mercy... First of all, I am thankful to God Almighty for giving me the strength, patience, and health to accomplish this thesis work...

Second, I am very lucky in working with a great supervisor, Prof. Omar Ramahi. I would like to express my sincere gratitude to Prof. Ramahi for his friendship, expert advice, support and patience through the course of this work. I can not thank him enough for his guidance and friendly assistance that helped me improve my technical skills and academic knowledge. I believe that having discussions with him is a peerless privilege.

I owe a debt of gratitude to my committee members Prof. Kostadinka Bizheva, Prof. Safavi-Naeni, and Prof. Slim Boumaiza for their dedication and time spent on reviewing my dissertation and providing invaluable comments. I greatly appreciate the time they devoted and their sincere advices. I would like to thank Prof. Mohamed Bakr for accepting the invitation to serve on my committee as the external faculty member. I am grateful to him and appreciate his time, valuable comments, and feedback.

I extend my deepest appreciation to my dear parents Atselom and Mana. I am grateful to my parents and apologize to them for being away all this period. Thanking them is not even enough for all what they have done to me and are still doing. I pray to God to shower his blessings and mercy on my parents, give them endless health and strength, and grant them paradise... I also thank my brothers and sisters for their faithful love, endless advices, and patience. I would always be indebted to them. I would also like to thank my wife, Wafa'a, for her love, encouragement, and patience during the lengthy journey taken. She has always been in my side. For sure, my two lovely sons, Salem and Mana, have made me go deeply through the course of this work, despite the tough times that one faces at some points during research work.

I would like to thank all my colleagues and friends in the microwave and electromagnetics research group at the University of Waterloo. I am glad to work with such a friendly, active, and collaborative group. I would like to thank Dr. Omar Siddiqui, Dr. Muhamed Boybay, Dr. Leila Yousefi, Dr. Babak Alavikia, Dr. Hussein Attia, Dr. Ali Kabiri, Zhao, Mehrbod Mohajer, Wael Abdelwahab, George Shaker, Dr. Mohamed Fakhrzadeh, Bayam, Mohammed Al-Shareef, Ali AlBishi, and special thanks to Na'el Suwan. I would also like to thank Prof. Hussain Al-Rizzo for his motivations and fruitful discussions. During my stay in Waterloo, I have been gifted with lots of true friends whom I will never forget the moments that I shared with them. I would like to thank: Dr. Shubair's family, Faisal Harriri, Hassan Al-Reasi, Issam Bahdoor, Rashid Al-Abri,

Dr. Mohamed Al-Badi, Suhail Al-Dharab, Fawaz Al-Sulami... My apology goes to those whom I did not include in this acknowledgment. They will always be in my heart.

This research was supported by my employer, Sultan Qaboos University. Without their financial support, this work would be extremely hard to accomplish.

***To my* parents,**

and

***memory of my brother* Salem**

Table of Contents

List of Tables

List of Figures

Chapter 1

Introduction

1.1 Motivation

Compactness and low-weight have become a highly desirable features in an antennas' design. In practice, more than one antenna is used to improve the performance of the antenna system. The mutual interaction between the antenna elements, known as mutual coupling, is a physical complex phenomena that describes the reaction between coupled antenna elements in a system. Although existence of mutual coupling can be of advantage to many antenna arrays (i.e., Yagi-Uda antenna arrays), such coupling is undesirable in many wireless communication devices nowadays. This mutual interaction between coupled antenna elements in an array will decrease the performance of the antenna system when the antennas are in close-proximity to each other. The degraded performance appears in the lack of maintaining good impedance match and hence waste of the incident power to the antenna system. Furthermore, the mutual coupling disturbs the far-field pattern of the antenna system due to the destructive interferences between the coupled antenna elements. As such, reduction of electromagnetic coupling or interference between the individual antenna elements becomes a challenging design task.

Mutual coupling is a common problem in antenna design, and it significantly affects most types of radiating systems. The study of the mutual coupling problem started several decades ago, and tremendous research efforts have been devoted to combat the mutual coupling between coupled antennas, not just from antenna engineers, but also from other disciplines such as communications where multiple antennas are frequently encountered, like in Multiple-Input Multiple-Output (MIMO) systems. MIMO systems provide a number of advantages over single-antenna communication by employing multiple antenna elements at both transmitter and receiver sides of the communication system.

MIMO systems take an advantage of the environment to transmit signals through multiple channels [4]-[5]. For example, sensitivity to fading or environment obstacles is reduced by the spatial diversity provided by multiple spatial channel paths. Usually antenna elements need to be spaced far apart in order to have suitable isolation and low correlation between the elements in order to exploit independence of signal channels in MIMO systems [5]-[6]. However, degradation would result upon placing the antenna elements in close proximity due to near-field effects, diffraction from finite-ground planes, strong inductive and capacitive coupling between the radiating elements, in addition to other sources of coupling (e.g. surface waves...etc) depending on the employed antenna system [6]. Therefore the performance of MIMO systems in terms of signal to noise ratio (SNR) and achieved diversity can be significantly affected when the antenna elements are in close proximity [5]-[7].

Mutual coupling also distorts the behavior of radiating elements in antenna arrays. Each element in an array affects every other element by radiating through the free-space or by propagating surface currents along the chassis or ground plane that eventually changes the current distribution of the neighboring elements. As a result, antenna gain, pattern, resonance frequency, and input impedance are all affected. Furthermore, in large planar phased antenna arrays, mutual coupling degrades the performance of phased antenna arrays for beam scanning [8]. In fact, a common problem known as scan blindness occurs due to the excitation of surface waves on the grounded dielectric slab and the coupling between individual antenna elements of the array. This scan blindness can be defined as the phenomena where significant dip results in the total active pattern of the phased antenna array (or sever mismatch in input impedance of the array) at certain scan angles [8]. At such scan blindness, no real power is coupled to or radiated by the antenna array due to the existence of surface waves that are trapped in the grounded dielectric slab and carry no real power.

The increased complexity and speed of electronic products have dramatically led to an increase of the amount of electromagnetic interference (EMI) and radiated emissions [9]. These EMI disturbances arise as a result of high-frequency clock or data signal with sharp rise/fall edges in addition to other several sources of noise. The noise degrades the performance and integrity of high-speed printed-circuit (PCBs) boards, microprocessors of personal computers (PCs), and laptop devices. Nowadays, with the continuous downscaling of integrated circuits, and the increasing clock frequency in modern microprocessors, a source of noise, known as *simultaneous switching noise* (SSN), has become a major concern for EMC engineers [10]-[11]. When many active devices switch at the same time, the switching noise generated can cause fluctuations or disturbances in the

power distribution system, which in turn leads to malfunction of analog circuits and a degradation of the signal integrity [11]. The coupling effects of this switching noise to other sensitive devices can be explained as follows. Electromagnetic fields generated by the switching device use the parallel-plate PCB board and travel radially along the board. These fields couple to nearby vias, and continue to propagate into the PCB edges. As a consequence, the energy coupled by the vias affects nearby idle devices (i.e., devices subject to noise), while part of this energy diffract and start to radiate once reaching the PCB edges. Eventually the radiated fields cause EMI and radiation problems [12]. Moreover, part of the energy that bounces back and forth from PCB edges gives rise to power plane resonances.

Recently, there has been tremendous research efforts in the development and use of novel electromagnetic artificial media, also termed *metamaterials*. These materials are engineered structures based on resonant (nonmagnetic) inclusions that can be periodic or aperiodic with properties not readily found in naturally occurring materials. This dissertation work presents novel use of metamaterials in two practical challenging applications: the first part covers the novel use of metamaterials designed to decouple antenna systems for wireless local area network applications (**Chapters 4** and **5**). The second part introduces novel techniques based on metamaterials for noise and electromagnetic radiation mitigation from high-speed PCBs and enclosures with openings, which are widely seen in modern personal computers, workstations, and laptop devices (**Chapters 6** and **7**).

1.2 Dissertation Contributions

The research work reported in this dissertation provides several advancements in terms of analytical modeling of metamaterials, novel design techniques applied to decouple antenna systems, and noise mitigation from modern electromagnetic systems. The contributions are summarized below.

A decoupling layer based on artificial magnetic materials (AMMs) is developed to alleviate the mutual coupling effects encountered between high-profile antenna systems. The designed decoupling layer is placed between highly-coupled monopole antenna elements. The decoupling layer not only provides high mutual coupling suppression but also maintains good impedance matching. This is achieved with very small separation distance between the elements of less than $\lambda/6$, where λ is the operating wavelength of the antenna elements.

Novel sub-wavelength complementary split ring resonators (CSRRS) are proposed to decouple low-profile antenna systems. The new designed unit cell consists of two CSRR

inclusions connected by an additional slot. This modification improves the rejection response in terms of bandwidth and suppression. The nature of these inclusions rely on etching out copper from metallic planes, thus resulting in low-cost production and maintaining the profile of the antenna unchanged without the need for extra layers.

Analytical models for general sub-wavelength CSRRs are proposed for the first time. The complementary resonators are the dual counterparts of the artificial magnetic materials. The analytical models give good engineering estimates for the effective permittivity of the sub-wavelength complementary inclusions. The analytical models has also the advantage of providing engineers with design recipes when using such complementary inclusions in many engineering applications.

A Novel technique based on cascaded CSRRs are proposed for wideband noise mitigation from power planes in personal computers and laptop devices. The designed structure is modeled and validated against experimental prototypes. The proposed novel technique overcomes many of the previously published approaches in noise mitigation from power planes of high-speed PCB boards in terms of noise mitigation bandwidth and suppression level, production cost, and signal integrity robustness.

The potential of the perforated power planes (i.e., power planes with CSRRs) for electromagnetic radiation is experimentally investigated. This novel design is suggested for use in next-generation integrated circuits packaging systems.

A Novel use of electromagnetic bandgap (EBG) structures, a subclass of metamaterials, is proposed for reduction of undesirable electromagnetic radiation from metallic screens and shielded enclosures with openings. A practical case study from real-world environment is presented, and measurements are conducted to validate the proposed concept.

1.3 Dissertation Outline

The remaining of this dissertation can be outlined as follows. **Chapter 2** gives a comprehensive background on various sources of coupling and noise in antenna systems and sub-systems. Previous trends and methodologies used to combat such threats are discussed, and the proposed techniques in this research work are highlighted.

Chapter 3 covers metamaterials and advanced structures, that will be utilized later in the context of this thesis work for decoupling antenna systems and mitigating noise and undesirable radiated emissions from high-speed electronic devices. **Chapter 3** starts

with an overview of existing engineered structures, *electromagnetic band gap* (EBG) structures, with emphasis on their design methodology and numerical characterization. Then, the development of a class of artificial materials, known as *artificial magnetic materials* (AMMs), is presented. The numerical model and retrieval procedure for extraction of the constitutive parameters ϵ and μ of the developed AMMs is discussed. Furthermore, another class of artificial materials, known as *complementary split-ring resonators* (CSRRs), is introduced. Such complementary structures are the dual-counterpart of AMMs in terms of the resultant response of constitutive parameters. In other words, while the artificial magnetic materials provide enhanced magnetic permeability when exposed to an axial time-varying magnetic field, the CSRRs result in enhanced electric permittivity when excited with a normal time-varying electric field. The analytical models for CSRRs are proposed, which gives the response of the electric permittivity ϵ. The proposed analytical models are compared with full-wave numerical simulations.

Chapter 4 presents applications of artificial magnetic materials to decouple highly coupled high-profile monopole antennas. The performance of the decoupling layer is assessed by measuring the coupled energy between the antenna elements and compared with a reference case (no decoupling layer between antenna elements). The performance of the antenna system is also evaluated with emphasis on MIMO systems. The advantages of the decoupling technique for electromagnetic interference problems is also illustrated by studying the near-field profile for the antenna systems with and without AMMs.

Chapter 5 presents applications of sub-wavelength complementary resonators to decouple low-profile patch antenna elements. A novel designed unit cell is developed and characterized using dispersion analysis and constitutive retrieval procedure. The designed unit cells require only etching out patterns from the ground plane. Hence, this topology is easy to manufacture and practical to integrate with microwave circuits. The mutual coupling in microstrip patch antenna systems is studied numerically and experimentally.

The second part of this thesis covers two applications of metamaterials related to the area of electromagnetic interference/compatibility (EMI/EMC). Particular emphasis is devoted to investigate the sources of noise and undesirable electromagnetic radiation in high-speed printed circuit boards (PCBs) and modern shielding equipment with openings.

In **Chapter 6**, novel and cost effective technique based on CSRRs is proposed for simultaneous switching noise mitigation. Both full-wave numerical studies and measurements are presented, discussed, and compared. Possible radiated emissions from the perforated boards are experimentally investigated. The robustness of the proposed technique is evaluated with the assessment of the eye diagrams.

Chapter 7 addresses cost-effective shielding techniques based on novel use of EBG

structures to mitigate electromagnetic field leakage from enclosures and apertures. Full-wave numerical studies are presented and compared with practical case studies from real-world environment.

Finally, an overview summary of this dissertation work, contributions, and suggested potential research directions are summarized in **Chapter 8**.

Chapter 2

Background

2.1 Sources of Coupling in Antenna Systems

2.1.1 Sources of coupling in high-profile antenna systems

High-profile antenna systems are referred to antennas in which their profile is comparable with the operating wavelength λ of the radiating elements, for example monopole and helical antennas, among others. These high-profile antennas are in contrary to the counterparts *low-profile* antennas, like microstrip antennas and planar inverted F antennas (PIFAs), among others.

When mounting multiple antenna elements near each others, some of the energy of one particular antenna is picked up by the other elements. The amount of the mutually interchanged energy depends mainly on the radiation characteristics of each antenna, separation between the antenna elements, and the immediate environment [6]. Due to the nature of the current distribution on high-profile monopole antennas, a magnetic field circulates around the antennas, leading to radiation into free-space, and possibly to nearby elements (antenna element B shown in Fig. 2.1). That interchange of energy is known as the *mutual coupling*. Although the impedance can be tuned and/or optimized, the mutual coupling still remains as a bottleneck that deteriorates the performance of the antenna system.

Due to the influence of the mutual coupling, antennas placed in close-proximity would alter the current distribution and in turn the input impedance of the antennas. With no mutual coupling, the input impedance of an antenna is equal to its self-impedance. However, with another antenna nearby, the input impedance becomes dependent on not only its self-impedance but also the mutual impedance and the currents on both antennas.

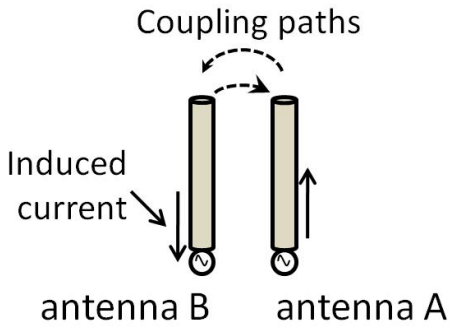

Figure 2.1: Illustration of transmitting mode coupling paths between antenna A and B.

To simplify the aforementioned analysis, this impedance relation can be expressed as

$$Z_{in} = Z_{11} + Z_{21}\frac{I_2}{I_1}, \tag{2.1}$$

where Z_{11} and Z_{21} are the self and mutual impedances respectively, and I_1 and I_2 refer to the input current of the respective antenna elements. For two half-wavelength dipole antennas, the mutual impedance referring to the input terminals of antenna 1 (i.e., antenna A in Fig. 2.1) can be expressed using the induced EMF method as [13]-[14]

$$Z_{21i} = \frac{V_{21}}{I_{1i}} = -\frac{1}{I_{1i}I_{2i}}\int_{-l/2}^{l/2} E_{z21}(z^{'})I_2(z^{'})dz^{'}, \tag{2.2}$$

where E_{z21} is the electric field component radiated by antenna 1 that is parallel to antenna 2, l is the electrical length of the wire antenna, I_{1i} and I_{2i} are the currents at the input terminals of antenna elements 1 and 2, respectively. Fig. 2.2 depicts the mutual impedance between two quarter-wavelength monopole antennas mounted over an infinite ground plane as a function of normalized separation distance, d/λ, where λ is the operating wavelength of the radiating elements. As the separation distance increases, the mutual impedance diminishes. Therefore, the performance of the antenna array remains fairly unaffected due to the minimal effects of mutual coupling when antenna elements are spatially spaced apart. However, in the worst case scenario (for example, d/λ <0.25), performance of the antenna systems in terms of maximal power accepted by the antenna systems and gain of such systems deteriorates resulting in less gain that has direct impact on signal to noise ratio (SNR). In many wireless communication applications, the elements of antenna arrays are placed in close-proximity, and as such it is of great importance to reduce the mutual coupling to have minimal effects on the performance of the antenna system.

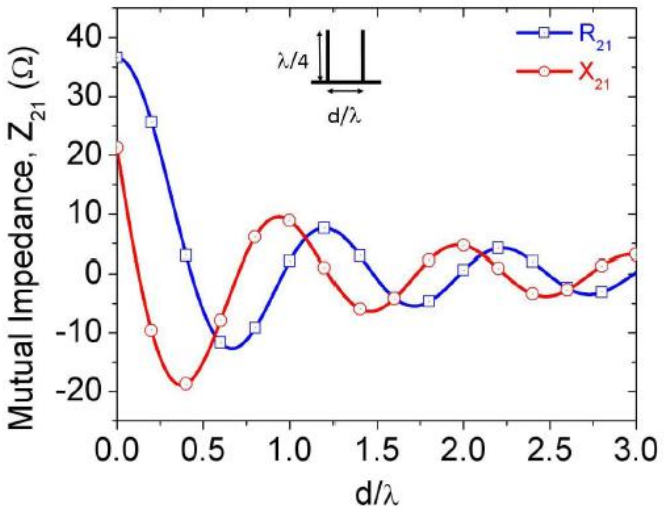

Figure 2.2: Mutual impedance Z_{21} between two vertical monopole antennas placed over an infinite chassis as a function of normalized distance between the antenna elements d/λ.

Maxwell's Equations for a non-dispersive and isotropic medium are given as

$$\nabla \cdot \mathbf{E(t)} = \frac{\rho}{\epsilon} \tag{2.3}$$

$$\nabla \cdot \mathbf{H(t)} = 0 \tag{2.4}$$

$$\nabla \times \mathbf{E(t)} = -\mu \frac{\partial \mathbf{H(t)}}{\partial t} \tag{2.5}$$

$$\nabla \times \mathbf{H(t)} = \mathbf{J(t)} + \frac{\partial \mathbf{D(t)}}{\partial t} \tag{2.6}$$

where, $\mathbf{E}$ is the electric field, $\mathbf{H}$ is the magnetic field, $\mathbf{J}$ is the current density, ρ is the electric charge density, ϵ is the permittivity of the medium, μ is the permeability of the medium, and the term $\frac{\partial \mathbf{D(t)}}{\partial t}$ is the displacement current. This current is another source of strong mutual coupling in high-profile radiating systems. Such a current can exist in many types of matter, even in free-space. To have more physical insights into that kind of current, consider having two coupled antennas and spatially spaced in free-space. I introduce here the *coupling path* term, as shown in Fig. 2.3, in order to account for the mutual coupling between the antennas and the current path through the displacement current. Such a current finds the path between the radiating antenna elements an attractive way to flow through, although no physical charges seem to exist within that free-space surrounding the two antennas. That current path also strongly couples the antenna elements, and within which a magnetic field exists around the path between the antennas. This coupling path is indeed critical in high-profile antennas. Therefore, mitigating it through the use of an appropriate synthesis technique or introducing a de-

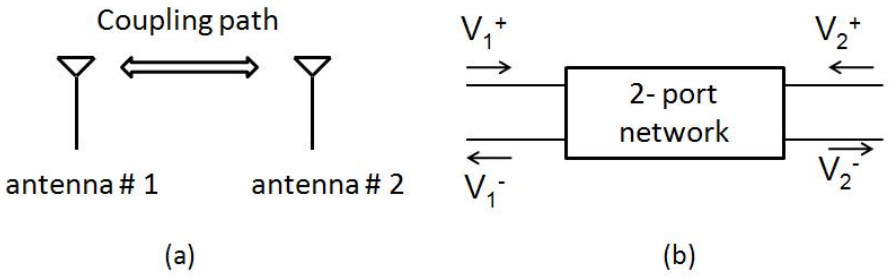

Figure 2.3: (a) Representation for the coupling path between two high-profile radiating elements and (b) its schematic network model.

coupling network is desirable in many applications. A decoupling layer will be introduced later in this dissertation to alleviate the mutual coupling problem between high-profile antennas.

2.1.2 Previous work on decoupling high-profile antennas

In this subsection, an overview of previous methodologies and decoupling techniques used to decouple high-profile antenna systems is provided. Each technique has its own advantage and disadvantage depending on the employed decoupling network. Anderson *et al.* [15] introduced the possibility of connecting a lossless transmission line network between the decoupling network input ports and the antenna elements ports such that no coupling between antennas is encountered. It was shown in Anderson's work [15] that antenna mutual impedances should be purely reactive at the antennas resonance in order to realize a decoupling network and hence isolate the antenna elements when placed close to each others. Other methods have also been suggested [16]-[17], where transmission lines were used as antenna decouplers. Although the capacitive decouplers work well, they are inherently narrowband, and limited by the antenna bandwidth.

An alternate way of reducing the electromagnetic coupling between radiating and/or receiving antenna elements sharing a common ground plane or chassis is to introduce resonant defects or slits in the ground plane [18]-[19]. A pair of quarter-wavelength slits etched on a finite ground plane [18] was used to reduce the mutual coupling effect in a closely spaced monopole antennas. With the slotted ground plane, almost 15-dB reduction in the mutual coupling was achieved over the reference (solid) ground plane at the antennas resonance frequency. A pair of half-wavelength resonant slots were used to alleviate the mutual coupling between two high-profile monopole antennas [19]. Higher suppression of mutual coupling was achieved in [19] over the solid ground plane, however, at the cost of distorted pattern and electrically large slots. In summary, by proper choice

of slits dimensions and shapes, the slits resonate and can trap some of the energy between the radiating elements.

Another mechanism proposed previously to isolate highly-coupled monopole antenna elements is to employ 180° hybrid couplers [17], [20]-[21]. This method is based on the mode-decomposition network, in which a multi-port network is inserted between the antennas and their driven ports. The decoupling is achieved by isolating the antennas radiation modes, after which the modes can be matched and driven individually through circuit ports. It is worthwhile mentioning here that this particular decoupling technique isolates the coupling at the network ports, but does not implicitly imply that the antennas are physically decoupled. By employing multi-modes to achieve orthogonal patterns, the hybrid couplers serve as a decoupling candidate to achieve pattern diversity.

Recently, electromagnetic artificial media, such as electromagnetic bandgap structures and alike, have been used extensively for many applications, including decoupling antenna systems [22]-[24]. Ferrer *et al.* introduced [22] the idea of using capacitively loaded loop (CLL) magnetic resonators in order to decorrelate two monopole antennas. Although the coupling had been reduced in [22], the antenna elements were not well-matched. In [23]-[24], a decoupling layer based on artificial magnetic metamaterials (the modified split-ring resonator (M-SRR) inclusions [25]) was developed to reduce the mutual coupling between highly-coupled high-profile monopole antennas. Higher suppression of mutual coupling was achieved in [24] in comparison to Ferrer's work [22].

2.1.3 Sources of coupling in low-profile antenna systems

Microstrip patch antennas are widely used in airbone and wireless communications due to their low profile, low weight, and ease of integration with other microwave devices. In principle, the microstrip patch antenna is a resonant type antenna, where the antenna size is determined by the operating wavelength. Microstrip patch antennas have low gain, and in practice an array of several antenna elements is used for applications requiring high gain. However, the performance of such antennas tend to deteriorate due to the mutual interaction between the antenna elements.

Fig. 2.4 depicts the possible coupling paths and mechanisms encountered in low-profile microstrip antenna systems. The sources of mutual coupling between low-profile microstrip patch antennas can be categorized into three main categories:

- near-field coupling;
- surface wave coupling;

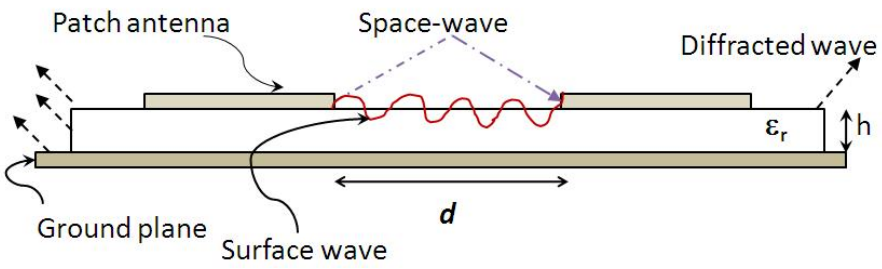

Figure 2.4: Model representation for sources of coupling in low-profile microstrip antenna systems.

- space-wave coupling.

The near-field coupling arises when an antenna is placed in the near-field zone of another antenna [26]. The electromagnetic fields in this region are dominantly reactive and decay very fast when antennas are further apart. Moreover, the near-field coupling is strong in situations where the antennas are printed on dielectric substrates with very low permittivity [26]-[27]. In this case, the wavelength in the substrate is very close to the free-space wavelength, and this type of coupling can result in severe degradation to the antenna's radiation characteristics.

Patch antennas are typically known to launch surface wave modes, as dielectric slabs do. These surface waves are guided by the substrate and ground plane (see Fig. 2.4), and propagate along the dielectric-air interface with an exponential decay away from the interface. The power lunched into surface wave modes will eventually be lost, and thus lowers the radiation efficiency of the microstrip patch antenna. Surface waves are strongly excited when antennas are printed on substrates with high permittivity and/or thicker substrates [28]-[29]. For such configurations, these type of waves dominate and result in strong mutual coupling between antenna elements, since surface waves decay slowly with radial distances and can travel to several wavelengths [28]. On the other hand, surface waves are not significant when antennas are printed in electrically thin substrates [8]. In general, surface waves have minimal effects subject to the following condition [30]

$$\frac{h}{\lambda} < \frac{0.3}{2\pi\sqrt{\epsilon_r}}, \tag{2.7}$$

where h is the substrate thickness, λ is the operating wavelength of the radiating antenna, and ϵ_r is the substrate's dielectric constant. An overview of surface wave modes which exist on dielectric slabs is studied and provided in Appendix B. While surface waves are weakly excited in very thin grounded dielectric substrates, another source of coupling, known in the literature as *space-waves* dominates [8], [28]. These space-waves have electric

field components that are normal to the dielectric substrate, which contribute to radiated power into space. Unfortunately, part of this space-waves power is lost due to the coupling effects between radiating elements when considering for example an antenna array printed in a very thin dielectric slab [8]. Space-wave coupling increases as well when antennas are in the near-field zone, wherein the normal electric field components couple from one antenna element to another, due to the fringing fields from the radiating slots of the antenna elements. This space-wave coupling will be shown later in this thesis to have dominant effects and a novel technique to reduce such coupling mechanism will be provided in Chapter 5. Fig. 2.4 summarizes the aforementioned sources of coupling that could entirely or partially exist in low-profile antenna systems. The effects of such sources of coupling would depend mainly on the properties of the dielectric slab and its thickness, spacing between the antenna elements, and ground plane size.

2.1.4 Previous work on decoupling low-profile antennas

The earliest theoretical and experimental studies on mutual coupling between microstrip antennas dates back to the early 80's [31]-[34]. The transmission line (TL) model was the first analytical technique to employ in analyzing rectangular microstrip antennas by Munson [31]-[33]. In the TL model, the interior region of the patch antenna is modeled as two radiating slots separated by a transmission line. Later on, an improved TL model was developed in [32] that accounts for the mutual coupling between the radiating edges of rectangular microstrip antennas by adding a mutual admittance connected between the two ends of the transmission line. Measured data for the mutual coupling between rectangular microstrip antenna elements were first reported in 1979 [34]. The TL model is easy to implement, but have some limitations, for example the model is restricted to thin substrates, ignores the width between the radiating slots [32] and surface waves effects, amongst others. To overcome some of the TL limitations, the cavity model was used to analyze mutual coupling in microstrip antennas [35]-[36].

The increased interest in the use of microstrip antennas in today's technology requires analysis methods that are accurately able to analyze microstrip antennas and able as well to fully account for all the mutual coupling effects. Tremendous efforts over the past fifty years were devoted to exploit fast full-wave numerical techniques for microstrip patch antenna problems [37]-[38]. In [37], a numerical technique based on the method of moment was used to solve for the current distribution and input impedance of a single microstrip antenna. In [35], the mutual coupling between microstrip antennas was calculated using the method of moments with cavity model. Pozar [38] applied a similar technique with Green's function used for the dielectric slab beneath the patch antenna

to rigorously account for surface waves losses and coupling interaction between antenna elements. In summary, analytical and experimental attempts in the past had mainly focused on analyzing and predicting the mutual coupling between microstrip radiators with no efforts to decouple such radiators. In the following, an elaborative survey on methodologies and techniques proposed by various research groups to combat the mutual coupling effects is discussed.

Several synthesis techniques had been reported in the literature for mutual coupling reduction between microstrip antennas [28], [39]. In the work of Jackson *et al.* [28], two variations of a circular microstrip patch design were proposed that excite very little surface waves. By proper design of the circular rings radius, the dominant TM_0 surface wave mode will not be excited in such antennas, and hence have reduced mutual coupling among the antenna elements, due to the reduced surface-wave excitation [39]. Alternative syntheses techniques were proposed by a number of authors [40]-[42] in order to compensate for the mutual coupling in closely-spaced low-profile antenna systems by introducing some additional coupling paths between the radiators. This can be done with a combination of capacitance and inductance effects by means of several slots and/or inductive strips, however, at the expense of narrowband suppression.

Another technique to isolate coupling in low-profile antennas is to use multimode antennas [43]-[44]. The deployment of multimode antennas results in independent radiation characteristics that are generated using several distinct modes. Those modes can be excited using a single antenna structure [43], like biconical or frequency-independent antennas. However, such multimode antenna structures are electrically large and result in a large antenna size in order to excite multiple higher-order modes. Another alternative of achieving orthogonal patterns is to excite several modes as well but using multiple ports [44], for example using a stack-up of several patch antennas. This type of decoupling technique is useful to achieve radiation-pattern diversity, in which the received signals are weighted independently using the radiation patterns of the modes, however, at the cost of fabrication.

Electromagnetic band-gap (EBG) structures, first introduced by Sievenpiper *et al.* [45], had been utilized to mitigate surface waves between low-profile microstrip patch antennas [46]-[50]. In [46]-[47], the mushroom-like electromagnetic band gap (EBG) structures were used, however, the structures involved plated-through-holes (vias) which are not attractive from the electric loss and manufacturing perspective. In [48], planar EBG structures were used in eliminating the need for vias; however, incurring the complexity and cost of using two dielectric layers. An alternative planar EBG structure, known as soft surface, first introduced by Kildal [51], was used in [49] to reduce the coupling be-

tween patch antennas at the expense of increased inter-element distance between antenna elements. In [50], planar EBG structures were used as well but as a superstrate placed on top of the antenna system layer. These type of covers (superstrates) incur complexity and substantial increase in the profile of the antenna system.

A technique was proposed [27], [52] to reduce the mutual coupling. It relies on machining or grooving the dielectric below the radiating antenna elements. Silicon micromachining has been adopted in [52] to reduce surface wave effects. However, the dielectric walls can cause diffracted electric fields which will significantly disturb far field radiation patterns. Although coupling was reduced, no far-field analysis was provided to quantify the superiority of the proposed technique. In [27], the effect of polarization currents within the substrate was compensated for by printing an array of shorting pins between the patch and the ground. However, this topology is tedious, and increases design complexity and fabrication process.

Several papers in the literature have introduced resonant defects or slits on a ground plane for coupling reduction between planar radiating systems [53]-[55]. In [53], mutual coupling between PIFA antennas suspended in free-space over a common ground plane was reduced using a pair of $\lambda/4$ slits. A pair of quarter-wavelength slits etched in finite ground plane was also used [18] to reduce the mutual coupling effect in a closely packed patch antennas. With the slotted ground plane, almost 10-dB reduction in the mutual coupling was achieved over the reference (solid) ground plane at the antennas resonance frequency. In [55], a quarter-wavelength slot etched in a ground plane was used to reduce mutual coupling between planar antenna elements. The achieved reduction in mutual coupling was around 6-dB. In summary, with proper slits dimensions, the defected ground plane resonate and can trap some of the energy between the radiating elements.

Recently, artificial magnetic materials (AMMs) had been utilized to reduce the mutual coupling in microstrip antenna arrays [56]-[57]. In the work of Buell *et al.* [56], spiral resonators were embedded within the dielectric substrate. Furthermore, similar loading of artificial magnetic materials using spiral resonators was adopted [57], where two individual (separated) microstrip antenna elements were loaded with such resonators. Although one do not expect any surface waves coupling among such isolated antenna elements, no physical explanation was provided for the coupling mechanism. In summary, loading substrates with artificial materials involve an intricate fabrication process and increase losses in the antenna system. In [58], a novel technique has been proposed to decouple low-profile microstrip antenna elements. The decoupling technique is based on miniaturized complementary split-ring resonators (CSRRs) which are the dual counterparts of AMMs. The CSRRs are etched out from a finite ground plane underneath the patch antenna

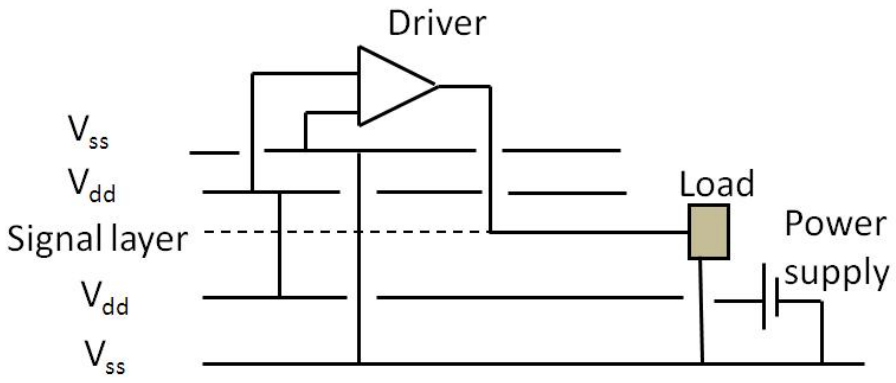

Figure 2.5: Schematic representation for the nature of switching noise in a multilayer PCB.

elements. Thus, this topology is cost effective and at the same time maintains the antenna structure low-profile.

2.2 Sources of Noise in Electromagnetic systems

In this section, potential sources of noise in modern high-speed printed circuit boards (PCBs) are discussed. Those sources, if uncontrolled, can lead to malfunction of analog circuits and performance degradation of digital electronic systems. Previous methodologies and techniques used to mitigate such sources of noise are then summarized.

2.2.1 Sources of noise in printed circuit PCB boards

Current microprocessors and computers utilize multi-layer printed circuit boards (PCBs) in order to provide both a packaging functionality and a power distribution network for the components [59]. These PCBs consist of multiple metal layers, separated by dielectric substrates. As illustrated in Fig. 2.5, the power distribution network is usually distributed over several metal layers, where the minimum requirement is to have one metallic layer for the *supply voltage*, denoted here as V_{dd}, and another layer works as a *reference voltage* (ground), referred to as V_{ss}. These power supply layers usually extend over the entire width and length of the PCB and are often referred to as *power planes*. Typically, output drivers are made out of active devices or gates, which are all part of a microprocessor or of a high-speed integrated circuit (IC). These ICs are mounted on the surface of the PCB and connected to the different layers of the printed circuit board using interconnects, such as wire bonds, bond pads, and vias [59].

Simultaneous switching noise (SSN) occurs when the simultaneous switching of many of these internal gates cause a voltage surge in the power distribution network (PDN). In fact, SSN was not noticeable in the past, due to the slow switching of digital systems with clock speeds in the MHz range [9]-[10]. However, the clock and data speeds of modern high-speed circuits have increased rapidly to the GHz range. Traditionally, the voltage drop or the current surge has been inferred to the inductive nature of the board parasitics [10]. In other words, the chip interconnects (wire bonds), the via and the power layers can be modeled as an *effective inductance*, L_{eff}, that altogether with the load and the output driver build a closed path.

When a time varying current i flows through the conductive closed path, an electromagnetic flux ψ is generated within the loop. The effective inductance L_{eff} of the loop is then given by

$$L_{eff} = \frac{\psi}{i}. \tag{2.8}$$

From Faraday's law, the induced voltage is

$$V_{ind} = \frac{d\psi}{dt}. \tag{2.9}$$

By substituting equation (2.8) into equation (2.9), the induced (or noise) voltage between the power and reference layers can be expressed as [2]

$$V_{ind} = L_{eff}\frac{\partial i}{\partial t}. \tag{2.10}$$

The noise voltage in equation (2.10) is often termed as *ground-bounce*, since the voltage glitch corresponds to an effective change of the supply voltage level and can therefore be seeing as a displacement of the ground level from zero to a non-zero value. Furthermore, the voltage fluctuation is generated when a single gate switches state. However, this voltage fluctuation would dramatically increase when hundreds or more gates and drivers switch simultaneously. Hence, equation (2.10) is given as

$$V_{ind} = NL_{eff}\frac{\partial i}{\partial t}, \tag{2.11}$$

where N is the number of switching devices. From equation (2.11), one can deduce the consequences of this SSN, as the number of gates that switch simultaneously increases, the generated noise voltage dramatically increases as well. This also implies that with the increase in the number of switching devices, the transient current consumed by the switching gates would increase. The effects posed by the switching devices on the performance and integrity of PCBs are discussed next.

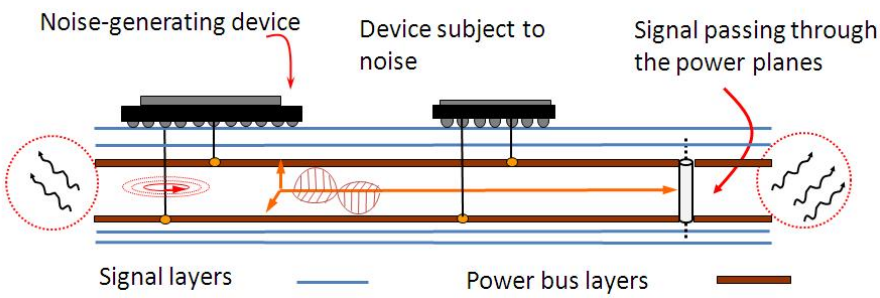

Figure 2.6: Schematic model for sources of noise and coupling in power planes environment [1].

When many active devices switch at the same time, induced current which flows through signal vias for example (see Fig. 2.6) excites a quasi-radial electromagnetic waves in the power/ground plane pair. These waves propagate along the parallel-plate guiding structure of the board. Such waves reflect from the edges of the PCB board causing resonances in the power plane cavity and resulting in voltage fluctuations. These voltage fluctuations affect the functionality of nearby idle devices (i.e., devices subject to noise) through energy coupling from vias. Eventually, the electromagnetic waves reaching the PCB edges diffract and start to radiate causing EMI radiation problems. In summary, simultaneous switching noise, if uncontrolled, can cause false logic and signal integrity issues. For example, when a switching device switches state, say from logic "0" to logic"1", a logic "0" could be read as a result of strong negative surge in the voltage or vice versa.

2.2.2 Previous trends on noise mitigation in high-speed PCB boards

Several methodologies had been introduced in the past in order to confront switching noise by reducing the resonance effects of the PCB parallel-plate guiding system. The most widely employed techniques include, but not limited to: decoupling capacitors [60], embedded capacitances [61]-[62], the use of dissipative lossy components along the edges of the PCB board [63]-[64], via-stitching [65], and dividing power planes into separable islands [66].

The most inexpensive used method is the placement of decoupling capacitors between the power plane layers around the sensitive integrated devices. These capacitors reduce high-frequency fluctuations on the power planes by providing a low impedance path between the power plane layers. These discrete capacitors have a dominant inductive behavior in the microwave frequency regime, due to the leads of the capacitors. The leads limit the noise mitigation capability of the capacitors to, typically, the sub 500 MHz

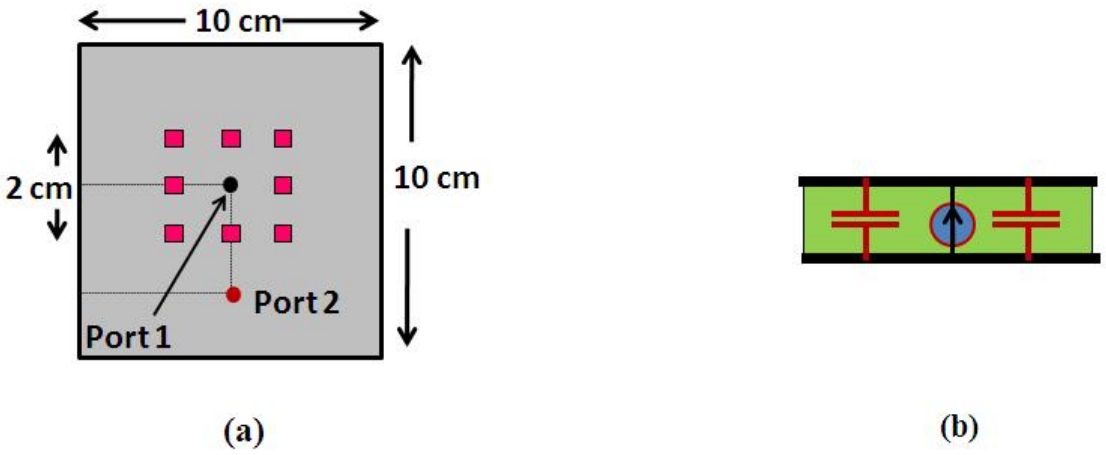

Figure 2.7: (a) Top view of a power plane surrounded by six decoupling capacitors; (b) Lateral view of the power plane, where port 1 is a representative of a time-varying switching current device. The PCB board is FR4 ($\epsilon_r = 4.4$, $\tan\delta = 0.02$, and thickness of $1.54mm$). The lumped element values of the decoupling capacitors: $R_{cap} = 50$ mΩ, $L_{cap} = 2$ nH, and $C_{cap} = 10$ nF are taken as those real-world capacitors provided in [2].

frequency band [2]. To demonstrate the limited capability of the decoupling capacitors, a source of switching noise in a power plane was modeled using CST Microwave Studio (MWS) [67]. The source of noise was surrounded with eight capacitors as illustrated in Fig. 2.7. Another port, representing an idle device, was placed outside the capacitors perimeter. The transmission coefficient was computed to quantify the energy (noise) that is picked up by the idle device. Fig. 2.8 shows the transmission coefficient for two scenarios: with and without the discrete capacitors. Clearly, the capacitors were only able to mitigate the low-frequency resonances, after which resonances take place, due to the dominant inductive behavior of the capacitors.

Another alternative to mitigate switching noise is to utilize embedded capacitances, which are achieved by shrinking the thickness of the parallel-plate PCB board. Although the embedded capacitances overcome the lead limitations, the deployment of such topologies in a low-cost PCB board increases cost of fabrication technology, in addition to unavoidable resonances of the power plane at some frequencies. Lossy materials and via stitching try to mitigate the radiated waves due to the noise generated by the switching devices in order to lower resonances of the PCB board. Power islanding is also commonly used, but it is limited to applications in which isolation is the main goal such that the source of noise and the susceptible components are kept on different power islands. All aforementioned methods are bandlimited, effective at most few MHz range, and are ex-

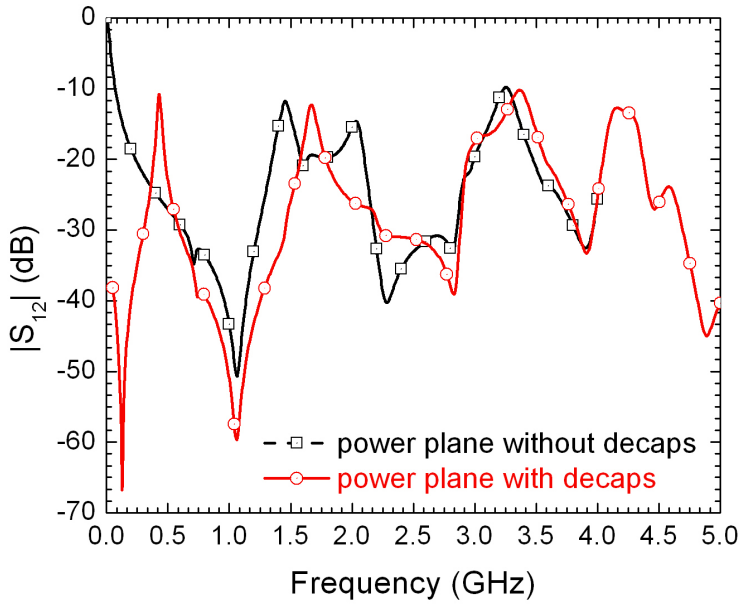

Figure 2.8: Simulated transmission coefficient of a parallel-plate power plane with and without decoupling capacitors.

pensive to implement at high frequencies. Thus, the question that is raised here are there any alternatives?

Electromagnetic band-gap (EBG) structures have been used in [68]-[72] for switching noise mitigation in PCBs and packages. Although the use of EBGs for noise mitigation is inexpensive and effective while still maintaining good signal integrity, an additional metallic layer is needed. Furthermore, EBG structures require vias, which is unattractive from the manufacturing and cost perspectives. Planar EBG structures were introduced for noise isolation in high-speed PCB boards with the advantage of eliminating the additional metal layer, however, at the cost of compromising the signal integrity [73]-[74]. One of the fascinating features of EBG structures is the mitigation of electromagnetic surface waves propagation over bandstop regime. Recently, EBGs have been used to minimize electromagnetic radiation from high-speed PCB boards [74], [1], [75].

Transmission line filters based on complementary split-ring resonators (CSRRs) were introduced in [76]-[77], where the CSRRs resonance is excited by the electric field normal to the ground plane. The function of the CSRRs, as in [76], was complementary to the split-ring resonators (SRRs) in the sense that SRRs create an effective bandgap for a magnetic field polarized normal to the surface of the loops, whereas in the CSRR, the effective bandgap is experienced by an electric field polarized normal to the surface of the

etched loops.

Since the CSRR is a natural filter for electric fields polarized normal to the rings, it is surprising that it was never used to mitigate electromagnetic switching noise in printed circuit boards (PCBs) and packages. In fact, it seems that the most fitting application of CSRR is mitigation of simultaneous switching noise as the topology calls for minimal etching of copper which has the advantage of decreasing the overall ohmic resistance of the power grid and improving the signal integrity. The work presented in this dissertation, as will be covered in Chapter 6, introduces a new topology for switching noise mitigation in PCBs using CSRRs. This is achieved through etching split-ring resonators on *only* a single metallic layer of the printed circuit board. In [78], I presented a numerical model for the proposed concept; herein, experimental validations are provided along with other studies for real-world applications where CSRRs are etched on a PCB made of FR4 dielectric board, which is most common in personal computers and laptop applications.

2.2.3 Sources of noise in shielded enclosures with apertures

The dramatic increase in sensitivity of electronic devices and the ever-increasing clock frequency of high-speed microprocessors increase the vulnerability of such systems to electromagnetic interference (EMI). The physical mechanism behind EMI is the electrical current that leads to either radiation or direct coupling onto other devices. Surface currents accumulate along conducting surfaces leading to radiation. Minimizing surface currents is a fundamental and very critical step in minimizing EMI.

To preserve the integrity and performance of electronic devices, it is necessary to shield the equipment from exterior interferences. However, the integrity of shielding enclosures is compromised by openings such as seams, and apertures. These apertures cannot be avoided in many practical designs, as would be the case when used for heat dissipation, air-flow, and input/output (I/O) cable penetration. The degraded integrity is commonly encountered, since apertures are very efficient radiators, and thus are undesirable sources of EMI radiation.

Electromagnetic radiation from metallic enclosures with openings that are excited by interior sources is of great importance in meeting the Federal Communications Commission (FCC) radiated EMI limits [79]. This is because in situations where the operating frequency is high such that the skin depth is less than the thickness of the shield, the shielding effectiveness will not depend on the shield material properties but on the openings and slots in the shield. Several frequencies that are sources of electromagnetic radiation and coupling are often encountered in modern electronic systems. One of which

is the frequency of an internal radiator within a system (i.e., secondary radiating source), such as heat sink, connectors, internal I/O cables, amongst others. Other frequencies that are sources of enhanced radiation are the resonant frequencies of enclosures and those of the slots or apertures present on the enclosures. Once electromagnetic radiation takes place at those frequencies, some of this energy leaks out through the apertures, and create currents on the outside environment. Those radio frequency currents form coupling paths (e.g. cables) eventually result in EMI and unwanted radiated emissions. In fact, the aforementioned sources of radiation are very critical issues for compliance of EMC requirements. Chapter 7 investigates such sources of radiation.

2.2.4 Previous trends on noise mitigation from shielded enclosures with apertures

The problem of electromagnetic field radiation from openings (apertures) is one of the most fascinating classical problems in physics and engineering. Tremendous amount of work have been done during the past 60 years to predict the electromagnetic field radiation from electromagnetic systems with openings of various sizes [80]-[84]. Numerous papers have attempted to develop analytical formulae to analyze the problem of radiation from such openings [80], [81]. Bethe in his pioneering work [80] has developed analytical relations to solve the problem of radiation from electrically small holes. Nowadays, with the dramatic increase in clock frequency of modern high-speed devices and increased complexity in systems packaging, the approximate analytical formulations would be inadequate to use, especially for EMC engineers when problems arise at design stages, like radiation from openings and alike. Nonetheless, numerical techniques have paved the road for such purposes. Several papers have been published in developing numerical models for the problem of electromagnetic radiation from apertures placed in chasses and enclosures [82] -[84]. However, most of the previous attempts have focused on mainly the prediction of radiation from apertures with various sizes and shapes.

With the expected increase in clock speed of microprocessors to 14.0 GHz and above [90], electromagnetic radiation and other related issues, such as power and signal integrity, will pose significant challenges. Therefore, there is the need for developing effective shields to minimize radiation from high-speed microprocessors without any modifications to the processors socket design. Another important issue this research work will address later in Chapter 7 is that when signal clock frequency or any of its subsequent harmonics coincides with the resonance frequency of the aperture, significant electromagnetic field leakage occurs.

Recently, electromagnetic bandgap (EBG) structures have been used in EMI/EMC literature to mitigate switching noise in high-speed printed circuit boards and packages [1], [91]. Interestingly, when EBG structures were first introduced, the potential for surface current suppression was explicitly discussed in [45], however, never exploited to mitigate surface currents in EMI/EMC applications. In this work, the emphasis is to gain further insight and understanding on the physical mechanism that makes apertures radiate. EBG structures, as will be shown in Chapter 7, can play a fundamental role in minimizing radiation from apertures.

To the best of my knowledge, the aforementioned issues have not been fully investigated. In this dissertation, novel use of EBG structures to shield apertures placed in metallic screens and enclosures is proposed. The technique comprises placing EBGs in the vicinity of the aperture's opening in order to mitigate the surface current while maintaining the aperture size for air flow and other mechanical functions. Numerical full-wave analysis are conducted and experimental work simulating real-world case study is presented to demonstrate the shielding effectiveness of the proposed technique.

2.3 Conclusion

In conclusion, a comprehensive background covering various sources of coupling that degrade the performance of antenna systems was introduced. Furthermore, sources of noise and EMI threats that disturb the functionality and degrade the integrity of modern high-speed digital systems were discussed. A literature review on previous methodologies and techniques adopted to mitigate such electromagnetic disturbances were summarized. In the next chapters, several cost effective techniques based on metamaterials are developed to overcome several challenging vital threats in antennas and electromagnetic systems.

Chapter 3

Artificial Electromagnetic Media

3.1 Introduction

Strong interest in artificial materials and engineered structures has been manifested in the recent years. One category of such engineered structures is electromagnetic band gap (EBG) structures. EBG structures exhibit unique characteristic of stopbands (bandgaps) in certain directions at microwave frequencies. These EBGs have the ability to mitigate surface waves propagation within the bandgap regime. Another category of engineered media belongs to artificial materials, which exhibit anomalous values of the constitutive parameters ϵ and μ at microwave frequencies. These artificial materials can be realized by embedding metallic (nonmagnetic) resonant inclusions in a host dielectric slab, and then stacking the slabs to form an effective medium.

In this chapter, three types of engineered structures are explored with more emphasis on their physical behavior. These artificial structures will be utilized later in this thesis for several applications.

3.2 Electromagnetic Band-gap (EBG) Structures

Generally, electromagnetic bandgap structures are class of man-made materials, in which novel and unusual behaviors can occur in such materials, unlike conventional dielectric materials. EBG structures operating in the microwave regime are periodic patterns created by metallic inclusions etched on dielectric materials or possibly other materials, like magnetic materials [45]. EBG structures are capable of suppressing surface waves in certain directions within a frequency band. EBG structures emulates a high impedance

surface (HIS) in its in-phase reflection bandwidth when used as a ground plane for planar antennas. This peculiar feature is in fact useful in many engineering applications, including but not limited to: enhancing the gain of printed antennas [92], improving the matching of low-profile wire antennas [93], enhancing the bandwidth and miniaturization of planar antennas [94], [95].

3.2.1 Mechanism of operation

The major characteristic of EBG structures is to exhibit frequency band with stopbands. At frequencies within the bandgap, surface waves are suppressed as presented in [96]. Without loss of generality, the mushroom-like EBGs are considered in this work, which is represented generically by the schematic shown in Fig. 3.1. These structures are characterized by periodic metallic patches connected to a common ground plane by plated through-vias. Patterned patches of size, a, are etched in a dielectric substrate of relative permittivity ϵ_r with a thickness h. The patches are separated by a small gap of distance g. Thus, the periodicity of such topology is $w+g$. The metallic patches are connected to lower conducting surface (ground plane) through plated vias of diameter d. At resonance, an EBG structure behaves like a parallel LC circuit; hence, it performs as a *band-stop* filter.

Considering a unit cell of the mushroom-like EBG structure, Fig. 3.2b depicts the origin of the lumped elements: capacitance and inductance within the EBG structure. Upon propagation of electromagnetic waves in such structures, currents are induced on the top metal plates, and will be confined within the small-loops (see Fig. 3.2a) that are bounded by the plated-vias. We can consider such confined loops as cavities, which exhibit resonant modes. Moreover, when voltage is applied parallel to the top surface, charges build-up around patches edges and give rise to capacitance, C. Due to the bouncing of charges back and forth, current flows through the plated-vias. Magnetic fields are induced as a consequence of the current flow, which corresponds to having an inductance, L.

There is an impedance that is associated with the surface of the EBG structure. Such impedance is equivalent to the impedance of a parallel LC-resonant circuit, consisting of the aforementioned sheet inductance and capacitance [45]

$$Z = \frac{j\omega L}{1 - \omega^2 LC}. \tag{3.1}$$

While the surface impedance is inductive at low frequencies and capacitive at high frequencies, it is very high near the resonant frequency, hence it can be termed as high-

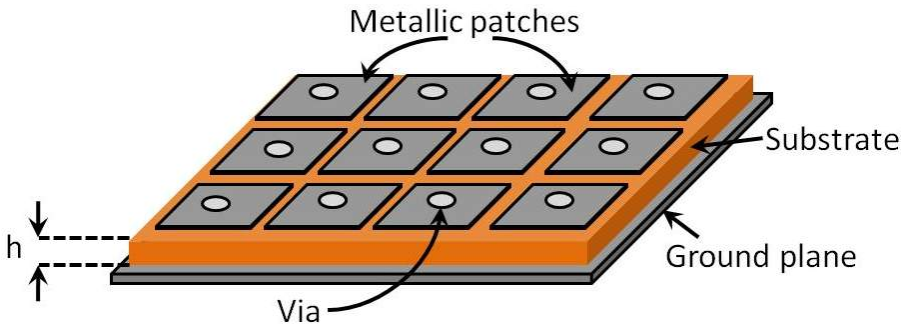

(a)

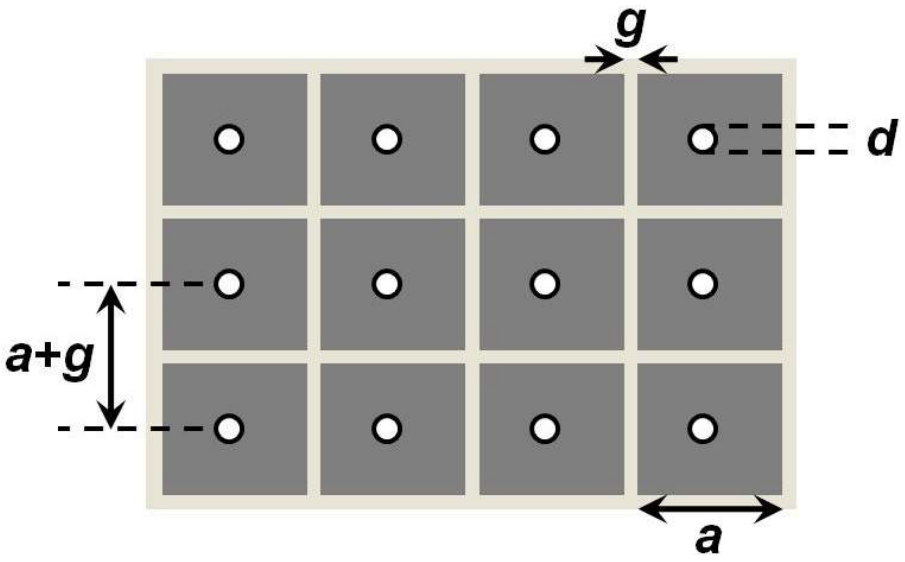

(b)

Figure 3.1: Typical mushroom-like EBG structure: (a) perspective view and (b) top-view with its design parameters.

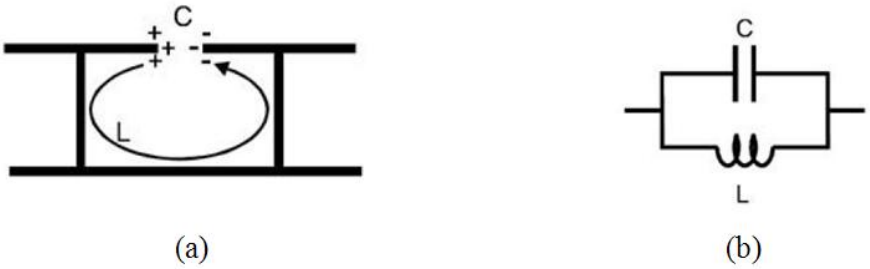

(a) (b)

Figure 3.2: (a) Illustration of the mechanism of operation in EBG structures, (b) equivalent LC resonant circuit.

impedance surface, with the resonance frequency given by

$$\omega_0 = \frac{1}{\sqrt{LC}}. \tag{3.2}$$

The bandwidth that characterizes the band gap of the mushroom EBG structures is given as

$$BW = \frac{1}{\eta_0} f_0 \sqrt{\frac{L}{C}}, \tag{3.3}$$

where η_0 is the free-space intrinsic impedance, and f_0 is the resonance frequency of the EBG structure.

3.2.2 Design Methodology of mushroom-like EBG structures

This section elaborates in much details the design methodologies encountered for the mushroom-like EBG structure, and likewise, one can extend such strategies to other EBG structures. Although the experimental models could be utilized, lumped elements circuit models can be used for initial design and numerical characterization based on full-wave simulators are then adopted for more accurate realization of the bandgap zones of such structures.

Experimental strategies

This method is based on fabricating the EBG structure, and then measuring the scattering parameters. Thus, one gets clear, yet accurate results for the band gap and filtering properties of such structures. However, this design method is inefficient, when it comes to time and design, since it will be costly to fabricate lots of structures, if one wants to perimetrically study or investigate the effects of some parameters of the EBG on any kind of application.

Lumped-elements Circuit model

Based on circuit theory, the resonance behavior of an LC circuit depends mainly on the parallel lumped circuit parameters: inductance, L, and capacitance, C. The approximate relations for the lumped inductance and capacitance elements are given as [45]

$$L = h\mu_0, \tag{3.4}$$

and

$$C = \frac{a(\epsilon_r + 1)\epsilon_0}{\pi} cosh^{-1} \frac{2a + g}{g}, \tag{3.5}$$

respectively, where μ_0 is the free-space permeability, h is the thickness of the EBG host medium, ϵ_0 is the free-space permittivity, ϵ_r is the relative permittivity of the EBG host medium, a is the EBG patch width, and g is the gap between the metal patches.

Numerical characterization

This sub-section covers in much detail the numerical strategies, which one can follow in order to design EBG structures. As a matter of fact, the numerical design strategies, that will follow up shortly, can be used to design any kind of EBG structures, no matter how the structure is, whether it is with vias or not, whether it is planar or not, still, the full-wave numerical solvers are quite powerful in extracting EBG parameters, and characterize their band gaps to a reasonable accuracy, as compared to experimentations.

Dispersion Diagram Representation The dispersion diagram is based on the relationship between wave numbers (or phase) and frequency(k-f). This extraction method for the EBG structures is based on Brillouin-zone [97]. The dispersion diagram provides details of the possible propagating modes that can be excited in different directions within the periodic structure (EBGs). The diagram also shows band gap zones that can potentially exist between such modes. In Brillouin theory, there exist certain directions within a unit cell of the periodic structure, that constitute a boundary region of propagation called irreducible Brillouin zone [97]. Therefore, it is sufficient to find the possible propagating modes that are excited within the EBG unit cell only in the directions of the vectors of the irreducible Brillouin zone.

Fig. 3.3 shows the three directions that one have to solve for in order to identify the bandgap zone. The three directions (regions) are: Γ-X, X-M, and then M back to Γ, as shown in the figure. The notation for Γ, X, and M points follow the terminology for the reciprocal lattice of a natural crystal [97]. The wave vector in each of the three regions is translated into the phase shift between the sides of the unit cell shown in Fig. 3.3. This translation allows the derivation of dispersion diagram using traditional eigenmode full-wave solver. The simulator calculates the frequencies of propagating waves that would generate such phase shifts. Within the numerical model, the x-direction (phase-1) is varied from 0^o - 180^o, while the y-direction (phase-2) is kept constant at 0^o. Thus, the possible propagating modes within the EBG unit cell can be solved for. Next, phase-y is varied from 0^o - 180^o, while phase-x is kept constant at 180^o. Within the last direction (M-Γ), both x- and y-phases (directions) are simultaneously varied from 180^o - 0^o.

Numerically, a unit cell of the EBG structure is modeled. Periodic boundary conditions (PBCs) are applied in all four walls of the EBG unit cell in order to ensemble

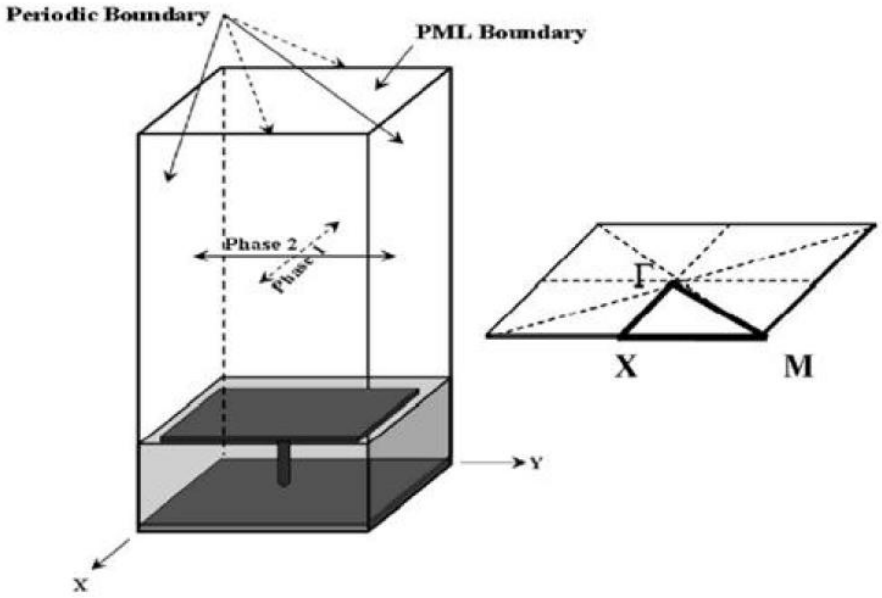

Figure 3.3: Numerical setup model of mushroom-like EBG structures used for dispersion diagram extraction.

a periodic behavior for the structure. A Perfectly matched layer (PML) is used on top of the EBG structure in order to mimic wave propagation in space without any kind of directions. Then, Eigenmode solver is used for the purpose of modes extraction; while the aforementioned directions (see Fig. 3.3) are varied in the three directions. Fig. 3.4 shows a sample of the dispersion diagram relation extracted using the eigenmode solver of CST MWS. A band-gap zone from 1.1 GHz - 1.28 GHz is achieved for this particular mushroom EBG structure.

3.3 Artificial magnetic materials

Generally, natural materials are characterized by constitutive parameters: the electrical permittivity ϵ, which is related to the response of a material to an electric field, and the magnetic permeability μ, which gives the response of the material to a magnetic field. At microwave frequencies, ϵ and μ are both positive for natural materials, which can be termed double-positive (DPS) materials. Fig. 3.5 shows a classification of materials based on their constitutive parameters ϵ and μ. Material with negative permittivity and negative permeability (DNG), however, cannot exist naturally over microwave frequencies and engineered artificial materials are developed and used to realize such materials [98]-[99]. This can be seen from the second and fourth quadrants of the $\epsilon - \mu$ domain shown in

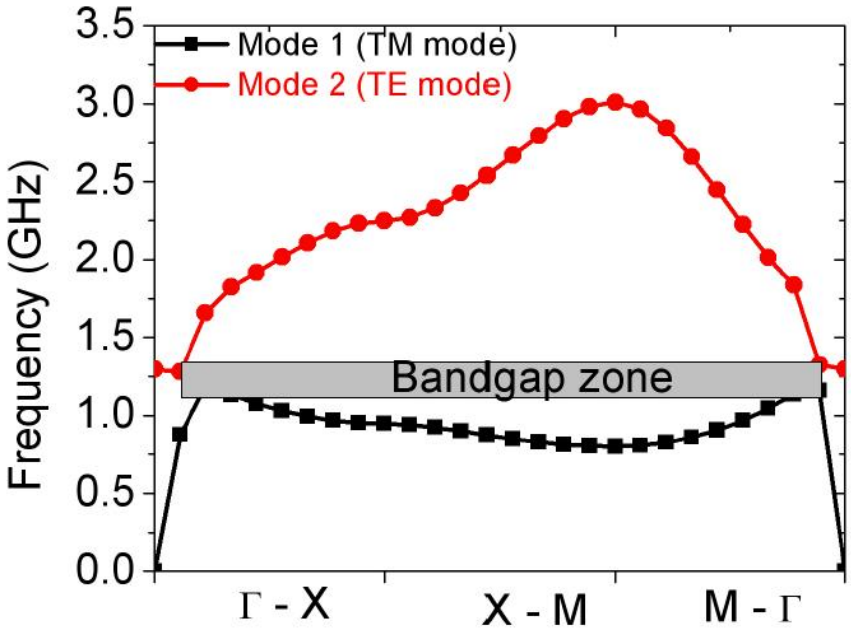

Figure 3.4: Dispersion diagram of an EBG unit cell with PBCs extracted numerically. The EBG parameters are: patch width $a = 18mm$, gap between patches $g = 0.2mm$ and via diameter $d = 0.6mm$.

Fig. 3.5. Artificial materials are engineered structures that have electromagnetic properties not yet available in nature. The composite structures, also known in the literature as *metamaterials*, are realized by etching metallic resonant inclusions in a host dielectric medium. The inclusions are electrically much smaller than the wavelength of the incident electromagnetic field. When exposed to an electromagnetic field, the artificial structures alter the electromagnetic properties of the host medium due to mainly the inclusions' resonating nature.

Amongst engineered materials, artificial magnetic materials (AMMs) have been the subject of interest for many years. This is due to their unique features, including the possibility of synthesizing magnetic permeability with real part of μ that is either positive (above zero) or negative (below zero). This is in contrast to ordinary magnetic materials, like ferrites, that loose their magnetic properties at microwave regime and above. The idea of creating magnetic materials from conductors was first proposed by Schelkunoff [100]. Ziolkowski *et al.* [101] used a similar concept to realize magnetic materials using loaded loops or loaded molecules. Pendry *et al.* [98] used concentric rings to provide further enhancement of the magnetic properties of the rings. Several artificial magnetic inclusions have been proposed in the literature. One of the popular and widely applied artificial magnetic material is the split-ring resonator (SRR). The SRR (see Fig. 3.6a-b) consists of

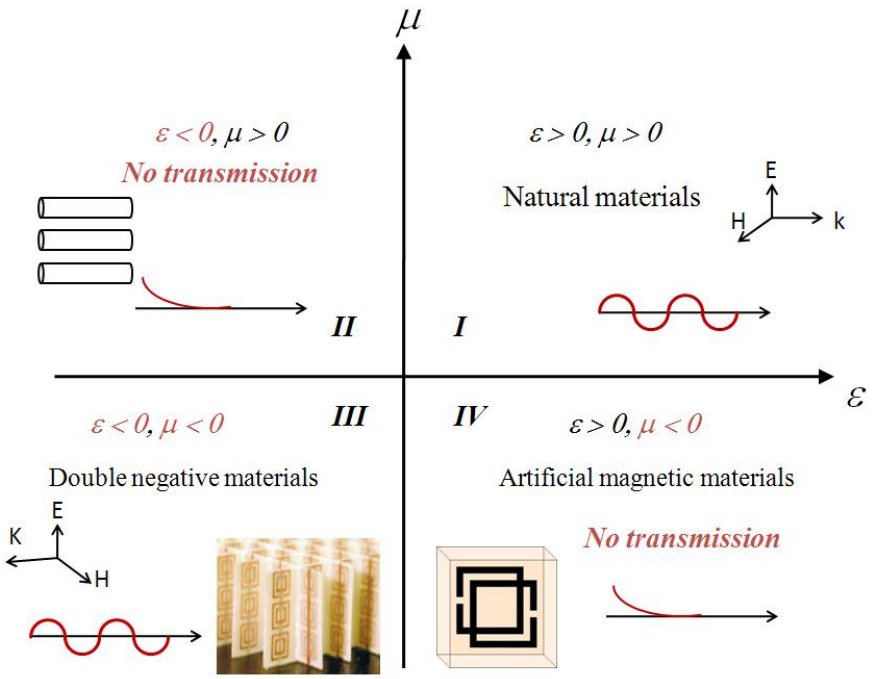

Figure 3.5: Materials classifications based on their constitutive parameters ϵ and μ.

two concentric (i.e., edge-coupled) metallic rings printed in a host medium, with splits in the rings at opposite ends. Marques *et al.* [102]-[25] presented a modification to the SRR (the so called modified SRR), where the two rings are very strongly capacitively coupled. The two split rings of the MSRR, as shown in Fig. 3.6c, are placed in broadside (hence called broadside-coupled, BC-SRR)normal to the incident magnetic field at the two sides of the substrate. Thus, the capacitive coupling in the MSRR can be increased more than the capacitive effect in the EC-SRR. Although the SRR is electrically small at resonance (i.e., unit cell dimension $< \lambda/10$ [25]), further miniaturization of sub-wavelength resonators is of particular importance for bandwidth enhancement and miniaturization of planar antennas, e.g. a substrate for patch antennas [103]-[104]. A number of miniaturized artificial magnetic inclusions have been proposed in the literature, to mention a few spiral resonators [105], capacitively-loaded loops [106], and space-filling (Hilbert) curves [107]-[108].

The electromagnetic response of an artificial structure can be considered as a homogenous medium, described by an effective material parameters, effective permittivity, ϵ_{eff}, and effective permeability, μ_{eff}. This effective response would be permissible if the unit cell dimension and separation between inclusions, say for example a,

$$a << \lambda, \tag{3.6}$$

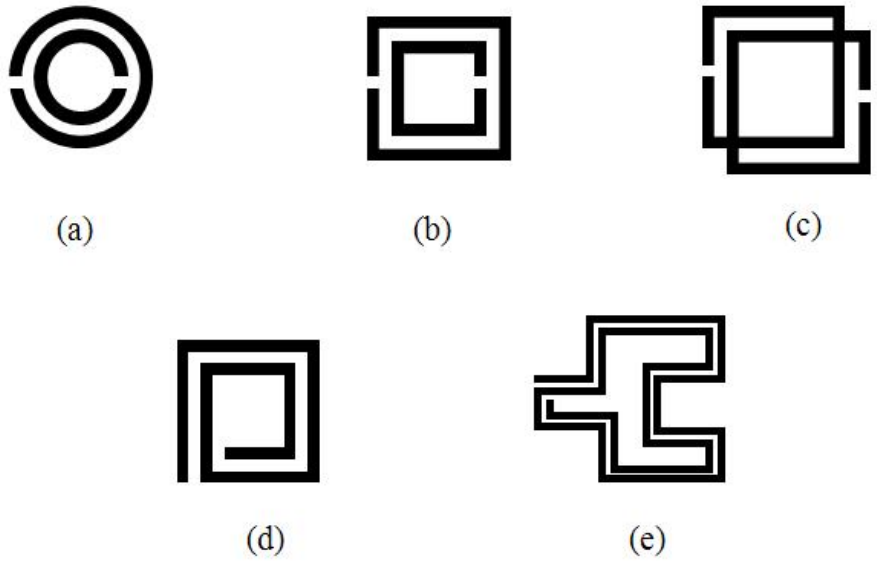

Figure 3.6: Several artificial metallic inclusions proposed in literature to realize magnetic materials. (a) Circular SRR, (b) Square SRR, (c) Modified SRR (MSRR), (d) 2-turn Spiral resonator (SR), and (e) Fractal Hilbert curve.

where λ is the operating wavelength of incident electromagnetic radiation.

When the condition 3.6 holds, quasi-static behavior for the artificial materials can be applied, in which lumped RLC elements are sufficient to provide qualitative description of the physical behavior of the artificial materials. Furthermore, when the spacing between individual unit cells of artificial materials is much smaller than the wavelength and when unit cells geometrical factors satisfy 3.6, it is justified to look for the effective constitutive parameters of the artificial media [109]. The physical behavior and numerical modeling of AMMs is discussed in the next subsequent sections.

3.3.1 Mechanism of operation

Several analytical models for artificial magnetic materials had been proposed by several research groups [98],[25],[110]-[112]. In the following, a brief discussion on the mechanism of operation of artificial magnetic materials is provided. Consider an incident electromagnetic field with an axial magnetic field impinges upon the artificial magnetic building block shown in Fig. 3.7a. As mentioned earlier, artificial magnetic materials based on the SRRs and other geometrical resonant inclusions react to the impinging magnetic field. This in turn results in an induced electromotive force, *emf*, in the rings. This *emf* in turn results in an induced current, I, that flows around the metallic inclusions as shown in

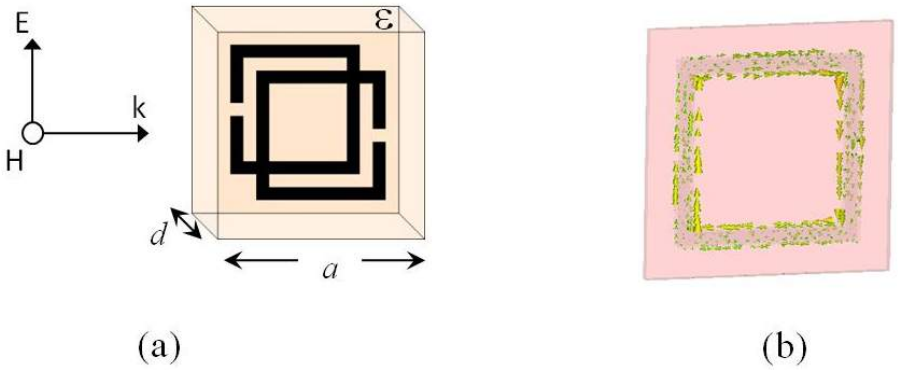

Figure 3.7: (a) Artificial magnetic unit cell based on the BC-SRR, (b) 2D vector plot showing the induced surface current distribution on the unit cell.

Fig. 3.7b. The circulating current lines will flow from one ring to the other through the capacitive gaps in the form of field displacement current lines. The total current gives rise to an induced magnetic field which results in an inductive part of the total impedance of the unit cell inclusion. Finite metal conductivity contribute to the real part of the total impedance. Hence, the effective induced current for the structures shown in Fig. 3.7 can be expressed as [110]

$$I = \frac{emf}{Z_{inc}} = \frac{emf}{j\omega L_{eff} + \frac{1}{j\omega C_{eff}} + R}, \tag{3.7}$$

where emf is the electromotive force, Z_{inc} is the total impedance of the inclusion. The inclusion lumped circuit parameters L_{eff}, C_{eff}, R_{eff} represent the inductance, capacitance and resistance of the inclusion, respectively, which are provided in [102].

The electromotive force can be expressed as

$$emf = -j\omega\mu_0 SH_{ext}, \tag{3.8}$$

where S is the effective area penetrated by the external magnetic field, H_{ext}.

Due to the exerted magnetic field, there will be an induced magnetic dipole moment within the inclusion, which is expressed as

$$m = \mu_0 SI. \tag{3.9}$$

The magnetic susceptibility, χ_m, quantifies the degree of magnetization of a material in response to an applied magnetic field. It is expressed as

$$\chi_m = \frac{M}{H_{ext}}, \tag{3.10}$$

where $M$is the average of the individual magnetic dipole moments within the bulk structure, which is termed as the magnetic polarization.

In electromagnetism, the magnetic permeability, μ, results due to the induced magnetization in the material. The permeability is expressed as the ratio of the total magnetic flux and the applied magnetic field in the material,

$$\mu_{eff} = \mu_0(1 + \chi_m). \tag{3.11}$$

From the above relation 3.11, it is visible that the effective magnetic permeability can be enhanced as a consequence of the increase in the effective magnetic susceptibility. The enhanced μ_{eff} is generally complex, with a positive real part below the inclusion's resonant frequency and negative real part above resonance.

3.3.2 Numerical modeling

Artificial magnetic materials have been extensively studied by several research groups. One studied aspect of the AMMs focused on the retrieval and characterization of such materials [109]-[113]. In this part, a unit cell of the MSRR (or the so called broadside coupled BC-SRR) is designed that will be used later in chapter. 4 for decoupling antenna systems. Initial design dimensions of the SRR inclusion unit-cell were estimated numerically using the characterization model that will be discussed later. Next, the tuned dimensions were obtained such that the inclusion resonance takes place at the middle of the frequency band of interest. The SRR rings considered here have equal sides of lengths $L = 12mm$ with strip width of $1mm$. The rings with opposite cut openings are etched on the sides of a dielectric substrate (Rogers RO4350, $\epsilon_r = 3.48$, $\tan\delta = 0.004$) having a thickness of $0.762mm$. The cut gaps within the metallic rings is $1mm$. The size of the unit cell, a, (see Fig. 3.8(a)) is 16 mm, which is much less than the operating wavelength at a frequency of 1.24 GHz. The SRR rings are made of copper with a thickness of 20 μm.

In order to numerically characterize the SRR inclusions, an air-filled waveguide with the artificial unit cell positioned at the center of the waveguide is used as shown in Fig. 3.8(b). Notice that the cell is positioned such that the incident magnetic field is perpendicular to the inclusion's surface. The model mimics a TEM wave impinging normally in the inclusion (see Fig. 3.8(b)), with top and bottom sides of the air-filled waveguide assigned as perfect electric conducting (PEC) walls, while its sides as perfect magnetic (PMC) walls. The assigned PEC-PMC boundary conditions mimic an infinite layer of the BC-SRR inclusions. In fact, the adopted PEC-PMC has the advantage of allowing the use of two ports in comparison to the PBCs that assumes a plane wave excitation. The characterization model adopted here is based on the retrieval extraction method reported

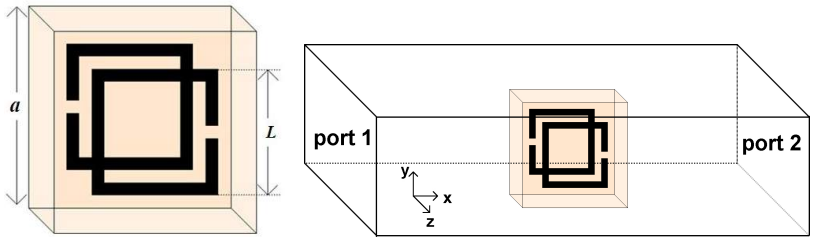

(a) (b)

Figure 3.8: The developed single-negative magnetic metamaterials based on the (BC-SRRs): (a) Split-ring resonator (BC-SRR) unit cell with its dimensions, (b) waveguide structure used for the characterization of the BC-SRR inclusion. Note that **E**-field points in y-direction, **H**-field is in z-direction, and the propagation is x-direction.

in [109], [113]. Basically, one have to compute the reflected and transmitted coefficients of a unit cell inclusion with the assigned periodic boundary conditions, from which the effective permittivity ϵ and permeability μ are retrieved using the procedure provided in Appendix A.

Fig. 3.9 shows the scattering parameters, S_{11} and S_{21}, computed using two commercially available full-wave simulation tools (Ansoft HFSS [114] and CST MWS). Good agreement can be seen between the two solvers, where S_{21} from the two solvers show excellent agreement, while slight variation is noted for the reflection coefficient S_{11}. The transmission coefficient, S_{21} is below -20 dB at resonance as shown in Fig. 3.9. The dip in the transmission coefficient is attributed to the magnetic resonance nature of the developed inclusions when a magnetic field impinges normally to the inclusions' surface. As such, the energy is sustained within the inclusions and results in no transmission at the enhanced magnetic resonance. The extracted real and imaginary parts of the effective electric permittivity and magnetic permeability of the developed magnetic resonators are shown in Fig. 3.10.

In Fig. 3.10, the effective permeability μ_{eff} is complex, and has positive real values below the resonance frequency, $f_0 = 1.23$ GHz. Furthermore, negative values for the real part of μ_{eff} covers the frequency range from the resonance frequency to 1.35 GHz. As artificial materials are inherently dispersive, the radiation losses are small, since the unit cell dimensions are much smaller than the free-space wavelength. Hence, the quality factor, Q, is expected to be relatively high. The Q-factor was estimated numerically using the model shown in Fig. 3.11. Note that both metallic and dielectric losses were incorporated within the numerical simulation model. Absorbing boundary conditions are assigned to enclose the geometry. The SRR unit cell was excited by a single coaxial 50Ω

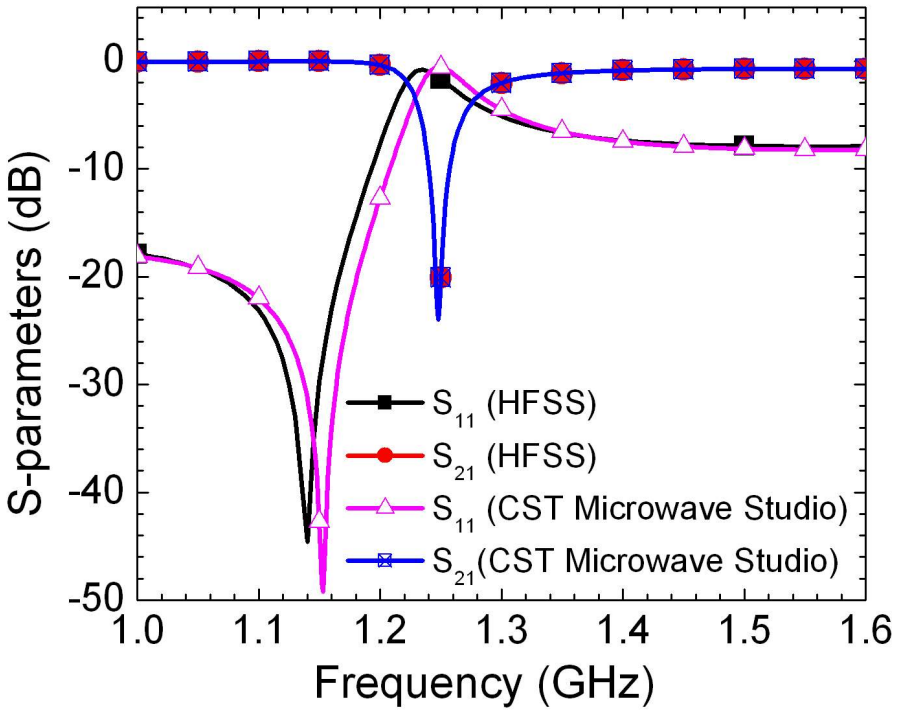

Figure 3.9: Scattering parameters of an infinite layer composed of BC-SRR inclusion with periodic PEC-PMC boundary conditions.

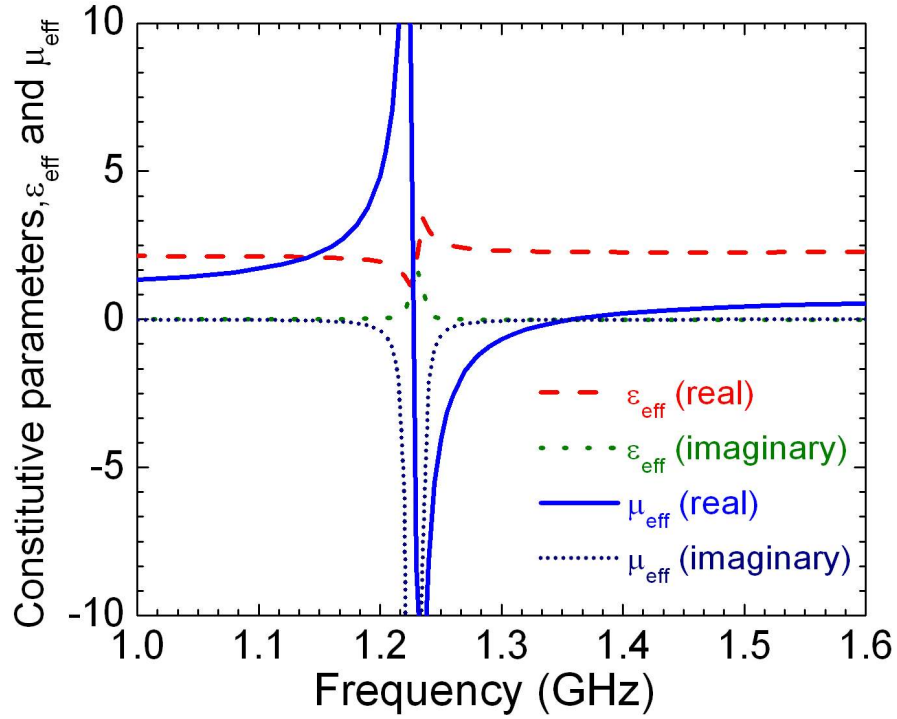

Figure 3.10: Numerically retrieved relative constitutive parameters of an infinite layer composed of BC-SRR inclusion with periodic PEC-PMC boundary conditions.

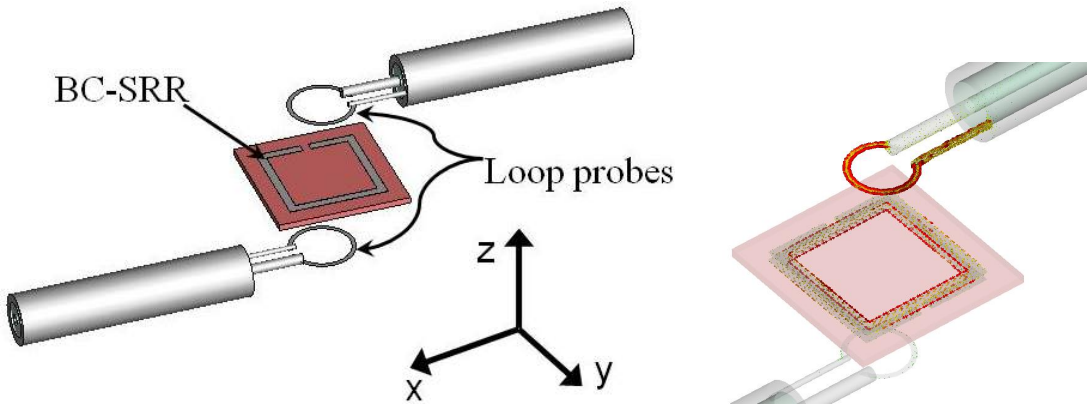

(a) (b)

Figure 3.11: (a) Numerical model setup used to estimate the Q factor of the SRR unit cell, (b) Surface current distribution at the SRR's resonance.

connector ended with a small loop probe. The loop antenna is expected to excite the SRR with a quasi-homogenized magnetic field normal to the unit cell (along the z-direction in Fig. 3.11). Another loop antenna was placed underneath the unit cell, and transmission coefficient S_{21} was computed numerically using CST MWS. The peak in S_{21} shown in Fig. 3.12 indicates the resonance of the SRR unit cell. The estimated loaded Q of the SRR was 195. The induced surface current along the metallic rings of the SRR unit cell is plotted as shown in Fig. 3.11(b).

3.4 Sub-wavelength Complementary Resonators

As discussed in Section 3.3, the realization of sub-wavelength particles based on resonant metallic inclusions patterned in a homogenized host medium had made it possible to synthesize magnetic permeability in the microwave and optical regimes. Similarly, It is possible to engineer the permittivity of a bulk medium by facilitating patterned metallic inclusions. Pendry *et al.* showed that an array of thin wires arranged in a cubic lattice can indeed exhibit negative effective permittivity at microwave regime given by [115]

$$\epsilon_{eff}(\omega) = 1 - \frac{\omega_p^2}{\omega(\omega + i\Gamma)}, \tag{3.12}$$

where Γ represents the energy dissipation of the plasmon into the system. The other term, ω_p, is the *plasma frequency* for metals, and is given in terms of electron properties by

$$\omega_p^2 = \frac{nq^2}{\epsilon_0 m_e}, \tag{3.13}$$

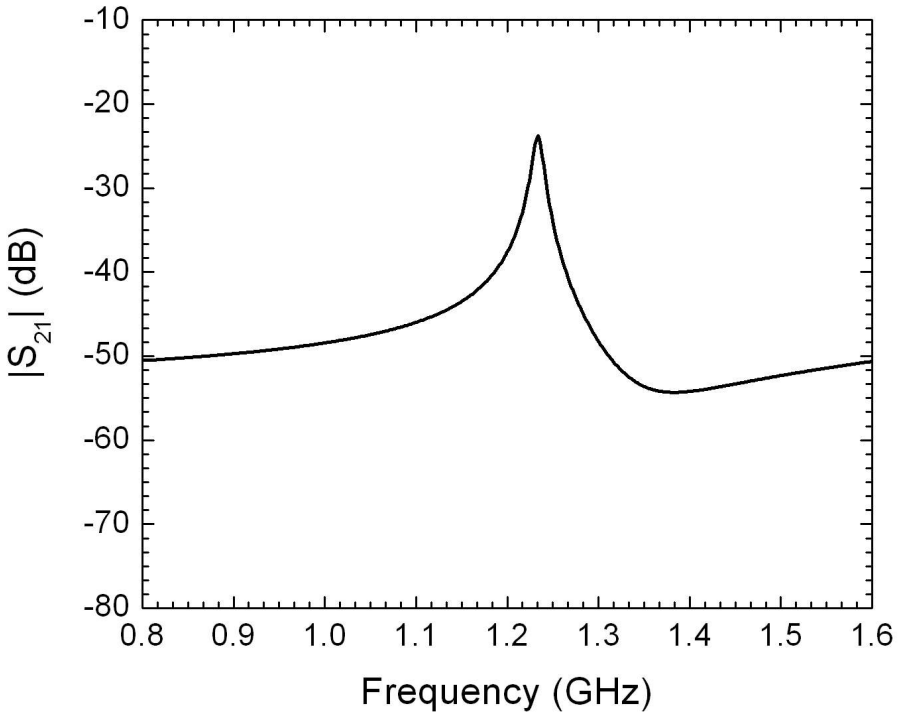

Figure 3.12: Simulated transmission coefficient S_{21} computed from the setup in Fig. 3.11.

where q is the electron charge, and m_e and n are the effective mass and density of electrons, respectively. The wires appear as small dipoles when excited with an applied electric field parallel to the wires plane, similar to the electric dipoles of atomic and molecular systems in natural materials.

Although the wire structure can tailor effective permittivity at microwave regime and below, the wire structure is still bulky and undesirable for planar microwave applications. Recently, Falcone *et al.* introduced in [76] a sub-wavelength resonant planar particle, known as the *complementary* split ring resonator (CSRR). Several CSRR particles, etched out from ground metallic screen, form the basis of constructing a compact stopband microstrip filter, as illustrated in Fig. 3.13. The bandstop behavior is attributed to the existence of negative ϵ_{eff}. Interestingly, CSRR particle can be easily excited with normal electric field, and hence, CSRR particle is very easy to integrate in transmission line environment. In summary, CSRR particles have been extensively applied in implementing variety of compact microwave filters and other microwave structures [3], and yet have lots of potentials to explore.

By looking into Fig. 3.14, it can be seen that the complementary of the planar SRR structure is obtained by replacing the SRR metal parts (rings) with apertures (slotted rings), and the apertures (surrounding free-space region) with metal plates [116]. If we

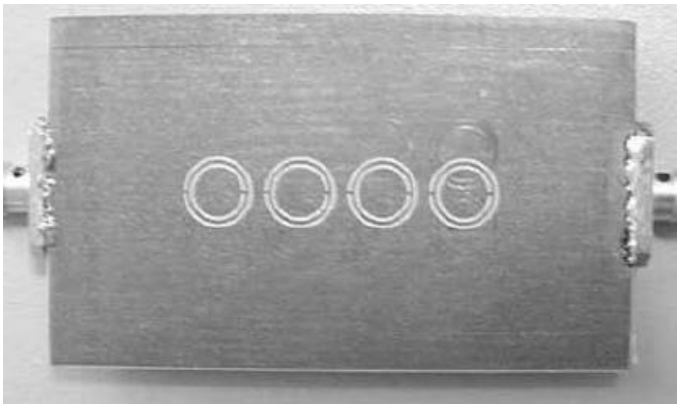

Figure 3.13: Bottom view of the bandstop filter with 4 CSRR inclusions etched out from ground plane [3]. Note that gray area represents metallization. On top view of this filter, a simple microstrip line is used to measure the S_{21}.

assume that metals have zero thickness and have infinite conductivity (perfect electric conductor PEC), it can then be inferred that the apertures (CSRRs) would behave as perfect magnetic conductors (PMC), when symmetry is taken into considerations. In this case, the SRR and its complementary screen (the CSRR) are dual.

The inspiration for the CSRR structure, and its counterpart (SRR), comes from Babinets principle in diffraction theory [116], which in its general form relates the relation of one particular screen with its complementary, for example, the resonant slot antenna is deduced from its counterpart dipole antenna. Consider an SRR structure which has a magnetic moment that can be excited by a magnetic field perpendicular to the ring. Based on Babinets principle and duality, it is expected that the complementary SRR structure will have a complementary excitation [117], in which the CSRR will have strong electric dipole moments that are excited by an axial electric field, as illustrated in Fig. 3.15. It is important to emphasize here that although duality was applied in the above scenario, the CSRR is not rigorously the dual of SRR particle. This is due to the presence of the dielectric layer, however, this would show as a shift in the response of the CSRR structure in comparison to its counterpart. In summary, the behavior of the CSRR particle excited by an axial electric field will be dual to the response of the original SRR structure that is excited by an applied external magnetic field, inhibiting electromagnetic propagation in both cases around the resonance frequency of the particle.

Recently, analytical models for transmission-lines using CSRRs have been introduced in [118]. However, the models do not explicitly provide any alternatives to design CSRR inclusions as building blocks for engineering applications. Furthermore, the models in [118] neither were able to predict the effective permittivity nor the losses of the com-

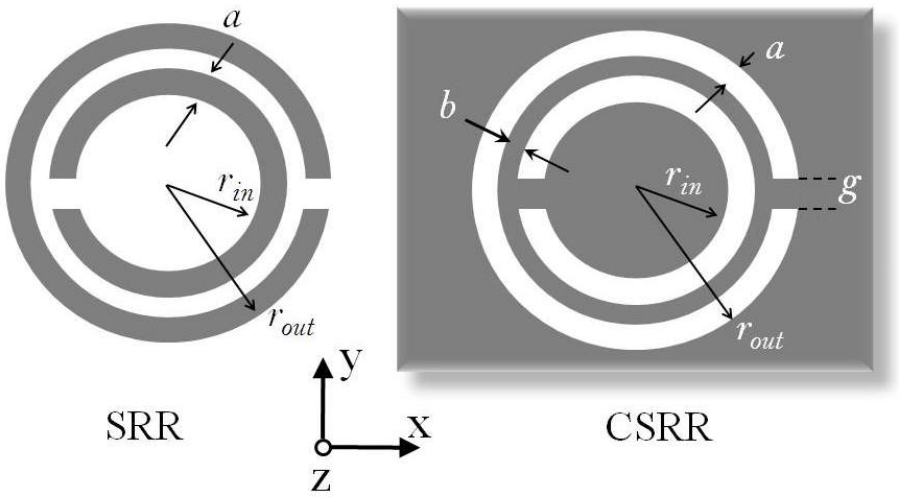

Figure 3.14: Lateral view showing the artificial magnetic particle, SRR, and its complementary, the CSRR inclusion. Note that gray area represents metallization.

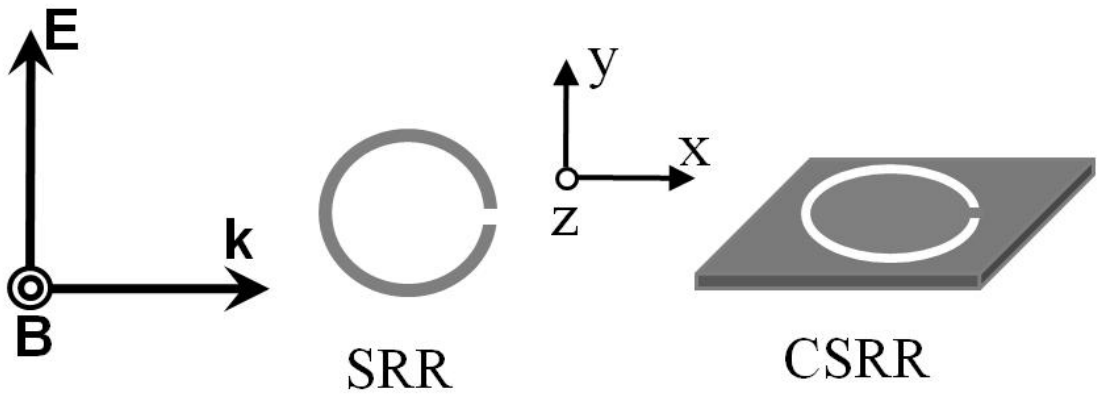

Figure 3.15: The dual SRR and CSRR particles. While an incident electromagnetic wave will excite the SRR with axial magnetic field when incident in the xy-plane, an axial electric field is needed to excite the CSRR (in xy-plane). Note that gray area represents metallization.

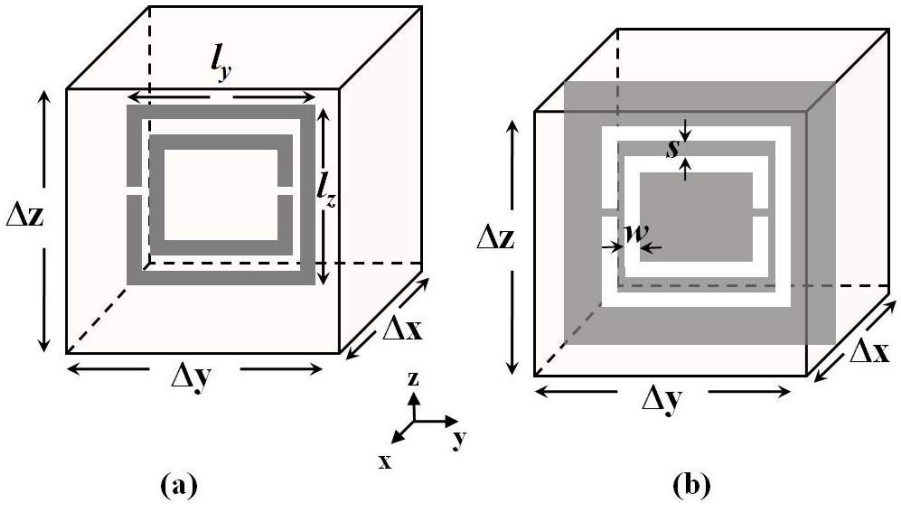

Figure 3.16: (a) A unit cell of an artificial magnetic inclusion, and (b) its complementary screen. Note that gray area represents metallization.

posite medium. In this part, analytical models for CSRR inclusions are presented. The formulations are general and can be used to provide engineers with sufficient estimates for the resonance frequency and material properties of such particles. The analytical formulations are able to describe the physical behavior of CSRRs and provide the effective electric permittivity of such inclusions. As will be shown later, the effective permittivity of CSRR inclusions is complex with a negative real part above the resonant frequency.

3.4.1 Analytical models for artificial complementary resonators

Fig. 3.16a shows an artificial magnetic inclusion unit cell. For illustration, an edge-coupled split-ring resonator (EC-SRR) is shown. Fig. 3.16b shows the complementary screen of the EC-SRR. With the assumption that both resonators are electrically small compared to the wavelength λ_0, simple quasi-static relations based on RLC lumped elements can be used to describe the physical behavior of such artificial materials.

Starting with Ampere's circuital law, one can have the following relation

$$I_{enc} = \oint \mathbf{H}.\mathbf{dl} = j\omega\epsilon(\mathbf{E}_{ind} + \mathbf{E}_{ext}).\mathbf{S}, \tag{3.14}$$

where $\mathbf{S}$ is the surface area enclosing the unit cell. The magnitude of the induced electric field, E_{ind} can be expressed as

$$E_{ind} = -\frac{V_{ind}}{\triangle x}, \tag{3.15}$$

and the induced voltage within the engineered unit cell is given in terms of the unit cell

impedance as

$$V_{ind} = I_{enc}.Z_{inc}, \tag{3.16}$$

where $\triangle x$ is the periodicity of the unit cell inclusion and Z_{inc} is the impedance of the inclusion.

Equation (3.16) can be expressed as

$$V_{ind}Y_{inc} = I_{enc}, \tag{3.17}$$

where Y_{inc} is the admittance of the unit cell.

Substituting (3.15) and (3.17) into (3.14) and rearranging the terms, we get the following relation

$$V_{ind}[Y_{inc} + j\omega(\frac{\epsilon S}{\triangle x})] = j\omega\epsilon E_{ext}S, \tag{3.18}$$

where $\triangle x$ is the periodicity of the unit cell, S is the surface area, given by $\triangle y \triangle z$, and C_{eff} is the effective capacitance of the artificial complementary inclusion, that is given by

$$C_{eff} = \frac{\epsilon S}{\triangle x} = \frac{\epsilon_0 \epsilon_r S}{\triangle x}. \tag{3.19}$$

In the case of a pair of opposite charge particles of magnitude q, the individual dipole moment due to an external electric field can be expressed as

$$\mathbf{p} = q\mathbf{d}, \tag{3.20}$$

where q is the charge of the electron and $\mathbf{d}$ is the displacement vector between the positive and negative charges.

The polarization vector $\mathbf{P}$ is the total dipole moment per unit volume, and can be defined as

$$\mathbf{P} = \lim_{\triangle v \to 0} \frac{\mathbf{p}}{\triangle v} = \frac{N(CV_{ind})}{\triangle x \triangle y \triangle z} = N(\frac{\epsilon S}{\triangle x})\frac{V_{ind}}{\triangle y \triangle z}. \tag{3.21}$$

where N is the number of paired charge particles.

The electric permittivity is the ratio of total electric displacement field and the applied electric field in a host media. Substituting (3.18) and (3.21) into the well-known relation for the electric displacement field, the effective electric permittivity ϵ_{eff} can be expressed as

$$\epsilon_{eff} = 1 + \frac{Kj\omega C_{eff}}{Y_{inc} + j\omega C_{eff}}, \tag{3.22}$$

where K = -$S/(\triangle y \triangle z)$ and Y_{inc} is the admittance of the unit cell inclusion. The minus sign appended to the parameter K indicate that the electric field lines within the unit cell inclusion are in opposite direction to the external electric field.

In terms of impedances, equation (3.22) can be expressed as

$$\epsilon_r = 1 + \frac{KZ_{inc}}{Z_{inc} + \frac{1}{j\omega C_{eff}}}, \tag{3.23}$$

where Z_{inc} is the effective impedance of the unit cell inclusion. Z_{inc} consists of two parts: R_{eff} accounts for the losses due to the finite conductivity of the metallic rings around the slots, and is given by

$$R_{eff} = \frac{l_{tot} + l_{avg}}{\sigma s \delta}, \tag{3.24}$$

$$\delta = \sqrt{\frac{2}{\sigma \omega \mu_0}}, \tag{3.25}$$

where δ and σ are the skin depth and conductivity of the metal, respectively, μ_0 is the permeability of free-space, and s is the separation between the slotted rings. The lengths l_{tot} and l_{avg} are the total and average side lengths of the metallic strips and are given by

$$l_{tot} = 4(l_y + l_z - 4w - 2s), \tag{3.26}$$

$$l_{avg} = (l_y + l_z - 4w - 2s)/2, \tag{3.27}$$

where l_y, l_z, w, and s are as labeled in Fig. 5.1. Note that the factor of 2 in equation (3.24) is to account for the losses of inner and middle metal rings between the two slots. The second part of Z_{inc} is given by $Z_{mut} = Z_{pul} l_{avg}$, and accounts for the inductive coupling between the external and internal strips around the slotted rings. The per-unit length impedance, Z_{pul}, is modeled as the impedance of a co-planar waveguide (CPW) structure of length l_y, strip width s, and slot width w, that is obtained using conformal mapping [119]

$$Z_{pul} = j\omega {\eta_0}^2 \epsilon_0 (1 - jtan\delta) \frac{F(\sqrt{1-k^2})}{F(k)}, k = \frac{\frac{s}{w}}{\frac{s}{w} + 2}, \tag{3.28}$$

where $\eta_0 = \sqrt{(\mu_0/\epsilon_0)}$, and $F(.)$ is the complete elliptic integral of the first kind, given by

$$F(k) = \int_0^{\pi/2} \frac{d\phi}{\sqrt{(1 - g^2 sin^2(\phi))}}. \tag{3.29}$$

3.4.2 Numerical modeling

Numerical full-wave models are developed here to validate the proposed analytical model for artificial complementary resonators. Fig. 3.17 depicts the numerical setup model using Ansoft HFSS. Within the numerical model, a complementary resonator (EC-CSRR is considered here) unit cell inclusion is surrounded with perfect electric conductor (PEC) normal to the y-axis and perfect magnetic conductors (PMCs) normal to the z-axis. The

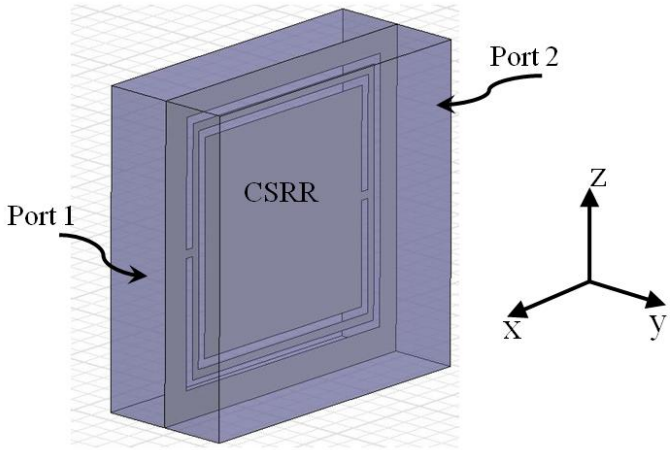

Figure 3.17: Numerical set-up used to extract the permittivity of the CSRR inclusion. Note that gray area represents metallization.

assigned PEC-PMC boundary conditions (BCs) mimic a homogenized effective medium, when the unit cell dimension is much smaller than the incident wavelength. Furthermore, a plane wave excitation is applied with the assigned BCs with two waveports that are normal to the x-axis. By computing the reflection/transmission coefficients, the electric properties of the artificial complementary resonator can be retrieved [109].

The dimensions of the EC-CSRR unit cell are: side length of $l_y = l_z = 7mm$, slot width $w = 0.186mm$, and separation between slots $s = 0.186mm$. The periodicity along the x-direction is $\triangle x = 3.048mm$. The host medium for the EC-CSRR has a dielectric constant of $\epsilon_r = 2.2$ and loss tangent $tan\delta = 0.0009$. Note that the CSRR metallic screen is assumed copper to account for the losses. Figs. 3.18-3.19 show the magnitude and phase of the scattering parameters obtained from the model shown in Fig. 3.17. Fig. 3.20 depicts the effective electric permittivity that is computed using the proposed analytical formulation and compared with the numerically retrieved permittivity characterized using the method in [109]. Good agreement between analytical and numerical retrieved effective permittivity is observed. A slight shift (less than 10%) in the resonance frequency of the EC-CSRR inclusion is also observed. This can be attributed to the inductive coupling accounted for in equation (3.28), which considered only the adjacent strip elements around the slotted rings of the EC-CSRR inclusion. Good agreement can also been seen for the magnitude of the real part of ϵ_{eff}.

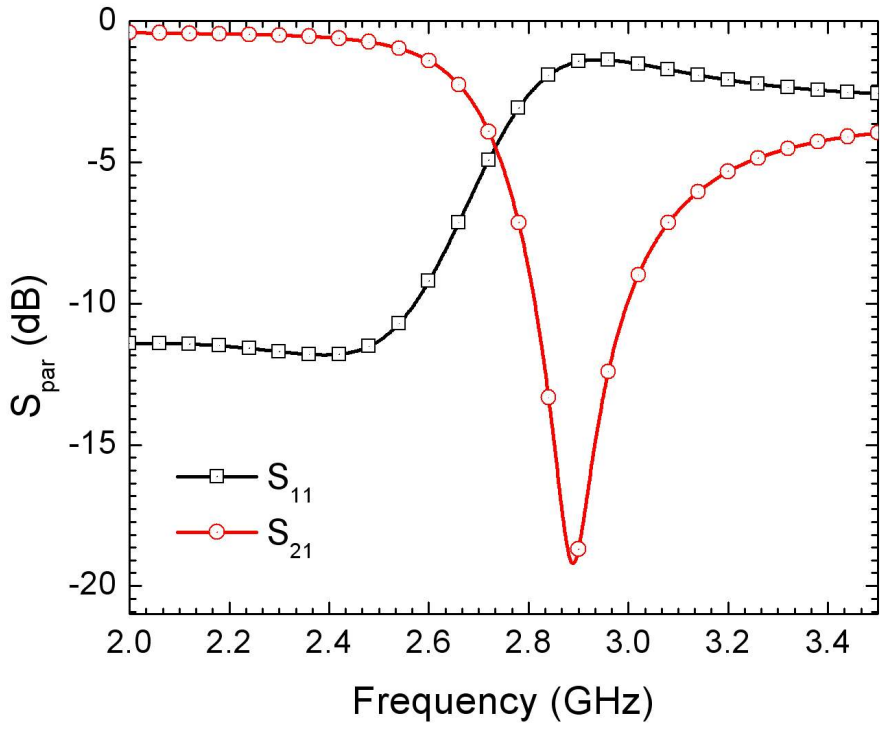

Figure 3.18: Simulation results for the magnitude of scattering parameters for the engineered EC-CSRR inclusion.

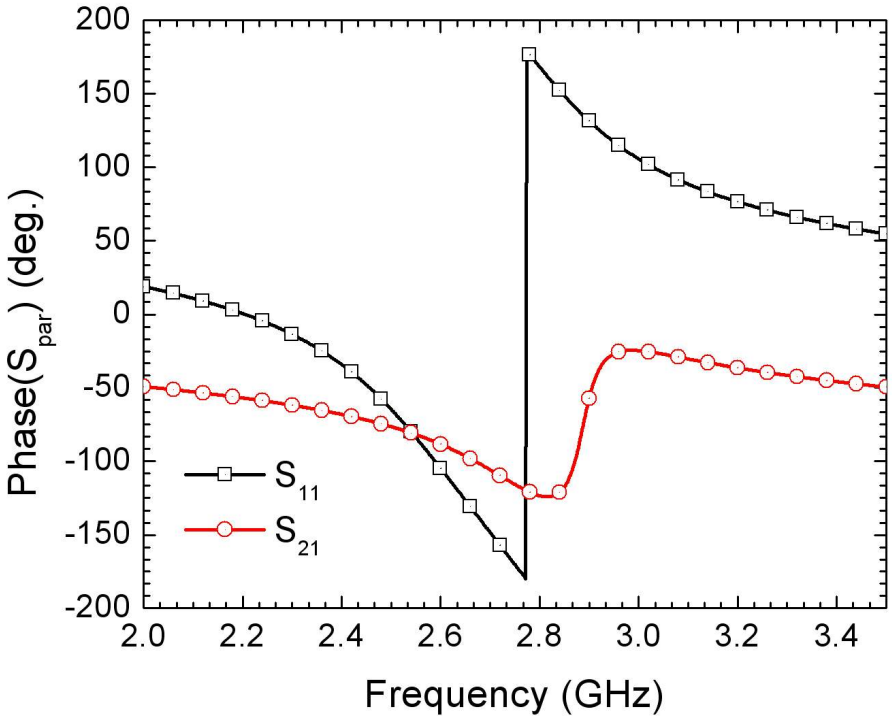

Figure 3.19: Simulation results for the phase of scattering parameters for the engineered EC-CSRR inclusion.

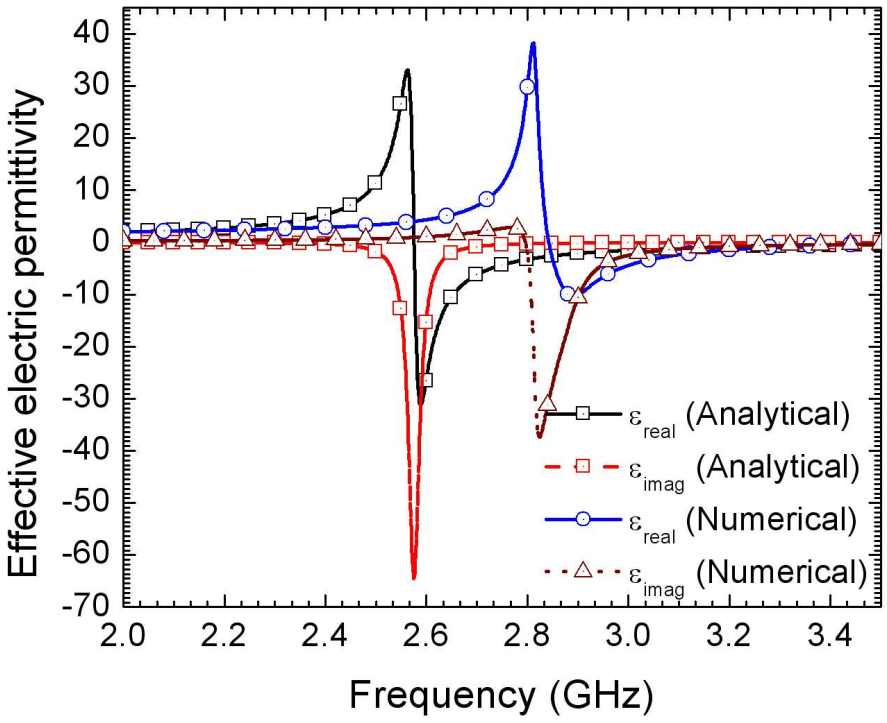

Figure 3.20: Calculated effective electric permittivity for complementary EC-CSRR inclusion using the proposed formulation and compared with the numerically retrieved permittivity.

3.5 Conclusion

In this chapter, an overview of engineered electromagnetic media was presented. Three sub-classes of metamaterials were discussed: EBG structures, artificial magnetic materials and complementary resonators.

Analytical model for sub-wavelength complementary resonators was presented. The resultant formulation relates the effective electric permittivity, ϵ_{eff}, of the complementary resonators as a function of equivalent RLC lumped elements. Full-wave numerical characterization were adopted to retrieve the constitutive parameters, ϵ_{eff} and μ_{eff}, of the developed inclusions.

Based on Babinet's principle, it was observed that the expression for ϵ_{eff} of complementary resonators is the dual of its counterpart, namely the μ_{eff}, of artificial magnetic materials. Through analytical and numerical studies, complementary resonators emulate materials with complex electric permittivity with negative real part above the inclusion's resonance frequency and positive real part below resonance. These findings are in contrast to artificial magnetic materials, which provide complex magnetic permeability with negative real part above the magnetic inclusion's resonance frequency and positive real part below resonance.

The developed inclusions will be incorporated in the next chapters to decouple antenna systems and mitigate electromagnetic noise and undesirable radiation from high-speed printed circuit boards, enclosures and apertures.

Chapter 4

Mutual Coupling Reduction Between High-Profile Antennas

4.1 Introduction

In Chapter 2, amongst the sources of mutual coupling in highly-coupled high-profile antenna systems, displacement currents are one of the challenges that affect performance of such antennas. The challenges lie on the deterioration of not only the matching of the antenna elements, but also the strong mutual interaction between the radiators. In this chapter, developed electromagnetic media are used to reduce the mutual coupling between highly-coupled monopole antennas.

The chapter is organized as follows. Section 4.2 introduces artificial magnetic materials as a decoupling layer to isolate highly-coupled monopole antenna elements. Section 4.3 presents both numerical and experimental setup models for the mutual coupling analysis. In section 4.4, the performance of the antenna system is presented, discussed, and numerical results are compared with measurements. Furthermore, the potential use of the monopole antenna system with the proposed decoupling network in Multiple-Input Multiple-Output (MIMO) communication systems is discussed, and studied by evaluating several metrics in MIMO systems. The effectiveness of the proposed decoupling layer is also studied experimentally. A conclusion based on the findings is summarized in section 4.5.

4.2 Artificial Magnetic materials for decoupling high-profile antennas

In this section, the concept of using the developed artificial magnetic materials (AMMs), presented in Chapter 3, as a decoupling layer will be presented. Let us consider highly-coupled high-profile antennas that are placed in free-space. For simplicity, two antenna elements shall be considered in this analysis. The model comprising the two antennas with the coupling path, as shown in Fig. 2.3, is analyzed systematically in terms of scattering parameters for ease of analysis. It will be show later that the magnetic resonators indeed work as a decoupling network, in which the mutual impedance should be purely reactive at the resonance frequency in order to decouple the antenna elements (i.e., Re(Z_{ij})=0 at resonance.) Such a condition is necessary for the existence of a decoupling network. This necessary condition had been discussed and verified in [15][16], [120]. The two antenna elements as a two-port linear network have the following scattering parameters

$$\begin{bmatrix} V_1^- \\ V_2^- \end{bmatrix} = \begin{bmatrix} S_{11} & S_{12} \\ S_{21} & S_{22} \end{bmatrix} \begin{bmatrix} V_1^+ \\ V_2^+ \end{bmatrix}, \tag{4.1}$$

where S_{ij} $(i \neq j)$ represents the coupling path between the two elements, as designated in Fig. 2.3. Let us assume that the two coupled antennas are lossless, reciprocal, matched and have poor isolation (strong coupling) (i.e, $S_{ii} = 0$.), then equation 4.1 becomes

$$\begin{bmatrix} V_1^- \\ V_2^- \end{bmatrix} = \begin{bmatrix} 0 & S_{12} \\ S_{12} & 0 \end{bmatrix} \begin{bmatrix} V_1^+ \\ V_2^+ \end{bmatrix}. \tag{4.2}$$

From equation 4.2, it follows that the mutual impedance Z_{ij} for the antenna system, $(i \neq j)$ should be reactive. Note that this condition holds quite often at a single resonant frequency, but nonetheless, it could be satisfied over a frequency band depending on the designed decoupling network [15].

4.3 Experimental and Numerical Setups

Fig. 4.1 shows the schematic of two monopole antennas separated by a distance of d=λ/8, where λ is the wavelength corresponding to the resonant frequency of the separate monopole antennas. The two antennas have been designed to operate at a frequency of 1.24 GHz. A finite copper ground plane of size 1.25λ x 1.25λ is used. Stacks of MNG inclusions, as designed and discussed in Chapter 3, are aligned vertically between the two monopole antennas. In this work, 4 SRR inclusion pairs are etched on both sides of the dielectric substrate. The periodicity of the magnetic inclusions is an important parameter

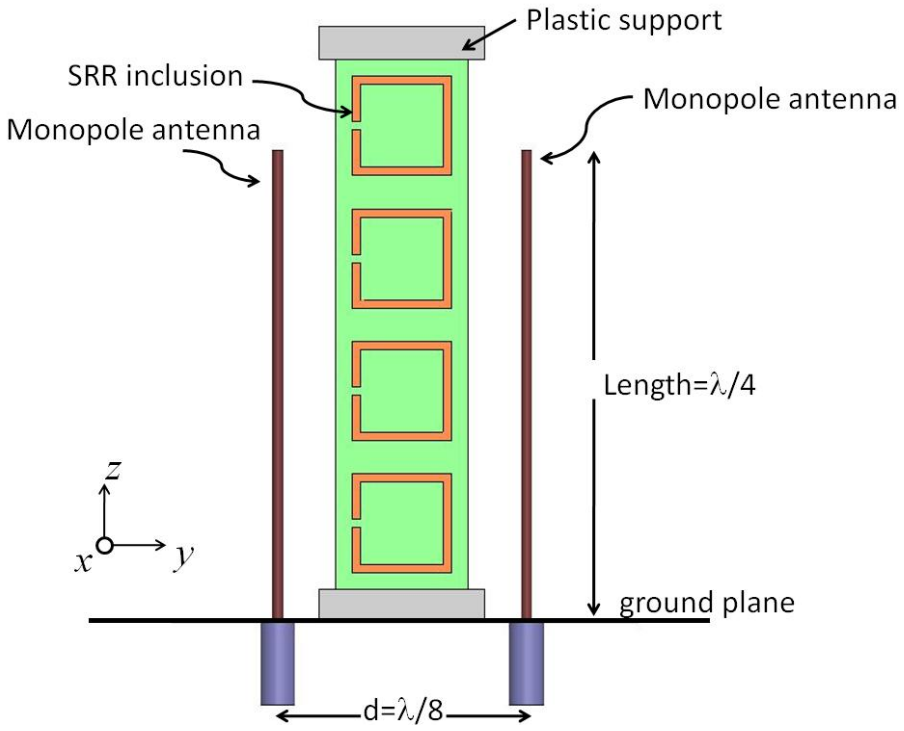

Figure 4.1: Lateral view of the two-monopole antennas with SRR inclusions. Distances are given in terms of an operational wavelength $\lambda = 240mm$. The plastic support is not shown for clarity purposes.

in the design of such inclusions, and it needs to be much smaller than the operating wavelength. The separation distance between each strip of the developed magnetic inclusions (see Fig. 4.1), corresponds to an electrical thickness of $\lambda/15$ at the resonance. The developed MNG inclusions have high permeability values around the resonance frequency. Those high permeability values enhance the inclusions resonance frequency and sustain much of the induced magnetic field within the MNG layer.

As mentioned earlier, the antenna mutual impedance should be purely reactive at resonance with its real part being nearly zero at resonance. In order to show that condition, a numerical model comprising two monopole antennas with the artificial magnetic decoupling layer is made (see Fig. 4.1). The two antenna system with and without magnetic inclusions are compared.

Fig. 4.2(a) shows the reactive part of the computed mutual impedance, Z_{12}, between the two monopoles with and without the magnetic decoupler layer. Around the resonance of the decoupling network, the reactive part is inductive, while it is capacitive over the antenna frequency band for the air case. Fig. 4.2(b) shows the real part of the mutual impedance Z_{12}. It is noticed that the computed resistances do not turn out to be exactly

zero at resonance. Those losses are mainly due to the losses within the MNG decoupling network. It is worth mentioning that the necessity condition in [15] was provided particularly for lossless decoupling networks. The decoupling network presented here is based on magnetic resonators, which are lossy and inherently narrowband [25], [121].

The model setup for the monopole antennas, shown in Fig. 4.1, was fabricated using two brass rods of length $57mm$ and diameter of $1.3mm$, soldered to 50 Ω coaxial (SMA) connectors. Fig. 4.3 shows the fabricated model with the artificial magnetic layer. Fig. 4.4 shows the reflection coefficient of the antenna system, S_{11}, obtained using an HP8722ES Vector Network Analyzer (VNA), and Fig. 4.5 shows the mutual coupling, S_{21}, between the two antenna elements. A two-antenna system with no spacer (air case) is used as a reference for comparison purposes. Another case when placing a PEC screen between the antenna elements is considered for completeness, although it seems very intuitive from a PEC screen to reflect back incident waves. In order to sustain the SRR inclusions in a vertical position, a plastic support layer ($\epsilon_r = 2.7$, $\tan\delta = 0.007$) has been used. The inclusions were sandwiched within the plastic holder with a uniform gap spacing between the MNG strips of $16mm$ (see Fig. 4.3). Note that the spacing between the SRR inclusions corresponds to the spacing used in the characterization model of the MNG unit cell in chapter. 3. The scattering parameters have been computed using HFSS and compared with measurements.

Due to computational memory constraints, the effective response of the magnetic inclusions (Fig. 3.10 in chapter. 3) was used in the numerical models in order to mimic the response of the magnetic inclusions. The artificial magnetic structures are in general inherently dispersive and anisotropic. The MNG materials considered in this work are based on the BC-SRRs [102]. Such inclusions provide enhanced permeability only in the direction normal to the inclusions plane (x-direction in Fig. 4.1), and enhanced permittivity in the directions tangent to the plane (y- and z-directions in Fig. 4.1). In this work, the orientation of the magnetic inclusions is assumed in yz-plane, as shown in Fig. 4.1. In such a case, the effective permeability and permittivity of the magnetic structures can take the following tensor forms, respectively

$$\mu(\omega) = \mu_0 \begin{pmatrix} \mu_{xx}(\omega) & 0 & 0 \\ 0 & 1 & 0 \\ 0 & 0 & 1 \end{pmatrix}, \tag{4.3}$$

$$\epsilon(\omega) = \epsilon_0 \begin{pmatrix} \epsilon_{avg} & 0 & 0 \\ 0 & \epsilon_{yy}(\omega) & 0 \\ 0 & 0 & \epsilon_{zz}(\omega) \end{pmatrix}, \tag{4.4}$$

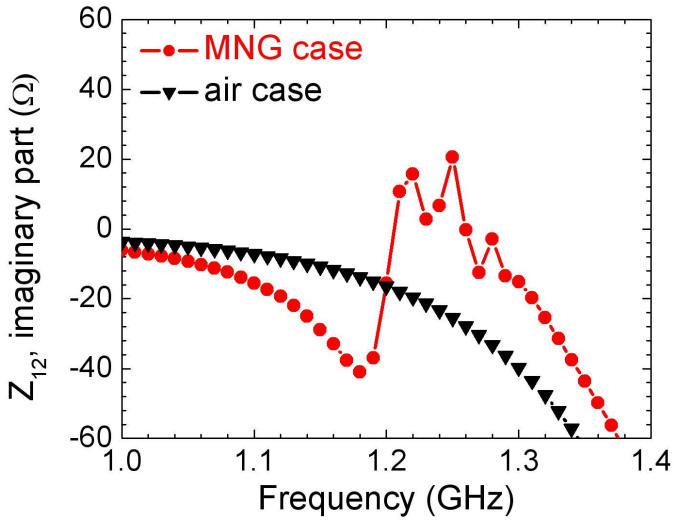

(a)

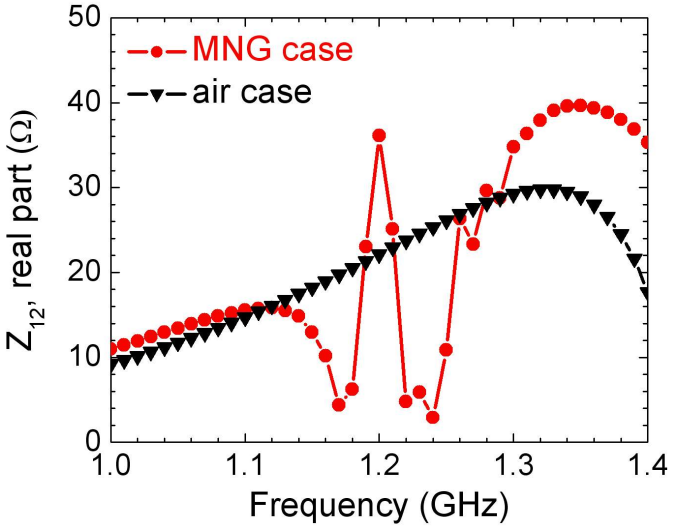

(b)

Figure 4.2: Computed mutual impedance, Z_{12}, between the two monopole antennas with and without the MNG decoupling network: (a) reactive part and (b) resistive part.

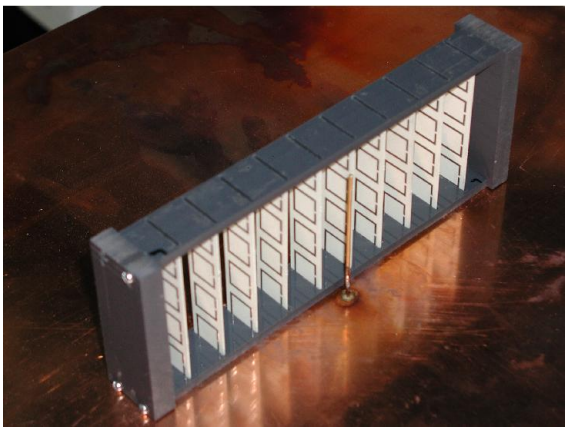

Figure 4.3: Fabricated monopole antenna system with the MNG inclusions. Note that one monopole antenna is visible and another antenna element is behind the MNG layer.

where ϵ_{avg} represents the averaged permittivity between the host medium (ϵ_{r1}=3.48 with a slab thickness of $d_1 = 0.762mm$) and air gaps between successive MNG strips (ϵ_{r2} = 1.0 with an air-gap thickness of $d_2 = 16mm$ - d_1).

It is instructive to note that within the numerical models, effective response of the constitutive parameters need to be carefully oriented. In more details, the effective permeability in the (x,y,z) directions correspond to ($\mu_{xx}(\omega)$,1,1), while the effective permittivity response corresponds to (ϵ_{avg},$\epsilon_{yy}(\omega)$,$\epsilon_{zz}(\omega)$) in (x,y,z) respectively, as can be seen from 4.3 and 4.4.

4.4 Experimental and Numerical Results

4.4.1 Scattering parameters

By placing the MNG inclusions between the antenna elements, the mutual coupling S_{21} has been reduced by almost 15 dB at the resonance frequency, while at the same time maintaining good impedance matching (i.e., $|S_{11}| \leq$ -10 dB) for the two-antenna system as shown in Fig. 4.4. The high μ values below resonance of the MNG inclusions have contributed to the mutual coupling suppression, where the transmission coefficient, S_{21}, starts to drop below -10 dB around 1.17 GHz. Moreover, the negative μ values above resonance have stronger influence on the mutual coupling suppression. This is attributed to the existence of evanescent fields within the negative region of the magnetic inclusions (i.e., above resonance), which then blocks the electromagnetic energy from being transmitted from one antenna element to another. A sizeable dip of S_{21} (below -40 dB) is noticed at a frequency of 1.22 GHz. We note here that the antennas without magnetic

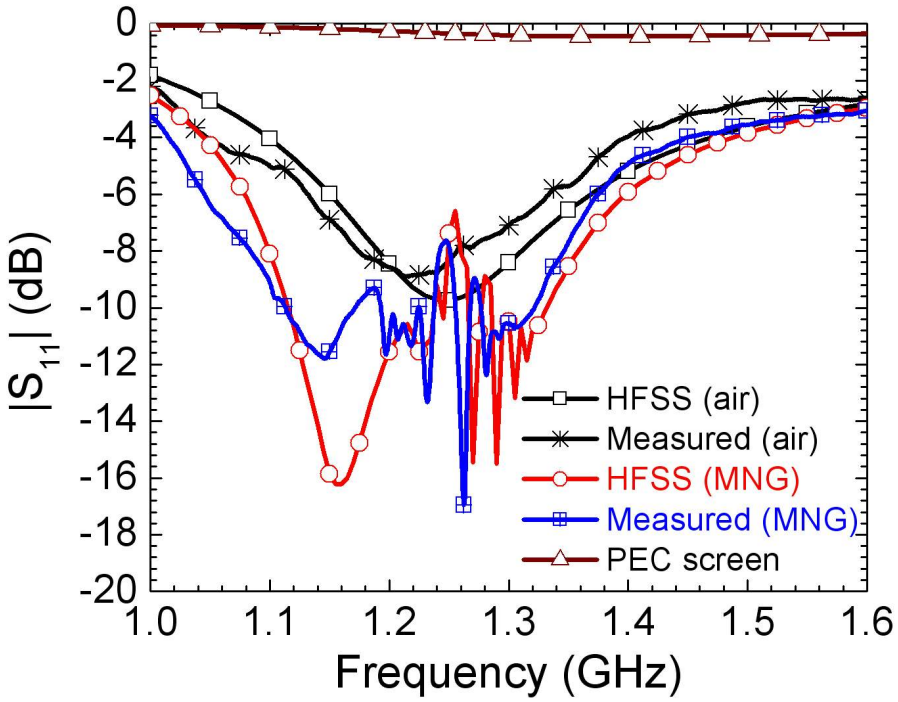

Figure 4.4: Measured and simulated S_{11} for the monopole antenna system with and without the MNG metamaterial slab.

inclusions (air case) were not well-matched due to the strong mutual coupling between the two monopole antennas. Good agreement between the numerical results and experimental ones can be seen.

The modeling of the effective response of the developed MNG inclusions, rather than modeling the real structure shows its effectiveness from both computational time and memory requirements. The mutual coupling suppression level achieved as a result of using the BC-SRRs inclusions is higher than the suppression level presented in [22], especially at the antennas' resonance. Most interestingly, however, is that unlike [22], the antennas in this work are well matched at the operating frequency despite the severe limitation placed on their separation distance. (The antennas were separated by a distance of only 0.125λ, and in another case 0.1λ. In terms of the operating wavelength, the separation distances between the antennas considered here were relatively smaller than the antennas separation distance, 0.156λ given in [22].)

The field generated by antennas can be considered as a superposition of evanescent and propagating waves. The interaction between antennas is a combination of the effects of these plane wave components. In order to eliminate the coupling, the propagating waves and the evanescent components with low decay constants must be suppressed. To analyze the relevant evanescent spectrum, we assume that coupling due to the evanescent compo-

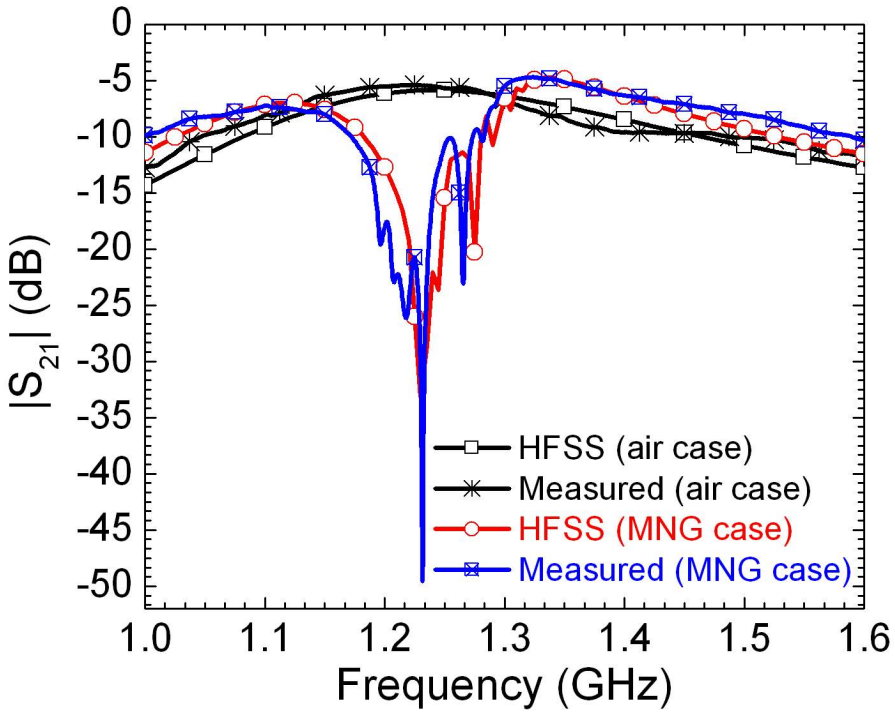

Figure 4.5: Measured and simulated S_{21} for the monopole antenna system with and without the MNG metamaterial slab.

nents that decay more than 10 times within a $\lambda/8$ distance can be ignored. Therefore the evanescent fields that satisfy $e^{-k_y \lambda/8} < 0.1$ are ignored, where k_y is the y component of the wave vector (see Fig. 4.1). Using dispersion relation and the assumption stated above, it can be deduced that the components that cause the interaction between the antenna elements are both the evanescent and propagating waves with $\sqrt{k_x^2 + k_z^2} < 0.8$ rad/cm. As a result the minimum spatial wavelength in the x-z plane to be suppressed is $\lambda_{min} = 2\pi/0.8$ = 7.85 cm. Since the periodicity of the developed magnetic inclusions is smaller than λ_{min} (i.e., around $\lambda_{min}/5$), the MNG layer can be assumed as an effective homogenized medium for these components.

4.4.2 Far-field

Far-field radiation patterns for the monopole antennas with and without the effective response of the MNG metamaterial slab are numerically computed using HFSS. In the numerical simulation, one antenna was connected to a 50Ω coaxial (SMA) connector while the other element is terminated with a 50Ω load. Fig. 4.6 shows the far-field pattern for the two antennas with and without the magnetic inclusions. The computed results (see Fig. 4.6(a)) show that the use of MNG inclusions enhances the antennas' potential

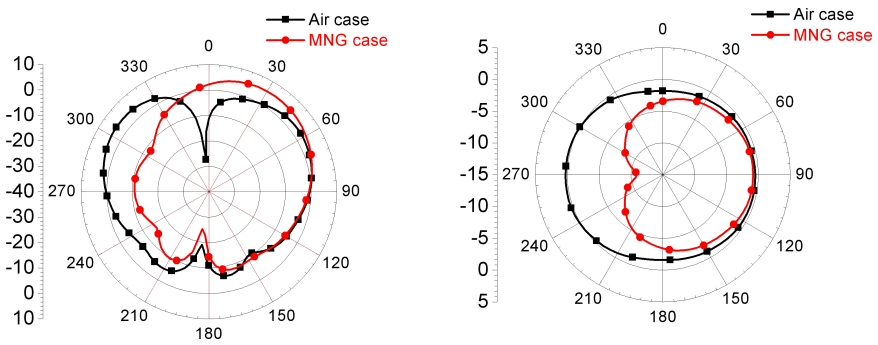

(a) (b)

Figure 4.6: Simulation results for far-field patterns for the two monopoles with and without magnetic inclusions at 1.22 GHz (a) E-plane (yz-cut, ϕ=90°) (b) H-plane(xy-cut, θ=90°)

to steer or concentrate energy into a more specified direction, thus increasing the gain in specific directions, whereas the counterpart antenna system (i.e., antennas without SRRs) yield the typical donut shape. For the resonant frequency of 1.22 GHz, the gain has increased from 4.2 dB for the air case to 5.6 dB for the case when SRR magnetic inclusions were used between the two antennas. Fig. 4.6(b) shows the gain in the H-plane (xy-plane, θ=90°) for the aforementioned cases. It is observed that the MNG layer helps in achieving quasi-orthogonal pattern and reducing the back radiation in comparison to the air case. Fig. 4.7 shows the far-field patterns for the two antenna elements with MNG inclusions at frequency of 1.2 GHz. The antenna system achieve quasi-orthogonal patterns when using the magnetic inclusions. Due to the nature of the magnetic resonators losses, the radiation efficiency of the antenna system with magnetic inclusions layer dropped to 60% at the SRR's resonance of 1.24 GHz. Despite the encountered losses, the gain has been enhanced when using the magnetic inclusions at 1.2 GHz and 1.22 GHz where the radiation efficiency was almost 93% and 80% respectively.

4.4.3 MIMO performance metrics

In recent years, there has been a tremendous interest in the so called MIMO communication technology. MIMO stands for Multiple-Input Multiple Output. In its simplest form, MIMO systems rely on the use of multiple transmitters and multiple receivers in a communication environment that allows for significant increase in noise immunity (improved signal-to-noise ratio, SNR) and enhanced performance (capacity). In many outdoor and indoor wireless communication environments, there are many obstacles and scatterers, like buildings, mobile terminals, and offices...etc. A problem that is encountered in such

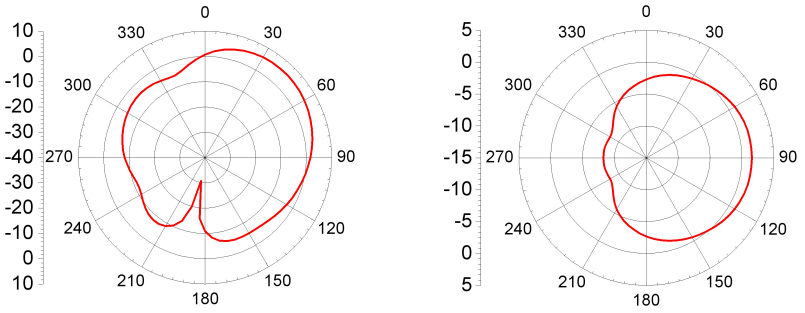

(a) (b)

Figure 4.7: Simulation results for far-field patterns for the two monopoles with magnetic inclusions at 1.2 GHz (a) E-plane (yz-cut, ϕ=90°) (b) H-plane (xy-cut, θ=90°)

Figure 4.8: Schematic representation of a MIMO communications system.

environments is multipath fading. Fading can be defined as a behavior that results in transmission/reception degradation of an electromagnetic energy due to any of the aforementioned obstacles. This fading phenomenon limits the performance and capacity of the antenna system, by introducing noise in the form of destructive interference and hence reduced received power (decreased SNR). One such mechanism to combat that multipath fading is to use multiple antennas at either transmit (MISO), receive (SIMO) or both ends (MIMO) as shown in Fig. 4.8.

In a rich scattering multipath environment, transmitted information from each antenna terminal takes its own path (or set of paths depending on the obstacles) independently of each others. This means that the likelihood that signals would destructively interfere in such scenarios is much lower than the interference that results from transmitting signals in just one path. This is the advantage of employing MIMO systems in rich-scattering environment, simply the greater the scattering, the higher the likelihood the transmitted signals will fade independently, and thus higher received SNR. An as-

sumption that is made in the above discussion is that the signal paths (channels) are uncorrelated over which antennas transmit/receive signals. This can be achieved ideally when antennas are placed far-apart from each others (usually more than half a wavelength). However, in practice, antennas are often correlated. With recent technologies nowadays, antenna systems design is subject to the available packaging volume depending on the applied technology. Therefore, antenna elements become highly correlated when placed in close-proximity. Thus, quantitative measure of the correlation between any two antennas within the array is often required and need to be kept as low as possible. This correlation metric can be defined as a statistical measure of similarities between any two signals; the higher the similarities, the higher the correlation. In antenna systems, the correlation metric between two or more antenna elements can be expressed using far-field components [5], mutual impedances between the antenna elements [122]-[123], or directly from the scattering parameters measured at the ports [124]. Under the assumption of uniform incident waves impinging on the antenna system in the azimuth plane and lossless antenna system [124], the envelope correlation can be calculated from the scattering parameters much more readily than from the far-field patterns. In this work, the use of scattering parameters is incorporated in the envelope correlation computation and compared with that using the far-field method [5].

The envelope correlation ρ_e of a two antenna system using the far field method [5] can be calculated using

$$\rho_e = \frac{\left| \iint\limits_{4\pi} \left[\overrightarrow{F_1}(\theta,\phi) \cdot \overrightarrow{F_2^*}(\theta,\phi) \right] d\Omega \right|^2}{\iint\limits_{4\pi} \left| \overrightarrow{F_1}(\theta,\phi) \right|^2 d\Omega \iint\limits_{4\pi} \left| \overrightarrow{F_2}(\theta,\phi) \right|^2 d\Omega}, \tag{4.5}$$

where $\overrightarrow{F_i}(\theta,\phi)$ represents the field radiation pattern of the antenna system when port i is excited and all other ports are terminated in a matched 50 Ω load [124], and $\cdot$ is the Hermitian product. The envelope correlation based on the scattering matrix can be calculated using [124]-[125]

$$\rho_e(i,j,N) = \frac{|\sum_{n=1}^{N} S_{i,n}^* S_{n,j}|^2}{\prod_{k=i,j}[1 - \sum_{n=1}^{N} S_{k,n}^* S_{n,k}]}. \tag{4.6}$$

In the case of a 2 x 2 MIMO system (N=2), the envelope correlation between antenna element i=1 and j=2 is given as

$$\rho_e(1,2,2) = \frac{|S_{11}^* S_{12} + S_{21}^* S_{22}|^2}{[1 - (|S_{11}|^2 + |S_{21}|^2)][1 - (|S_{22}|^2 + |S_{12}|^2)]}. \tag{4.7}$$

It is worth mentioning that several assumptions in aforementioned equations are considered. One important issue is that the deployed antenna system is lossless in equation (4.6). Another matter is that the impinging electromagnetic energy in the antenna system (receiver) arrives uniformly from all angles in the azimuth plane. The spread of the incident electromagnetic wave is mainly dependent on the environment (obstacles, buildings...etc), and this spread phenomena is known as *power angular spectrum* (PAS). This PAS would appear in both the numerator and denominator of equation (4.5. In the ideal case of rich scattering environment, described by an equally likely incidence of power from all angles, the PAS can be assumed constant.

The envelope correlation ρ_e for the antenna system with the MNG inclusions is computed using equation (4.6) and compared with the far field formula in (4.5). Results presented in Fig. 4.9 show comparison with the case without spacers between the antennas. Good agreement between the envelope correlation computed using the scattering parameters formula (4.6) and that obtained using the far field method (4.5) can be seen for the air case. The computed envelope correlation was above 0.3 in average. From Fig. 4.9, the envelope correlation results using equation (4.6) for the MNG case shows low correlation between the antenna elements below 0.2 over the antennas frequency band as compared to the air case. The correlation then starts to increase after 1.3 GHz, which corresponds to diminishing of the mutual coupling suppression when using the developed magnetic inclusions (see Fig. 4.5). It is important to emphasize here that the increase in envelope correlation beyond 1.3 GHz will result in non-orthogonal radiation patterns. Nonetheless, the 1.3 GHz is at the edge of the operational band of the two-monopole antenna system. The envelope correlation results obtained using equation (4.5) show that the antenna elements are well-decorrelated below 0.1 for frequencies up to 1.25 GHz where losses of the magnetic inclusions are inherently pronounced above 1.25 GHz.

An important conclusion based on the assessment of the envelope correlation between antennas is that the scattering matrix based formula is not fully descriptive, especially in situations when lossy decoupling networks are placed between the coupled antenna elements, which is simply because the evaluation of correlation based on the scattering parameters do not account for the the antennas efficiency. Similar observations were reported in [125].

Although the difference between envelope correlation calculations is attributed to the electromagnetic loss of the MNG material, Figs. 3.10 and 4.9 show that the deviation between envelope correlation calculations correspond to the frequencies where the loss tangent of the MNG material is low. This counter intuitive observation is explained as follows. The first thing to note is that the decay and energy dissipation relation in the

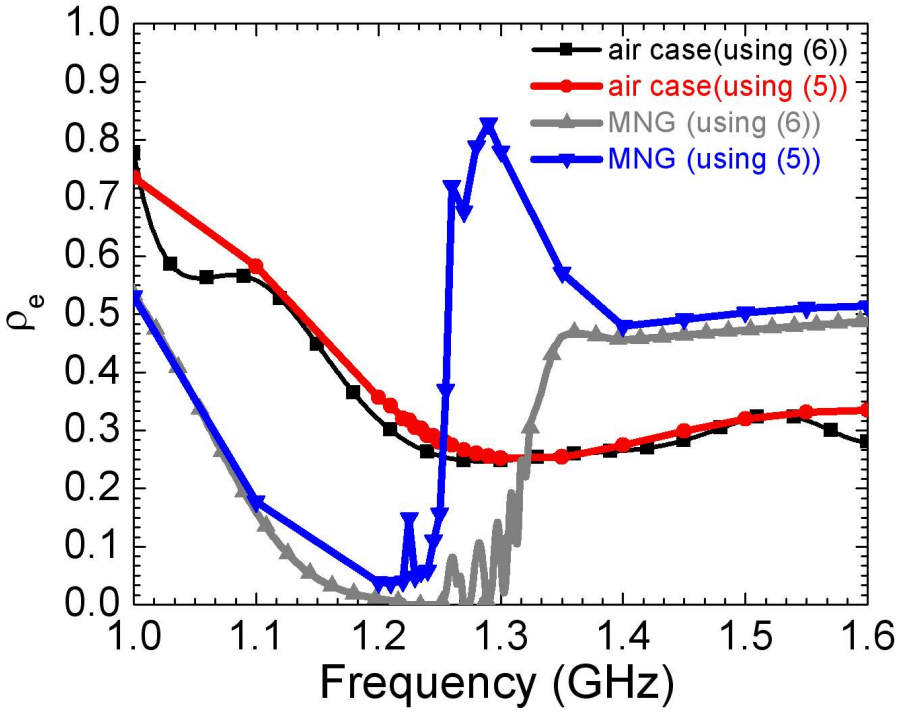

Figure 4.9: Simulation results for the envelope correlation, ρ_e, for the monopole antenna system with and without MNG inclusions.

case of a regular double positive lossy material is different than the relation in the case of a single negative material. Therefore, a straight forward relation between the imaginary part of the μ and the electromagnetic loss within the negative material that states "the higher the imaginary part, the higher the loss" is not correct in all cases. Basically, the decay within MNG material is a result of the high negative value of the real part of the μ. When the real part of μ is highly negative, the field is suppressed faster and the field would not penetrate to the MNG material. Therefore, the amount of the field within a slab with highly negative real μ is not as much as the amount of the field within a MNG material with negative μ closer to zero. As a result, even if the imaginary part is higher for highly negative MNG materials, they do not dissipate as much energy as MNG materials which have a negative μ closer to zero. This behavior is also affected by the thickness of the slab and the mode, direction and evanescence of the incident field. This phenomenon is described in Fig. 4.10, where the electric field intensity is plotted within the MNG material at different frequencies. Although the imaginary part is lower at higher frequencies, since the field penetrates more, it is possible to lose more energy. Note that for the presented plot, it is assumed that the incident field is a TEM plane wave.

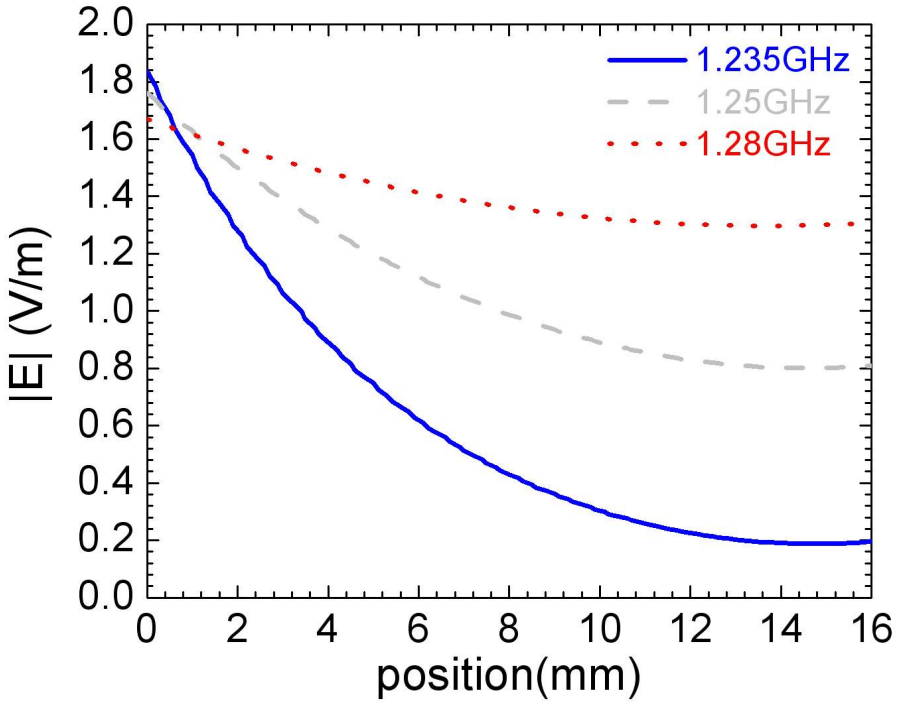

Figure 4.10: Calculated electric field intensity within the MNG material at several frequencies.

In addition, the total power consumed within the artificial magnetic layer (using the retrieved effective medium parameters) was calculated using CST MWS and presented in Fig. 4.11. The power consumption is high at higher frequencies although the imaginary part of the permeability is lower.

4.4.4 MNG decoupler effectiveness

The effectiveness of the MNG as an antenna decoupler is experimentally investigated. Parametric analysis based on varying the number of MNG strips is considered. Results are shown in Fig. 4.12. It is observed that by inserting 2 strips of the MNG inclusions, the effectiveness of such materials in suppressing the mutual coupling is diminished. However, when using 8 strips, a minimum of 44 dB suppression was achieved, and the 10 strips case is as illustrated before and shown in Fig. 4.5. The diminished mutual coupling observed when using 2 MNG strips is due to the weak induced magnetic field that is not homogenized enough to excite the MNG layer. The case of 8 MNG strips has resulted in more homogenized induced magnetic field; an indication of such behavior is seen from the high suppression of S_{21} below -30 dB. A parametric study was also

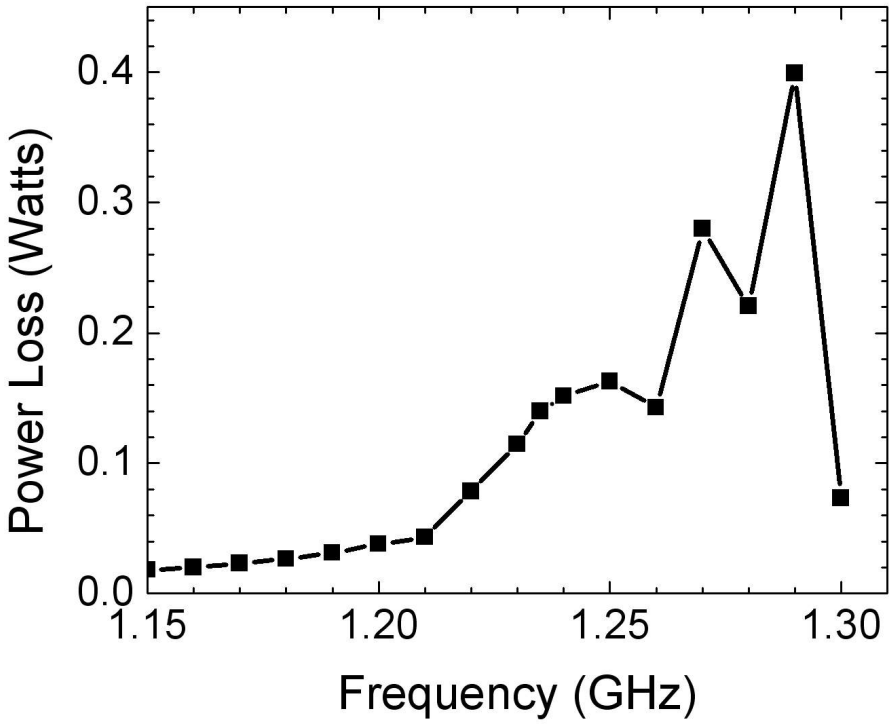

Figure 4.11: Power loss within the MNG layer computed numerically using the full-wave solver of CST MWS.

conducted to investigate the effects of varying the number of MNG strips on the envelope correlation between the antenna elements, as shown in Fig. 4.13. This has been conducted numerically using the far-field formulation at a frequency of 1.22 GHz. It is observed that the use of 8 MNG strips is sufficient to achieve low correlation between the two antenna elements below 0.25. The noticed discrepancy arises due to the minimal mutual coupling suppression that results when using less number of MNG strips (for example, number of MNG strips below 6.)

Fig. 4.14 illustrates how the displacement current is mitigated using the developed single-negative magnetic materials. In order to show the effectiveness of the developed MNG inclusions, one of the antennas is fed while the other element is terminated with a 50 Ω load. Simulations using the HFSS full-wave solver are carried out in this context. Two normalized separation distances of $d/\lambda = 0.1$ and 0.125 are shown for two antenna elements with the developed MNG inclusions and compared with air case (no spacers). By placing the MNG layer between the two antennas, much of the radiated energy is blocked and no transmission of energy is observed within the MNG layer. The strength of the coupling path can be seen for the case of no spacers between the antenna elements, due to the strong mutual interaction between the antennas. The MNG layer effectively reduced

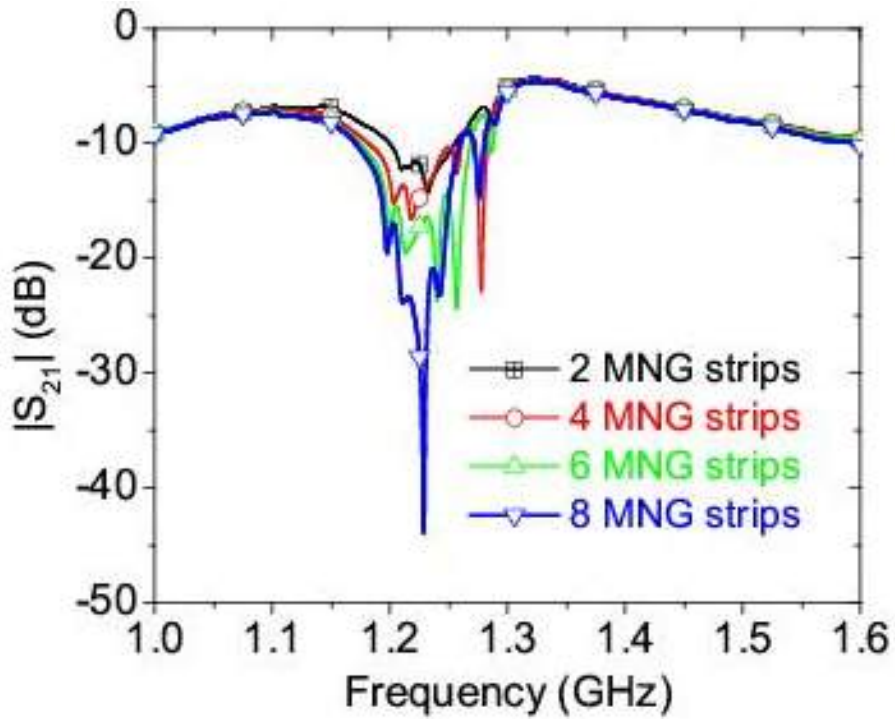

Figure 4.12: Parametric study for the measured mutual coupling between the monopole antenna elements when MNG strips are varied.

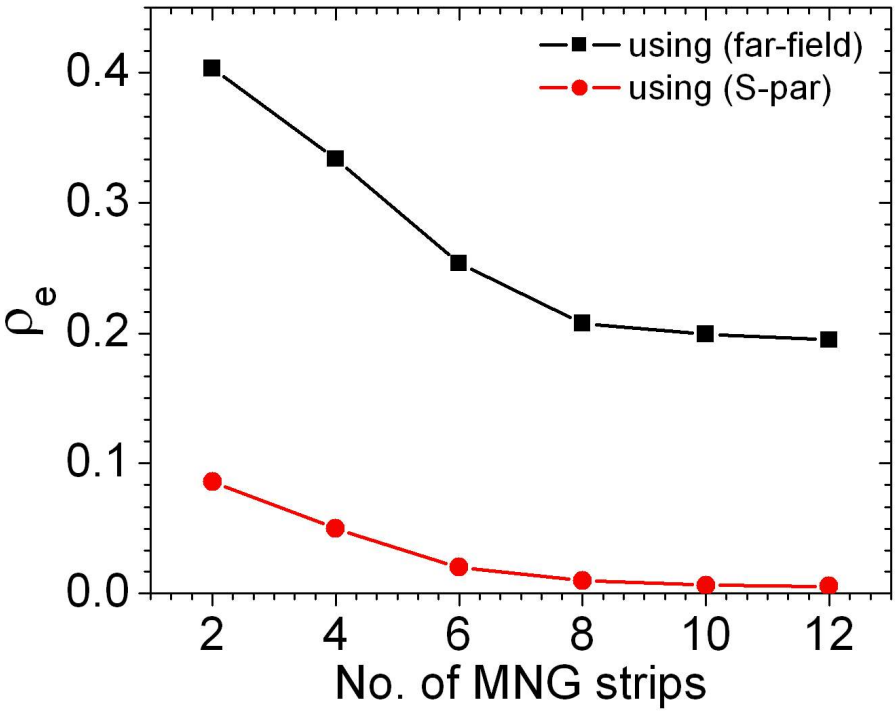

Figure 4.13: Simulation results for envelope correlation as a function of MNG strip layers.

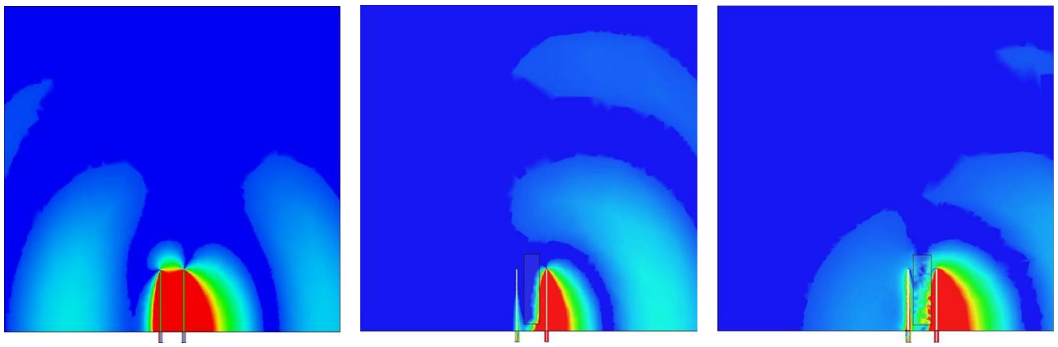

(a) (b) (c)

Figure 4.14: Simulation results for the magnetic field in the transverse plane (yz-plane) for the highly-coupled monopole antenna system: (a) without any spacers (d/λ=0.125, (b) with MNG layer (d/λ=0.125), and (c) with MNG layer (d/λ=0.1). A maximum scale of 1 A/m was used for the H-field strength for all the snapshots.

the mutual coupling between the antennas and mitigated the displacement current and as such the coupling path effect diminished.

4.5 Conclusion

In this chapter, mutual coupling between closely-packed high-profile monopole antennas is investigated. Artificial magnetic materials based on the modified split-ring resonators (M-SRRs) were developed and used to decouple the high-profile antennas.

Effectiveness of the magnetic inclusions was experimentally investigated with emphasis on the effect of number of MNG strips inserted between the monopole antenna elements. The decoupling layer showed its effectiveness in terms of reducing the mutual coupling and its shielding effectiveness in suppressing the displacement current. The MNG layer is an efficient magnetic shielding wall that can be advantageous in many antenna applications and EMI problems. Through numerical and experimental studies, it was shown that more than 20-dB reduction in mutual coupling between antenna elements was attainable. Moreover, good impedance matching can be achieved when using the MNG inclusions, unlike the case of no decoupling layer.

Chapter 5

Mutual Coupling Reduction Between Low-Profile Antennas

5.1 Introduction

As discussed in Chapter 2, several mechanisms of mutual coupling tend to appear in low-profile antenna systems. Those sources of coupling vary on their strength depending on how far antennas are spaced apart, substrate's thickness and material properties, and ground plane size. In this chapter, mutual coupling between low-profile patch antennas is investigated. A cost effective technique based on complementary split-ring resonators (CSRRs), presented in Chapter 3, is proposed here in order to alleviate such coupling effects. The developed complementary unit cell will be referred to as the *slotted-CSRR* (SCSRR). Full-wave numerical analysis are carried out to investigate the effects of the SCSRR on the antenna system's parameters.

This chapter is organized as follows. Section 5.2 introduces a novel unit cell design based on artificial complementary resonators which were introduced earlier in Chapter 3. The analysis of the novel SCSRR unit cell is studied using dispersion analysis and constitutive parameters retrieval. Section 5.3 provides both numerical and experimental setup models proposed to decouple low-profile microstrip antenna systems. In section 5.4, numerical results are presented, discussed, and validated against fabricated prototypes. Finally, a brief summary is provided in section 5.5.

5.2 Complementary Resonators for Decoupling Low-Profile Microstrip Antennas

Complementary SRR (CSRR) structures were used for harmonic rejection and filtering [126]. The CSRR (see Fig. 5.1a) electromagnetic behavior is best understood by applying the duality principle to the magnetically resonant SRR structures [127]. As discussed in Chapter 3, the SRR based magnetic materials react to the vertically polarized (with respect to the SRR's plane) magnetic fields. Their resonance behavior is due to the induced electromotive force that induces a current which flows in the metallic rings and gaps producing a balanced inductive-capacitive effect. From duality, the CSRR exhibits resonant behavior in the presence of vertically polarized electric fields [3]. Therefore, such structures are particularly useful in an electromagnetic environment where the electric field is dominantly vertically polarized.

Fig. 5.1 shows the unit cells of the CSRR (Fig. 5.1a) and the new structure (Fig. 5.1b) SCSRR. The new configuration is implemented by etching away the copper sections from the ground plane. The fabrication does not require any modifications to the existing dielectric substrate. Consequently, the antenna remains low-profile and light weight and the far field properties are practically left unchanged.

The proposed structure as shown in Fig. 5.1b consists of two complementary SRRs connected with a slot of length L_s and width W_s. The new resonator is produced by bridging two traditional CSRR cells through a slot. The CSRR connected by a slot can be viewed as two cascaded filters. The slot in a ground plane has been well known to provide a low-pass response in a certain frequency range[128]. The dimensions of CSRRs and slots are adjusted so that their individual stop bands are connected in frequency, resulting in a wideband response. Eigenmode analysis was performed using the full-wave 3-D simulation tool CST MWS to demonstrate the filtering characteristics of the proposed structure. The corresponding Brillouin diagram for an infinite SCSRR structure is plotted along the Γ-X axis of the periodic structure as shown in Fig. 5.2. The dimensions of the SCSRR unit cells were estimated by computing the transmission coefficient and looking for zero transmission that corresponds to the rejection band of the proposed inclusion. The adopted characterization method is to place a microstrip line segment above a grounded dielectric with the new inclusion etched on it, similar to the characterization discussed in [126]. The dimensions of the tuned SCSRR unit cell are $L = 4mm$, $a = b = g = 0.2mm$, $L_s = 2mm$, and $W_s = 0.35mm$ (see Fig. 5.1) that provide a rejection band from 4 GHz to 5.1 GHz. The inclusions are etched on a dielectric substrate ($\epsilon_r = 3.48$, $tan\delta = 0.004$) with a thickness of $1.27mm$. The separation distance between the

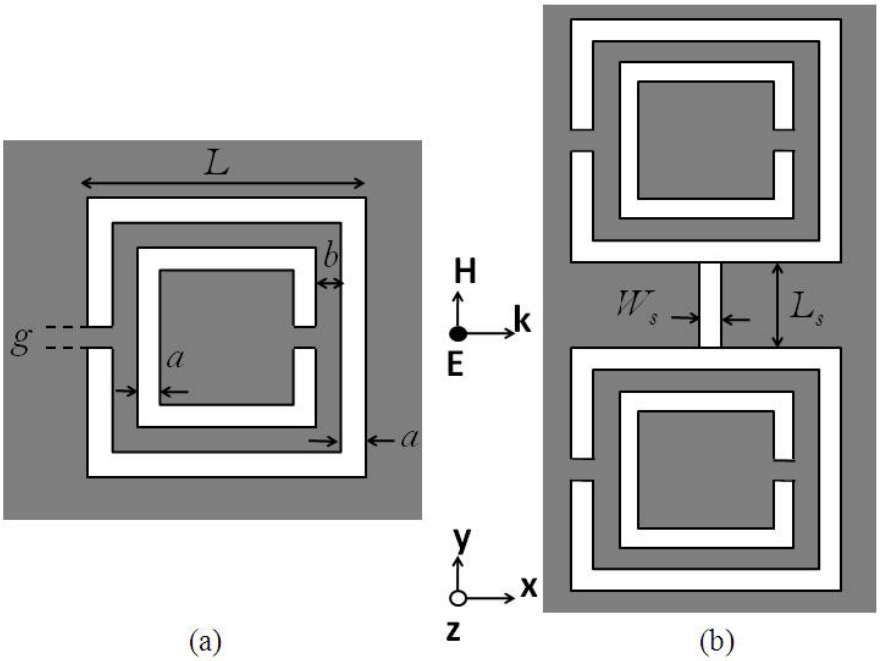

Figure 5.1: (a) Complementary-SRR unit cell, and (b) the proposed slotted-CSRRs unit cell. Note that gray shaded area represents metallization, and figure is not drawn to scale. **E**-field is normal to the axis of both complementary-SRR and SCSRR-slotted inclusions.

unit cells is $1mm$. Strong rejection characteristics are observed for the SCSRRs, where the bandgap zone is clearly seen within the designed frequency range. To demonstrate the effectiveness of the slot in comparison to the traditional CSRR cell, a comparative eigenmode analysis is given in Fig. 5.2. Clearly evident from Fig. 5.2, a larger unit cell ($4.5mm$ x $4.5mm$) is needed to achieve suppression around 5 GHz, resulting in a narrow rejection band of 0.1 GHz as compared to the 1 GHz rejection band of the SCSRR cell.

Based on Babinet's principle, the effective permittivity is enhanced for complementary resonators (i.e., the SCSRR in this work), unlike the artificial magnetic materials which have an enhanced magnetic permeability. The enhanced permittivity ϵ_{eff} is complex, with a negative real part above the SCSRR's resonance. The effective electric permittivity ϵ_{eff} of the SCSRR inclusion was numerically characterized using the method reported in [109], in a manner similar to the procedure outlined in Chapter 3. Interestingly, the negative part of ϵ_{eff}, as shown in Fig. 5.3, agrees well with the bandgap zone as obtained from the Brillouin diagram in Fig. 5.2. This validates the predictions that complementary resonators are single-negative media with enhanced ϵ_{eff}.

In order to investigate the effect of the slot in the proposed inclusion, the scattering parameters of a microstrip transmission line (TL) segment are computed when the TL

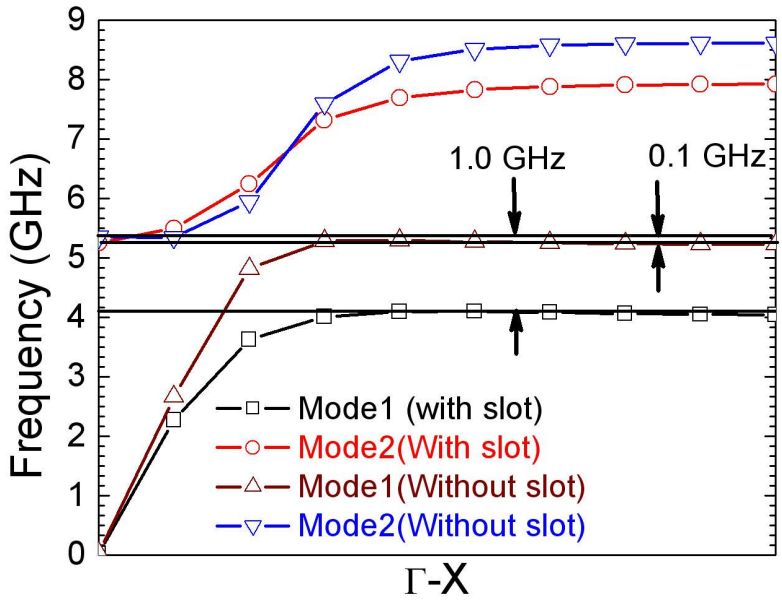

Figure 5.2: Dispersion diagrams for SCSRR and CSRR unit cells.

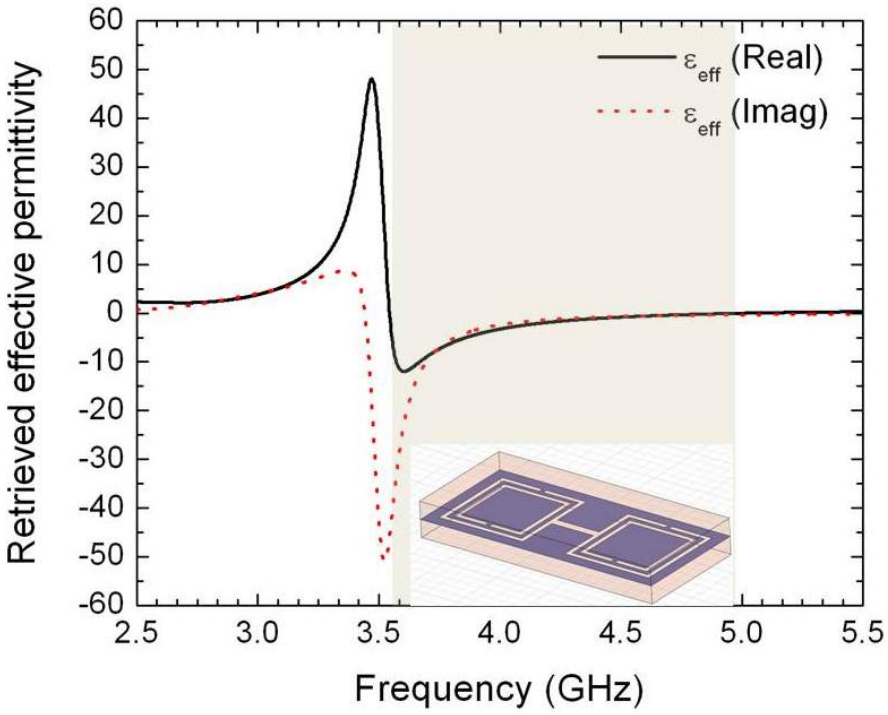

Figure 5.3: The retrieved effective permittivity for the SCSRR inclusion obtained using PEC-PMC boundary conditions to mimic an effective homogenized medium of SCSRR inclusions. Two ports were lunched to record the scattering parameters of the SCSRR inclusion, from which ϵ_{eff} was retrieved.

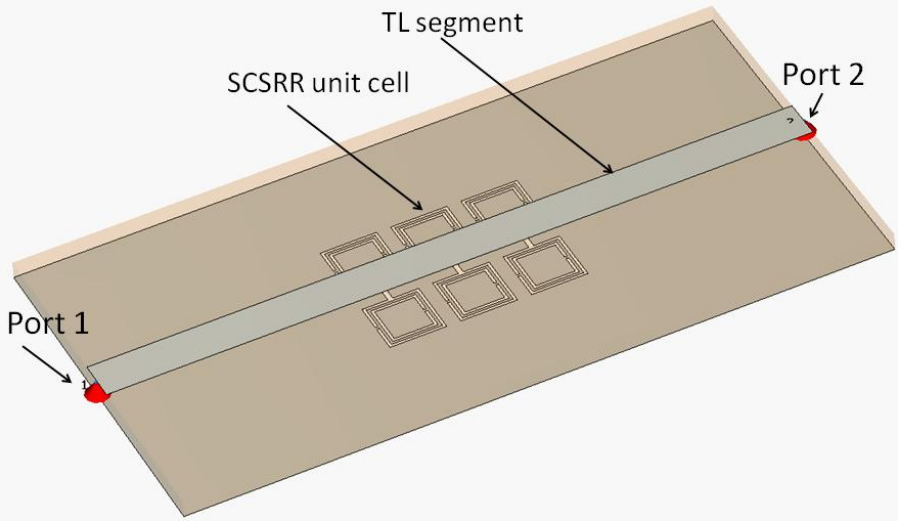

Figure 5.4: Numerical characterization model used to extract the bandgap of the proposed SCSRR structure using the transmission coefficient S_{12}. The model comprises a 50Ω microstripline placed over a dielectric substrate ($\epsilon_r = 3.48$, $\tan\delta = 0.004$, and thickness of $1.27mm$) backed by three SCSRRs unit cells in ground plane. The width of the transmission line segment is $2.88mm$.

is placed over the aforementioned dielectric substrate and backed by three SCSRR inclusions. The numerical characterization model used to study the effects of the SCSRRs parameters is as shown in Fig. 5.4. The structure is excited with a vertically polarized electric field and the resulting transmission coefficient is plotted in Fig. 5.5. Other complementary configurations (CSRRs) are also shown for comparison purpose. A suppression of 15 dB is maintained over the whole rejection band. The CSRRs particles have the suppression at around 4.9 GHz. However, the narrowband suppression of the CSRRs has resulted in mutual coupling reduction occurring above 5 GHz (see Fig. 5.11) due to the close proximity of the CSRR resonators to the patch antenna edges. A narrowband suppression is also observed for the proposed particles without the slot. The center frequency of the rejection band is controlled by the slot width W_s. A parametric study based on varying the slot width W_s shows that a decrease in the width of W_s causes the rejection band to shift to lower frequencies. This study is shown in Fig. 5.6.

Another measure to quantify the rejection characteristics of the proposed complementary resonator is to compute the attenuation constant. This particular coefficient provides quantitative measure of how easily a material can be penetrated by an electromagnetic wave. The larger the attenuation contact, the weaker the wave penetrates the medium. From the scattering parameters, the attenuation constant can be extracted as shown in Fig. 5.7, and indeed, it was found to be appreciable over the bandgap regime shown in

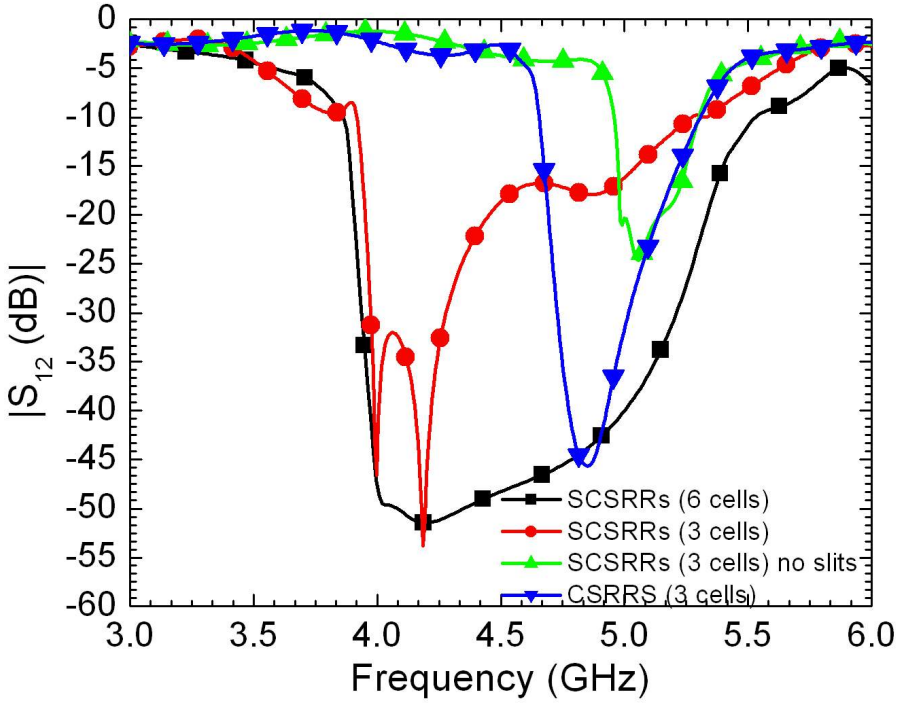

Figure 5.5: Simulated transmission coefficient S_{12} for the SCSRRs etched in the ground plane underneath the microstripline. Comparison is made with other designed configurations.

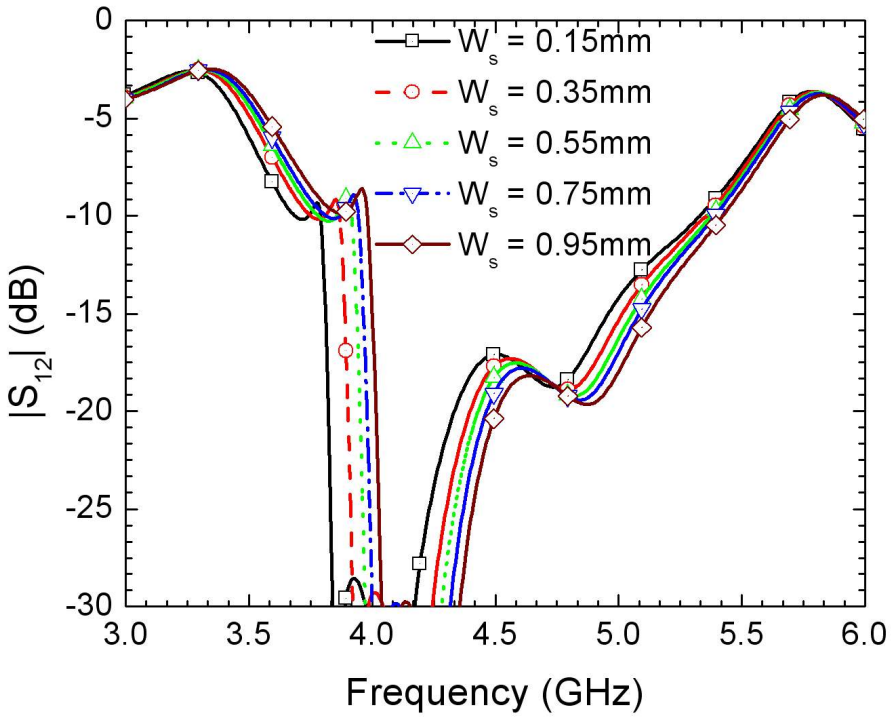

Figure 5.6: Simulated transmission coefficient S_{12} for various slot width W_s to study the effect of the slot on suppression bandwidth of the SCSRRs.

Fig. 5.2. While it should be noted that the electric field behavior under a microstrip line is not identical to that of the electric field within the substrate of the two antennas, the similarities exist in that a significant normal (to the ground plane) electric field component is present in the two scenarios.

5.3 Experimental and Numerical Setups

The set-up model used to demonstrate the mutual coupling reduction is shown in Fig. 5.8. Two identical planar microstrip antenna elements having a resonant frequency of 5 GHz, suitable for WLAN applications, are placed $0.25\lambda_0$ apart, where λ_0 is the free-space wavelength. The square patches have an area of $15mm$ x $15mm$ with the overall board size given by $1.3\lambda_0$ x $1.0\lambda_0$. The antennas are printed on a dielectric substrate (ϵ_r = 3.48, $tan\delta$ = 0.004, and thickness $h = 1.27mm$). As shown in Fig. 5.8, the SCSRRs are etched out in such a way that the ΓX axis of the periodic structure (see Fig. 5.2) coincides with the line joining the center of the two patch antennas. This configuration ensures the suppression of the vertically polarized electric fields (space-waves) between the two patches. The transmission coefficient between the two patches is determined to gauge the

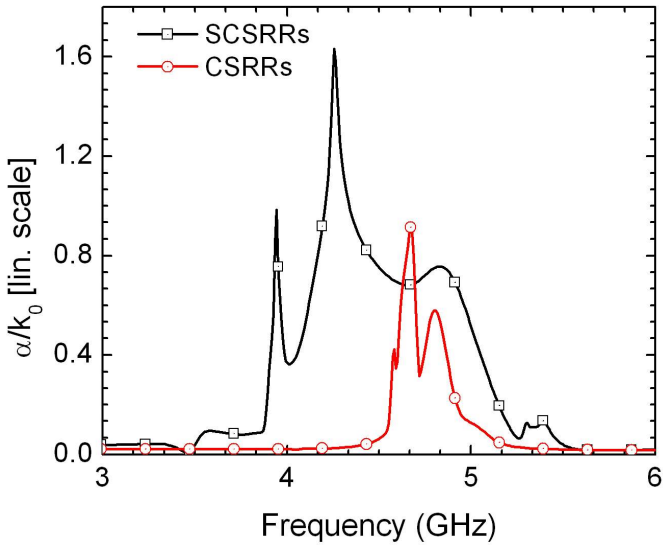

Figure 5.7: Normalized attenuation constant computed numerically for the microstrip line structure with SCSRRs and compared with CSRRs.

mutual coupling effect. Figs. 5.9- 5.10 show photos of the fabricated low-profile antenna system with and without the complementary resonators.

5.4 Experimental and Numerical Results

5.4.1 Scattering parameters

Fig. 5.11 depicts the simulation results for the mutual coupling between the two patch antennas with and without the SCSRR inclusions. A reduction of about 10-dB in the mutual coupling between the antennas is achieved. The mutual coupling between two patches when using 3 cells of CSRRs is also shown for comparison. It is observed that the use of CSRRs results in mutual coupling reduction between the radiating elements above 5 GHz. This is in agreement with the dispersion diagram shown in Fig. 5.2.

Figs. 5.12-Figs. 5.13 show simulated scattering parameters obtained using CST MWS and compared with measurements for the two antenna system with and without SCSRRs. A slight shift (less than 1.5%) between simulated and measured scattering parameters was observed. This is attributed to the SMA connectors which were not accounted for in the numerical models.

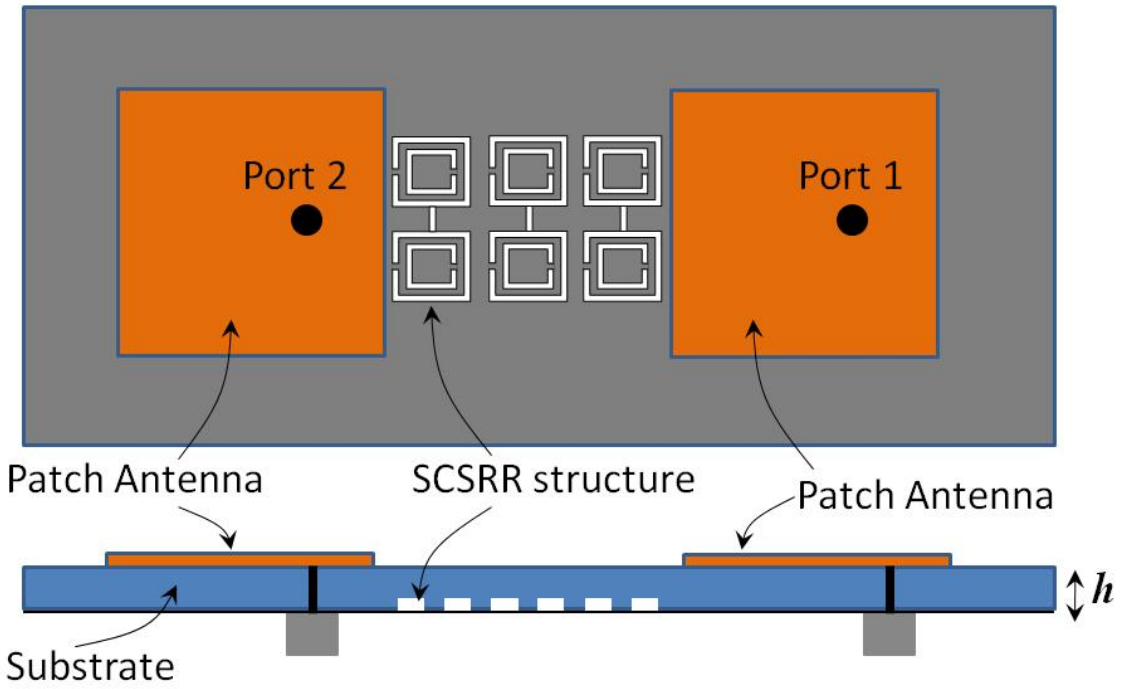

Figure 5.8: Top and side views for the two patch antennas with the SCSRR etched on the ground plane. Note that gray area represents ground plane metallization.

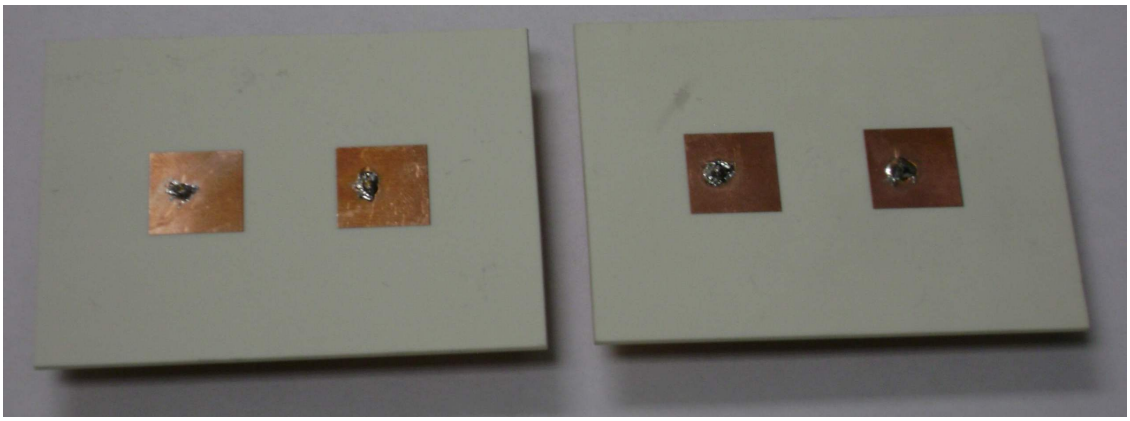

Figure 5.9: Top view of the fabricated low-profile antenna system with and without SCSRRs.

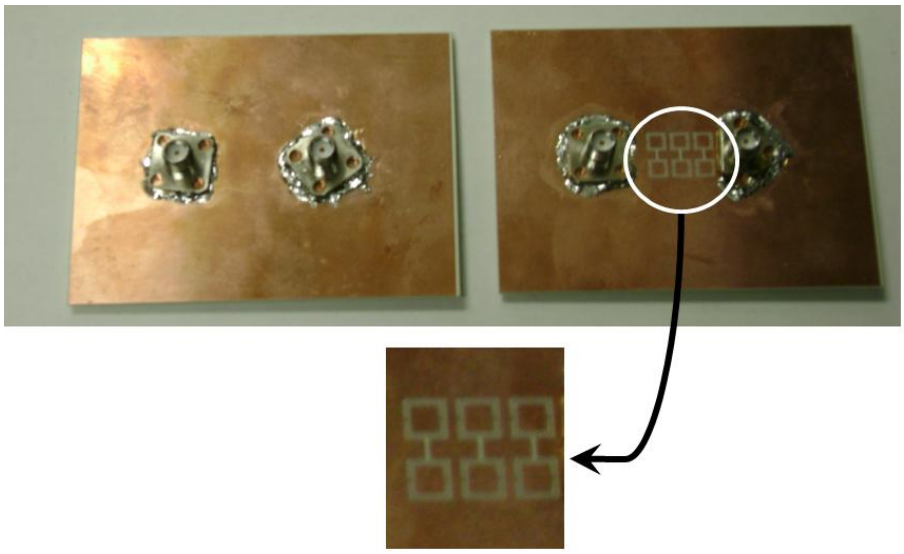

Figure 5.10: Bottom view of the fabricated low-profile antenna system with and without SCSRRs. The inset shows three SCSRRs etched in the ground plane.

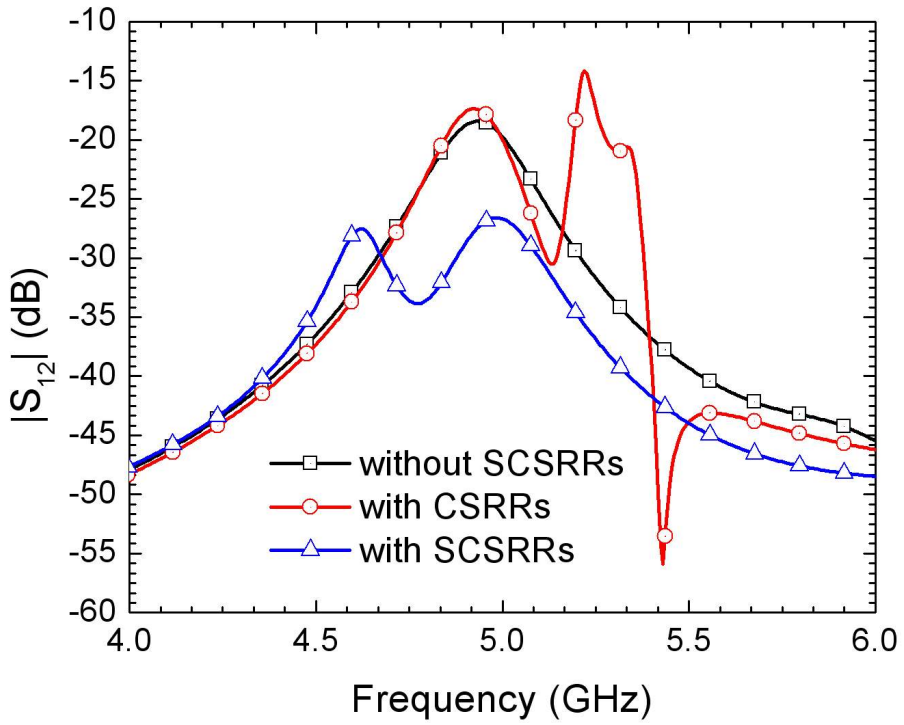

Figure 5.11: Simulated mutual coupling comparison for the two patch antennas without SCSRRs (solid ground plane), with SCSRRs, and with CSRRs.

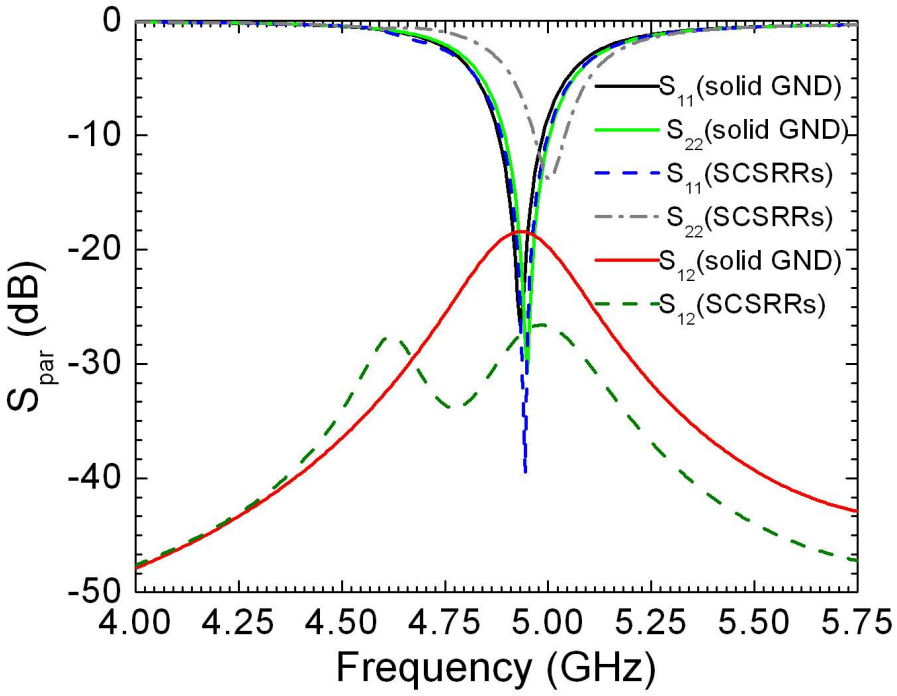

Figure 5.12: Simulated scattering parameters for the two patch antennas with and without the SCSRRs.

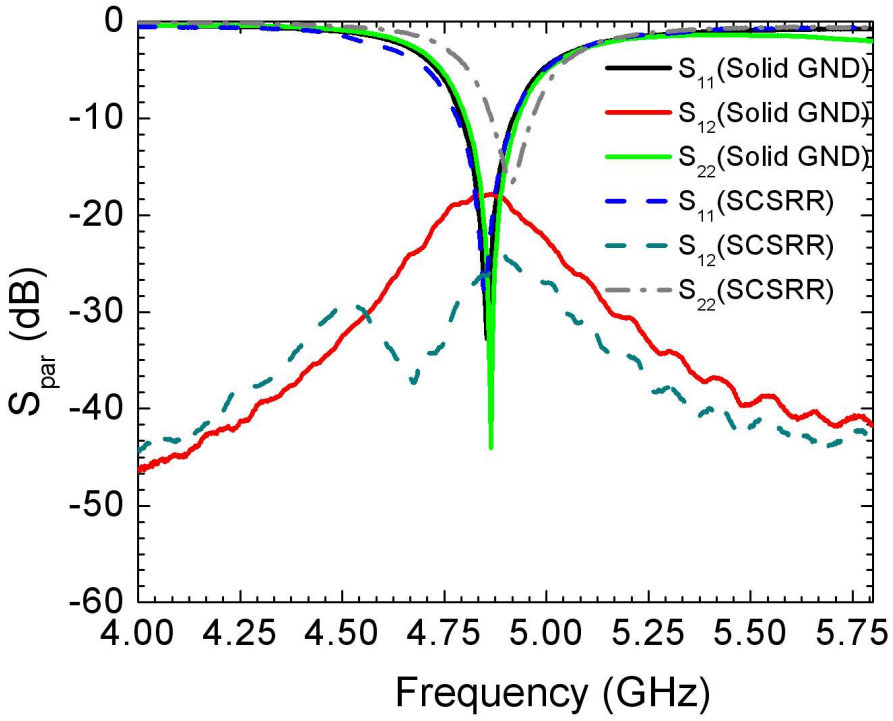

Figure 5.13: Measured scattering parameters for the two patch antennas with and without the SCSRRs.

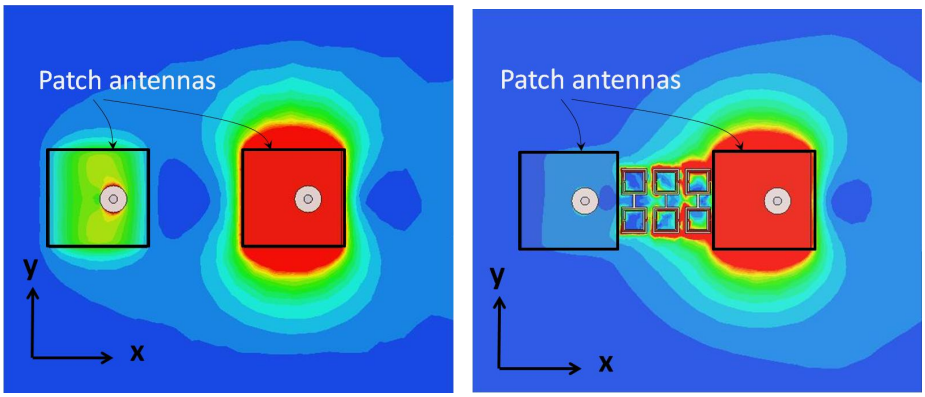

(a) (b)

Figure 5.14: Simulation results for the surface current distribution plotted in the finite ground plane for (a) the solid ground (no SCSRRs resonators), and (b) the SCSRRs case.

5.4.2 Current and field distributions

Since the substrate is very thin ($h/\lambda_0 \simeq 0.02$), surface wave modes are not the dominant source of coupling here as shown in Fig. B.2 in Appendix B). The TM_0 surface wave is the first mode that can propagate and has no cut-off frequency. However, it is not of significant effect for the substrate thickness considered in this work. In fact, the dominant coupling mechanism is a space-wave with vertical electric field component above the ground plane. The mitigation of the space-wave by virtue of the band-gap filtering is clearly observed in Fig. 5.14(a), in which the distribution of surface currents on the ground plane is plotted when one antenna is excited while the other antenna is terminated with a 50Ω impedance. Without the SCSRRS, high concentration of the surface currents is seen in the loaded antenna. Fig. 5.15 shows vertical electric field distribution (space-wave) for the patch antennas with and without SCSRRs. It can be seen from Fig. 5.15(a) that the SCSRRs resulted in suppressing the normal electric field component that radiates into space, and strongly couples to the nearby patch antenna element for the case of no SCSRRs as shown in Fig. 5.15(b). The inclusion of SCSRR resulted in only a slight shift in the resonant frequency of the patches as depicted in the reflection coefficient shown in Fig. 5.13.

5.4.3 Far-field

The antenna gain patterns were computed by exciting one of the antennas and loading the other with a 50Ω impedance. The E- and H-plane patterns, depicted in Figs. 5.16(a)-5.16(b), respectively, do not show any significant difference between the main lobes patterns. A slight back lobe radiation occurred due to the perforations in the SCSRRs,

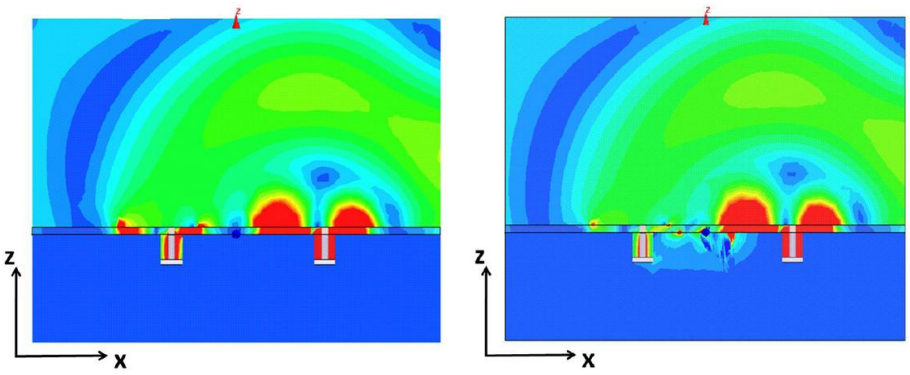

(a) (b)

Figure 5.15: Simulation results for the space-wave coupling plotted along the transverse plane (a) the solid ground (no SCSRRs resonators), and (b) the SCSRRs case.

however, this can be compensated for using a thin backing layer. The measured peak gain is shown in Fig. 5.17 which was measured in an Anechoic chamber for the two antenna systems with and without the SCSRRs inclusions. Furthermore, the antenna's efficiency does not show any notable change at the operating frequency, as can be seen from Fig. 5.18.

5.5 Conclusion

In this chapter, new sub-wavelength slotted complementary split-ring resonator (SCSRR) was developed and used to reduce the mutual coupling between low-profile patch antennas. The properties of the SCSRR were studied using dispersion analysis and retrieved constitutive parameters of an effective homogenized SCSRR media. The SCSRRs were able to reduce the mutual coupling between two microstrip patch antennas spaced by a quarter free-space wavelength. The reduction was possible because of the ability of the SCSRRs to efficiently suppress the electric fields normal to the ground plane, which in turn reduced the surface currents in the terminated antenna element. A 10-dB reduction in the mutual coupling was achieved when three SCSRR cells were placed in the ground plane between the two patches. Furthermore, unlike EBG and SRR based coupling reduction techniques, no additional metallic structures were embedded inside the substrate.

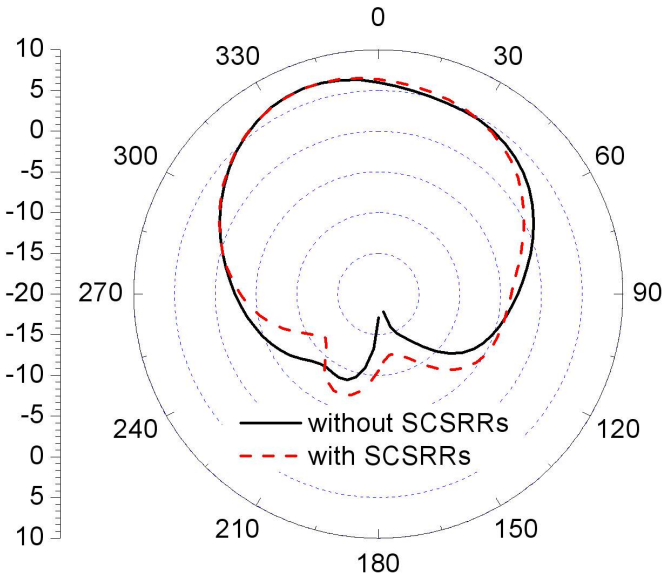

(a)

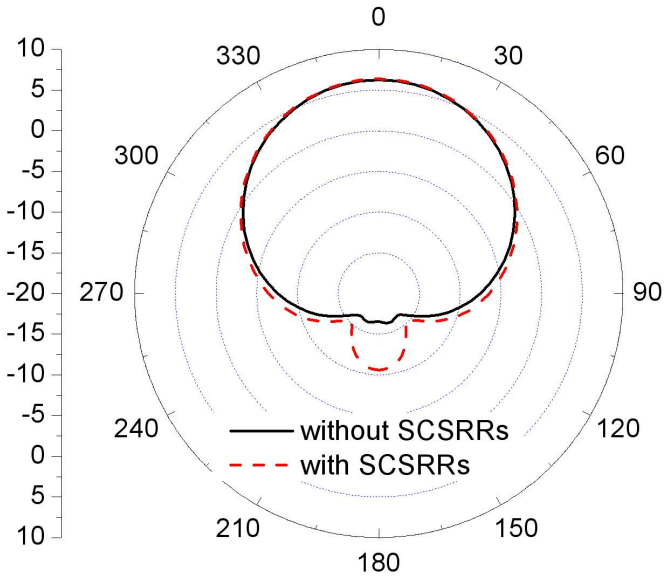

(b)

Figure 5.16: Simulation results for the far-field gain patterns for the two patches with and without SCSRRs resonators at 4.97 GHz: (a) E-plane; (b) H-plane.

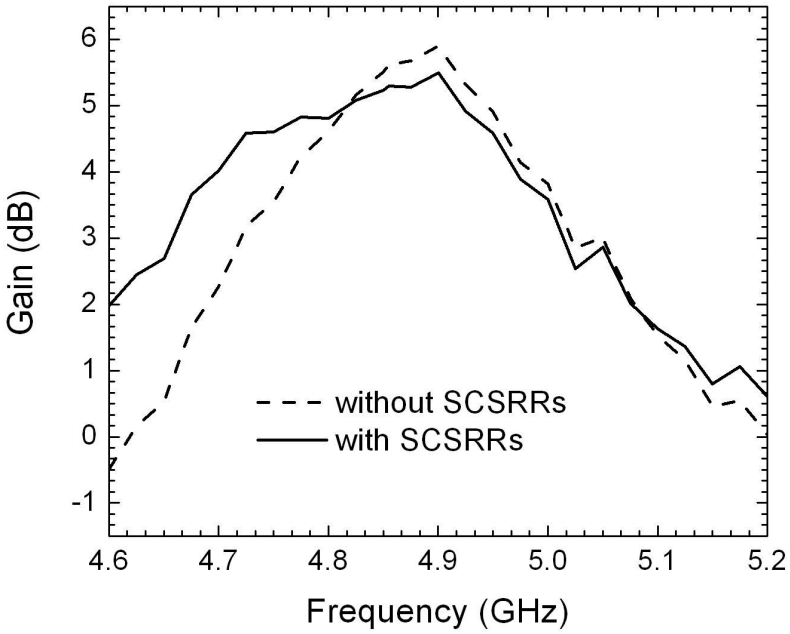

Figure 5.17: Measured peak gain for the two antenna systems with and without SCSRRs.

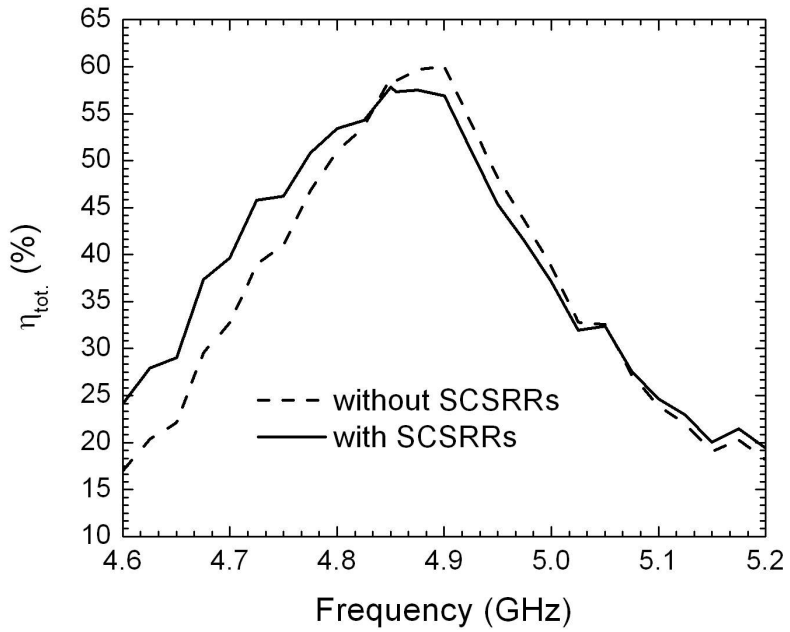

Figure 5.18: Measured total efficiency for the two antenna systems with and without SCSRRs.

Chapter 6

Applications of Complementary Resonators for Noise Mitigation in High-Speed Printed Circuit Boards

6.1 Introduction

It was discussed in chapter 2 that simultaneous switching noise (SSN) appears as unwanted voltage fluctuations on the power bus of the printed circuit board (PCB), due to the excited resonance modes between the power/ground plane pair. Those voltage fluctuations cause significant signal integrity (SI) problems and electromagnetic interference (EMI) issues for the high-speed PCB. Therefore the elimination of the power plane resonances is essential. In this chapter, a novel effective technique for mitigating SSN propagation in PCBs is presented. The proposed concept is based on etching complementary split-ring resonators (CSRRs) on only one metallic layer of the printed circuit board. By such topology, the electric field between the power plane layers can be suppressed. It will be shown in this chapter that by concentrically cascading CSRRs, an ultra-wide band suppression of simultaneous switching noise (SSN) from sub-GHz to 12 GHz is achieved. A PCB prototype of the proposed concept was simulated, fabricated and tested. Good agreement is achieved between simulation and measurement.

The organization of this chapter is as follows: section 6.2 addresses the mechanism of operation of CSRRs in power planes environment. Numerical full-wave results are presented and validated with measurements. Possible EMI leakage from the perforated

power planes is investigated both numerically and experimentally in section 6.3. Section 6.4 elaborates on the performance of the novel power planes with CSRRs through signal integrity analysis. Finally, a brief summary based on the findings is presented in Section 6.5.

6.2 SSN Mitigation Using Complementary Split-Ring Resonators (CSRRs)

6.2.1 Model description

As was discussed in Chapter 3, artificial magnetic materials, like split-ring resonators (SRRs) amongst others, resonate when driven by an external magnetic flux with a component normal to the plane of the loops of the SRR. This resonance behavior is caused by a time-varying magnetic field **H** incident upon the SRR plane. Depending on the resonant properties of the SRRs, the induced magnetic field within the artificial rings may oppose or enhance the external incident field. This in turn gives an effective inductance which when balanced with the capacitance between the rings, gives rise to magnetic resonances. Recall, based on duality and Babinet's principle [127], *complementary* SRRs (CSRR) are expected to respond to an applied electric field parallel to the CSRRs axis (since the PCB has a finite thickness, the complementariness is less than ideal [129]). Thus, CSRRs possess an electrical resonance (or electrical bandgap behavior) upon axial **E**-field excitation. Fig. 6.1 depicts a cross section of a split-ring resonator unit cell with its complementary counterpart.

Within the parallel plate guiding system of the PCB, and considering the energy-dominant modes, the electric field is normal to the metal planes because of the very close proximity of the power planes to each other (i.e., power plane thickness $h << \lambda$ for the dominant modes). Thus, if a CSRR is etched on the power plane metal layer and is in the path of field propagation, it is expected to impede the propagation over the resonant frequencies of the CSRR. To achieve a wideband noise suppression, several CSRRs, which resonate at different frequencies, are designed to cover multiple bandgap regions. Since switching noise results in a wave that propagates radially between the metallic layers of the PCB, a natural placement of CSRRs would be in a concentric fashion which results in cascading the respective effective bandgaps. Fig. 6.2 shows four CSRRs cascaded concentrically.

The dimensions of the CSRRs resonators were initially characterized separately using a simple microstrip transmission line method as in [129] in order to obtain a quick esti-

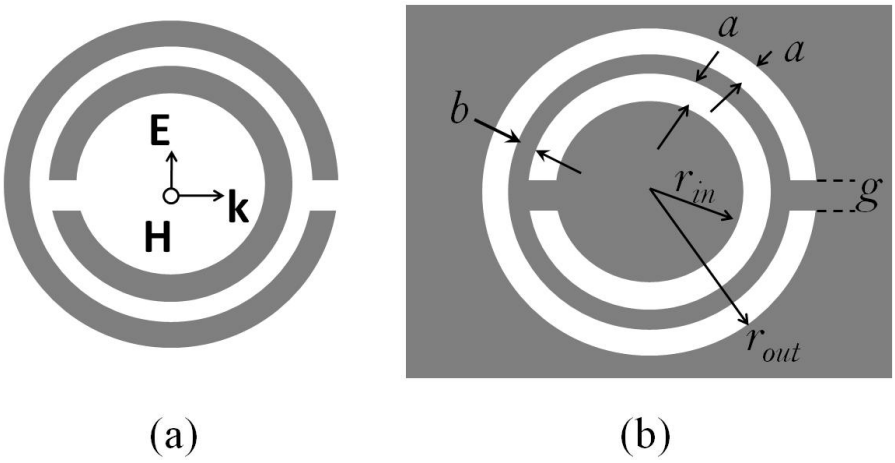

Figure 6.1: (a) Split-ring resonators (SRRs), and (b) its complementary screen (CSRRs). The gray shaded area represents metallization.

mate of the CSRRs frequency bandgaps. We emphasize here that although the physical behavior of power planes is different from the simple transmission line characterization used here, the dominant quasi-TEM mode insures the excitation of normal electric field component needed to excite the CSRR resonators. Fig. 6.3(a) shows the model used to characterize the CSRR resonators. The width of the microstrip line is designed to match a 50Ω impedance. The dielectric material is FR-4 with a thickness of $h = 1.54mm$. The radii of the designed CSRRs shown in Fig. 6.2 are $r_{in1} = 4.2mm$, $r_{in2} = 5.0mm$, $r_{in3} = 6.3mm$, $r_{in4} = 6.9mm$, $r_{in5} = 8.2mm$, $r_{in6} = 8.4mm$, and outer radius $r_{out} = 10.4mm$. Referring to Fig. 5.1, $a = b = g = 0.2mm$. Fig. 6.4 shows the simulation results for the transmission coefficient S_{12} for several CSRR unit cells, placed as shown in Fig. 6.3(a). The CSRR unit cells have several stopband regimes, that when cascaded concentrically, it is expected to widen the bandgap regions.

A case study is considered next. A source of switching noise was placed within the parallel plate PCB and concentrically surrounded by a set of four CSRR resonators as shown in Fig. 6.2. Fig. 6.5 depicts a photograph of the fabricated power plane board with CSRRs etched on one layer. As discussed in chapter 2, power plane comprises a minimum of two metallic layers: one for the supply voltage and another for the reference or ground (return current), where a dielectric substrate (usually FR-4) is sandwiched between the two layers. The power plane board is of size l =70mm x w =60mm and thickness h = 1.54mm. The FR-4 substrate parameters considered for the simulation are $\epsilon_r = 4.4$ and $tan\delta = 0.02$. Simulations were carried out using the full-wave solver HFSS and compared with measurements.

The transmission coefficient S_{12} was computed for an output port placed 4cm away

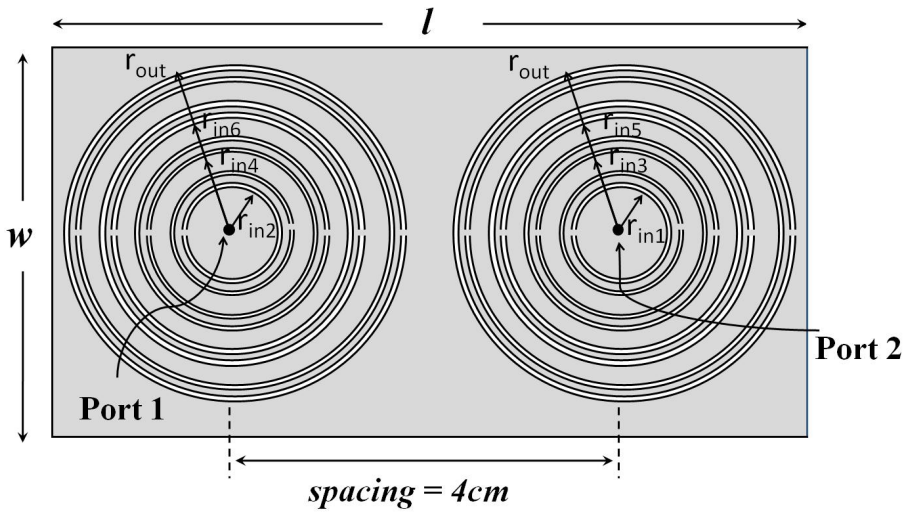

Figure 6.2: Schematic representation for the CSRRs etched on one metallic layer of the PCB. Note that schematic is not drawn to scale.

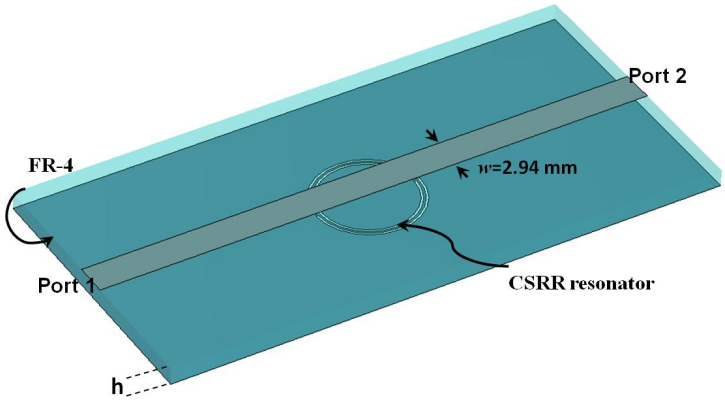

(a)

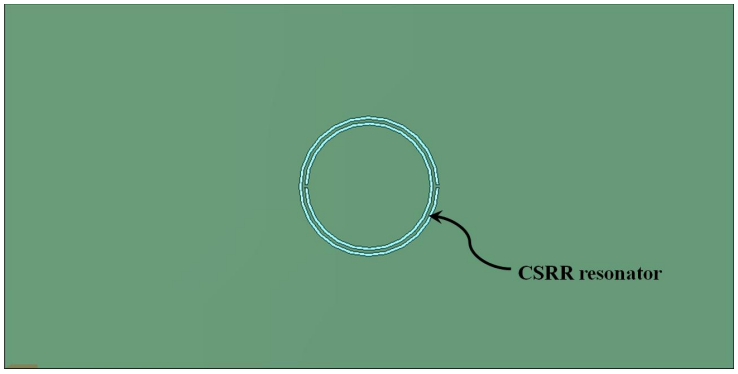

(b)

Figure 6.3: 3D view of the characterization model used to identify the bandgap regions of the CSRR resonators, (b) Bottom view showing the etched CSRR unit cell.

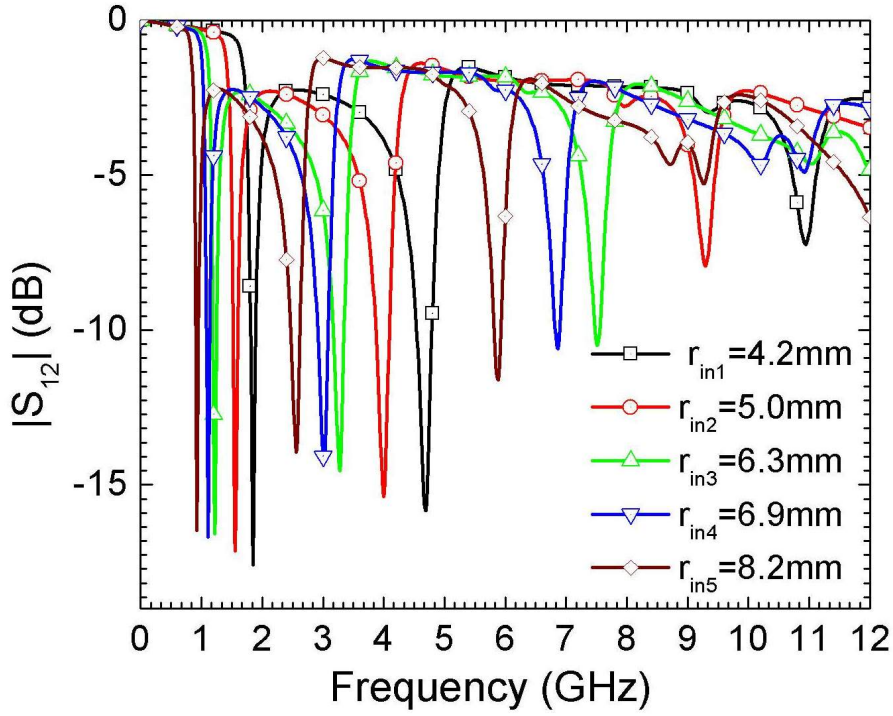

Figure 6.4: Simulated transmission coefficient, S_{12}, for the individual CSRR resonators.

from the source (see Fig. 6.2). The output port was also surrounded by a set of concentric CSRR resonators in order to add additional suppression. For comparison, a board with solid copper layers was also considered as the control case.

6.2.2 Experimental and Numerical Results

Fig. 6.6 shows the transmission coefficient S_{12} for the PCB with and without the CSRR resonators. An ultra-wide band suppression of switching noise is achieved covering the frequency band from sub-GHz to almost 12 GHz. The bandwidth criteria for noise suppression used here is for the magnitude of S_{12} to be less than -20 dB. Good agreement is observed between measurement and simulations. The slight shift seen from simulations is attributed to the uncertainties in the FR-4 board dispersion properties. The fast fluctuations in the transmission coefficient correspond to the resonances of the power planes that are excited due to the source of noise and finiteness of the power plane. Within the numerical simulations, the metallic layers of the power planes were modeled as perfect electric conductor with zero thickness, and an electric loss tanδ of 0.02 for the FR-4 laminate was considered over the entire range of frequencies considered here.

Fig. 6.7 depicts the simulation results for the transmission coefficient for the proposed structure with and without an RC dissipative wall placed around the edges of the board.

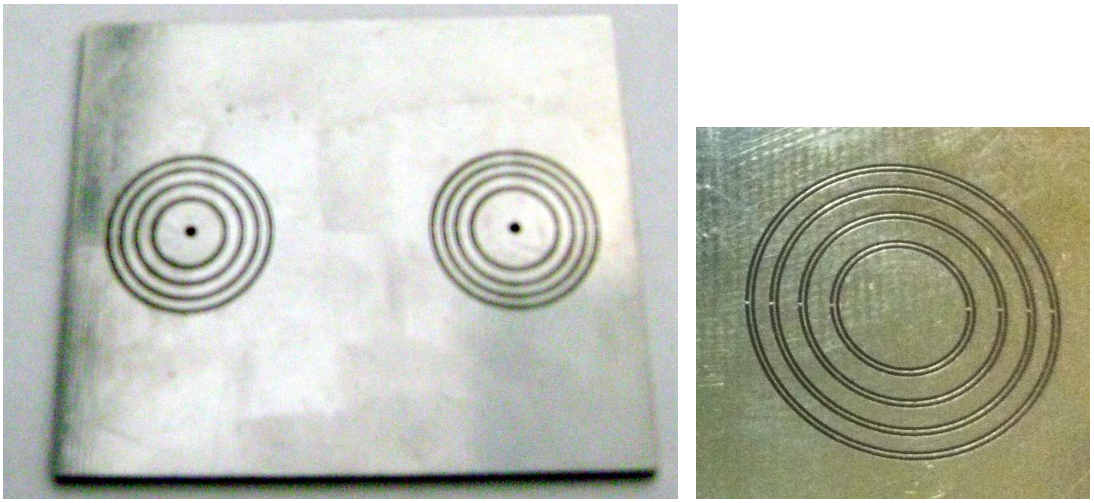

(a) (b)

Figure 6.5: (a) Photograph of the proposed power plane with CSRRs, (b) A close-up photo showing the cascaded CSRR rings.

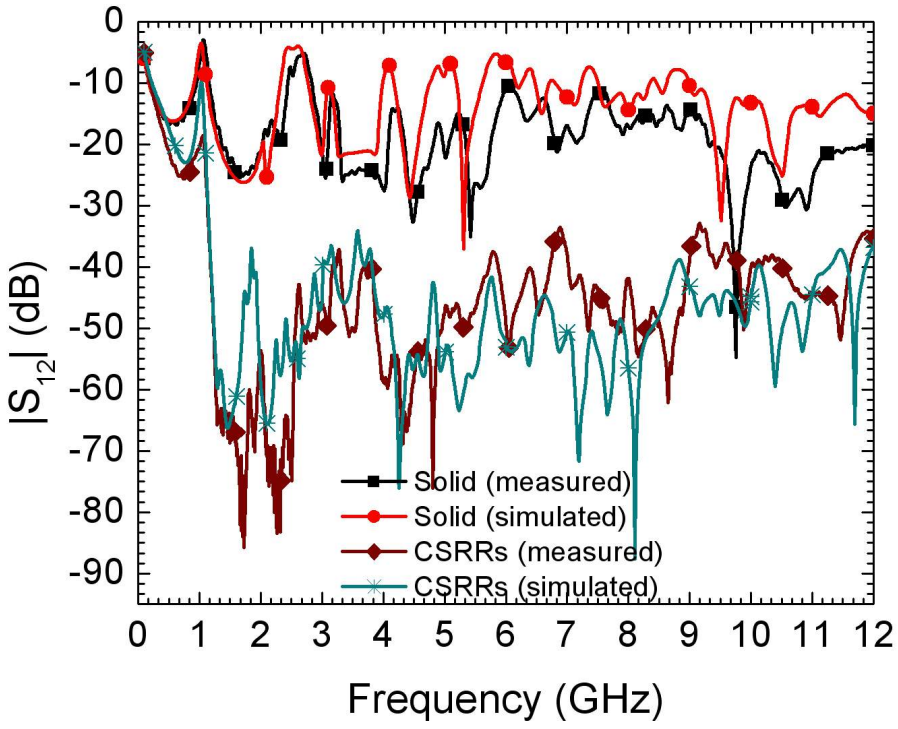

Figure 6.6: Simulated and measured transmission coefficient, S_{12}, for the PCB with and without CSRR resonators.

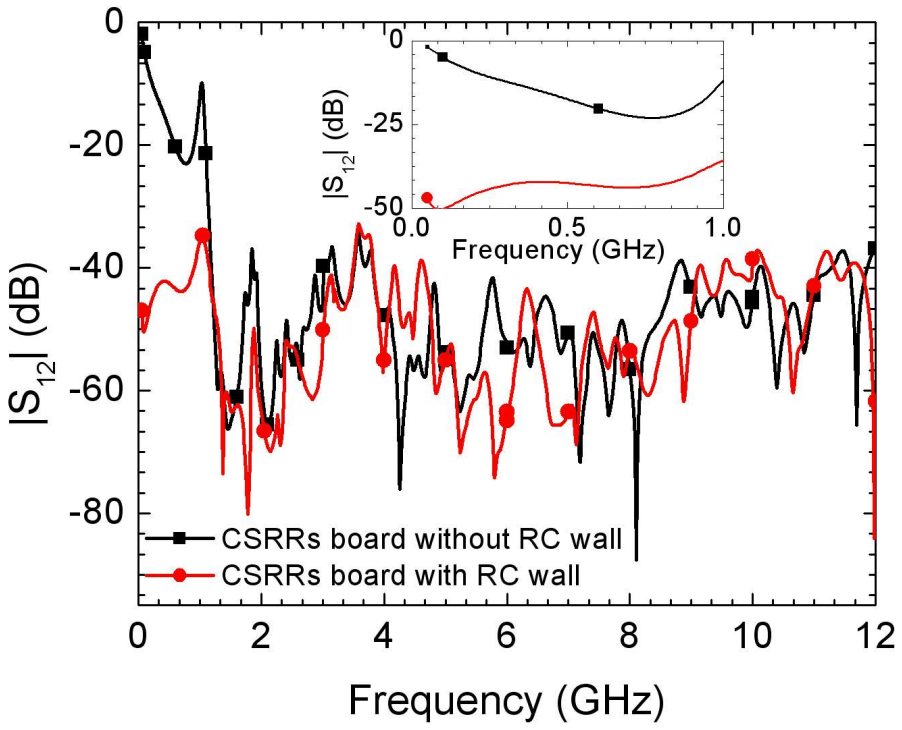

Figure 6.7: Simulated transmission coefficient, S_{12}, for the CSRRs PCB with and without the RC wall. The inset shows the transmission coefficient magnitude for both cases in the sub 1 GHz frequency band.

A total of 40 RC pairs were placed uniformly around the PCB with $R_w = 5.36\ \Omega$, $C_w = 1$ nF and $L_w = 0.5$ nH as implemented in [68] (note that the inductance value of 0.5 nH accounts for the effect of the leads of the capacitors as in [68] and references therein). The capacitors wall offers good switching noise mitigation capability at the lower frequencies as shown in the inset of Fig. 6.7, while the CSRRs show their effectiveness above 1 GHz.

6.3 EMI Radiation

6.3.1 Field leakage through the CSRRSs board

As discussed in Chapter 2, when multiple integrated circuits switch simultaneously, time-varying currents are generated and travel along the parallel-plate guiding structure. The traveling waves diffract once reaching the edges of the PCB board and radiate in a manner similar to patch antennas [12]. Moreover, part of the time-varying fields at the edge reflects back and forth, and introduces resonant modes within the power plane. The total lost power can be characterized by the quantity 1 - $|S_{11}|^2$ - $|S_{12}|^2$. This loss

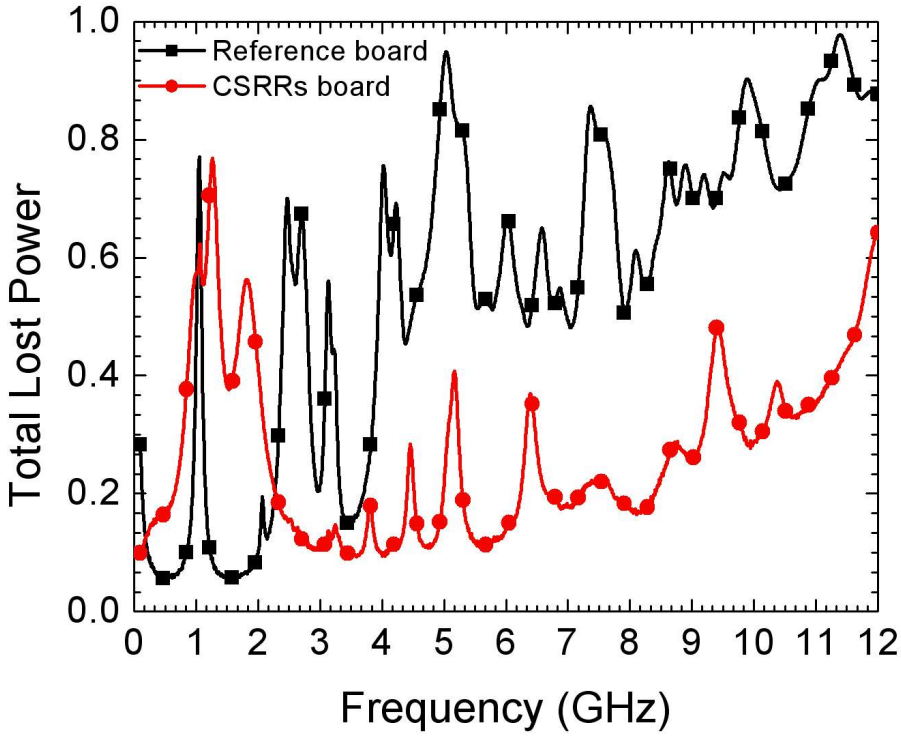

Figure 6.8: Total lost power from the reference power plane and proposed power plane with CSRRs obtained using the measured scattering parameters of the two power planes.

quantity is different from a lossless closed system, in which the sum of the reflection and transmission coefficients equals unity.

Fig. 6.8 shows the lost power obtained from the measured scattering parameters. High radiation can be seen from the reference power plane as compared to the CSRRs board. The radiated emissions leaking through the CSRRs board have been mitigated as a result of suppressing the power plane resonances. Note that the dielectric losses have not been included in Fig. 6.8. In fact, the dielectric losses were numerically computed by volume integration of the fields within the PCB board. Although not shown, the results show minimal dielectric loss power for the proposed board, which were below 0.1 watt in average. To give a qualitative idea of the encountered losses, the dielectric loss power for the proposed CSRRs board is computed for several frequencies. At 1 GHz, the dielectric losses for the reference board (no CSRRs) were 0.01 watt while it was 0.05 watt for the CSRRs board. The high radiation observed at 2 GHz in Fig. 6.8 is attributed to the encountered dielectric losses. Low losses were observed for the CSRRs board as compared to the solid board at frequencies above 2 GHz. At the upper frequency band (10 GHz-12 GHz), the dielectric losses for the CSRRs board were less than 0.021 watt, while high losses were encountered for the solid board reaching 0.16 watt.

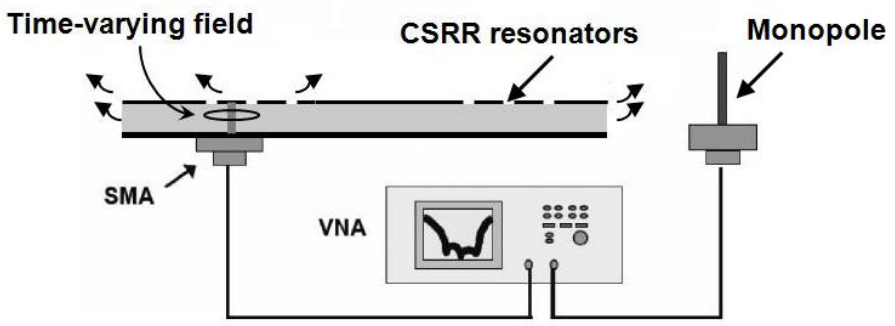

Figure 6.9: Experimental setup used to study near- and far-field EMI leakage from CSRRs board.

6.3.2 EMI radiation from CSRRs board

Fig. 6.9 shows the experimental set-up considered to study the electromagnetic leakage from the edges of the CSRRs board. A reference (solid) PCB board is used for comparison purposes. A quarter-wavelength monopole antenna, designed at 3 GHz, was used to capture the energy that leaks out from the edges of the reference and CSRRs boards. Figs. 6.10- 6.11 show the EMI radiation from the PCB boards measured in the near-field proximity of the board: $2cm$ and $5cm$, respectively. The far-field radiation from the CSRRs board is also measured at a distance of $10cm$ away from the PCB board edges as shown in Fig. 6.12. Around 3 GHz, more than 10 dB suppression of the near- and far-field EMI radiation is achieved for the CSRRs board. We note here that although significant suppression of EMI radiation was visible at 3 GHz, it is possible that electromagnetic leakage, due to the source of noise and perforations in the PCB board may result at other frequencies as a consequence of radiation from the perforations in the cascaded CSRR rings. For example, the high field radiation observed at 9 GHz for the CSRRs board as compared to the solid board is a result of radiated emissions from the perforations in the board and possibly from the edges of the CSRRs board, which had been observed in literature [74],[130]. Another important issue to mention here is that EMI radiation from multilayer PCB boards due to any perforated bandgap structure needs to be carefully considered, otherwise such radiation can result in severe interference and coupling problems that degrades signal and power integrity of the multilayer PCB boards.

It is important to investigate the effects of the perforated CSRR rings in order to qualitatively estimate the amount of energy leakage from the perforated rings. For such purposes, a monopole probe, connected through an SMA connector to one port of Vector Network Analyzer (VNA), was used and placed on top of the CSRRs board. Another SMA connector was connected from a source of noise to the other port of the VNA, and

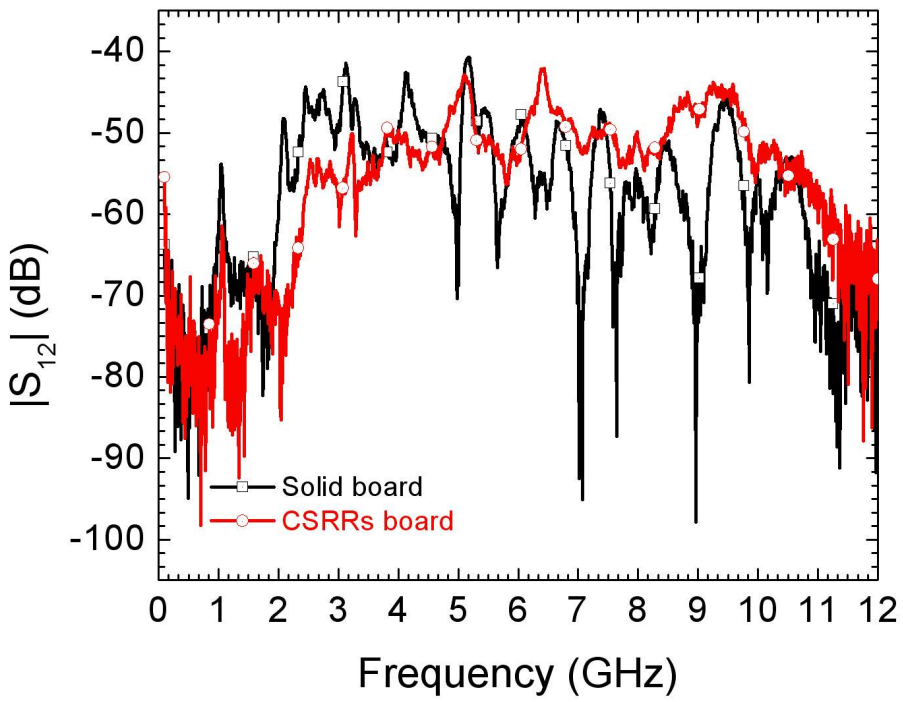

Figure 6.10: Measured field leakage from both solid and CSRR boards with monopole probe placed 2cm away from PCB edge.

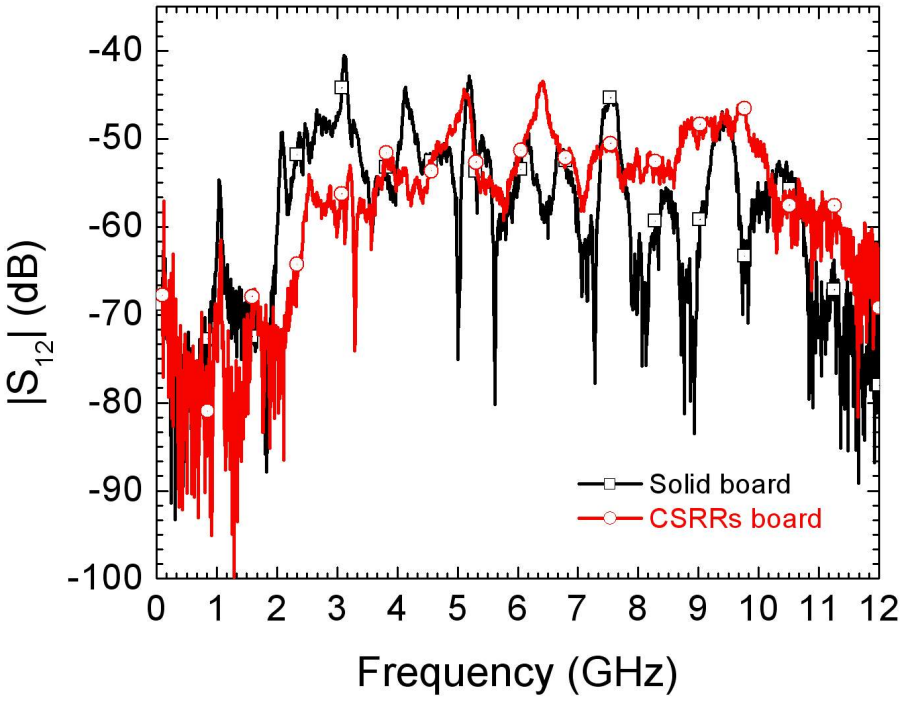

Figure 6.11: Measured field leakage from both solid and CSRR boards with monopole probe placed 5cm away from PCB edge.

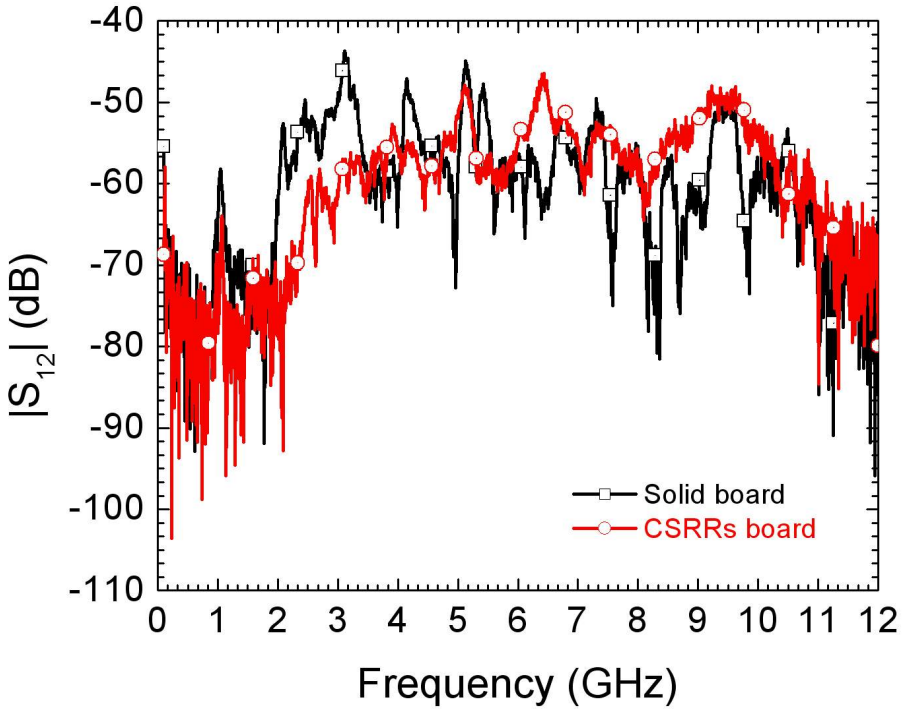

Figure 6.12: Measured field leakage from both solid and CSRR boards with monopole probe placed $10cm$ away from PCB edge.

S_{12} was used as a measure for the radiated power at various test points. Three different locations are considered along a test line: above the source of noise (feed location), above the center of the board and above the edge of the board. For convenience, same quarter-wavelength monopole probe used earlier is positioned $1cm$ above the PCB board. Fig. 6.13 depicts the experimental setup considered for this study. A solid power plane board is also considered for comparison purpose. Figs. 6.14-6.16 depict the S_{12} for the three different locations above the board. The measured results show that high field concentration accumulates around the source of noise, and gradually decreases away from the source of noise since the power plane resonances have been diminished as a result of using the cascaded CSRR rings. It is also important to mention that although wideband SSN mitigation was achieved here using the proposed perforated rings, radiation from such perforations may take place at some frequencies, and one have to avoid such frequency components if a switching device is allocated at one or any harmonic of those frequencies.

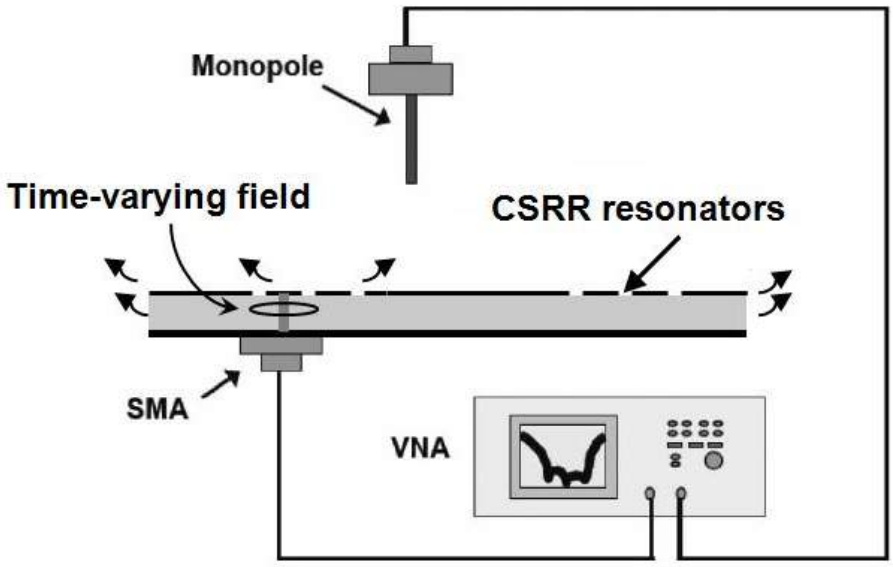

Figure 6.13: Experimental setup used to study the EMI radiation from top of CSRRs board.

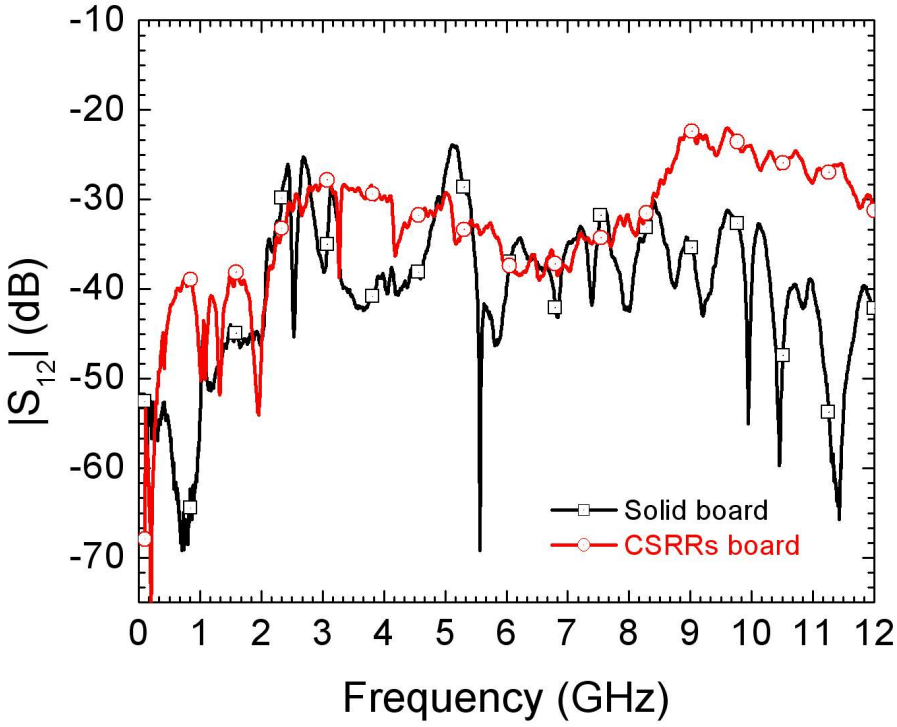

Figure 6.14: EMI radiation for both solid and CSRR boards with monopole probe placed on top of source of noise.

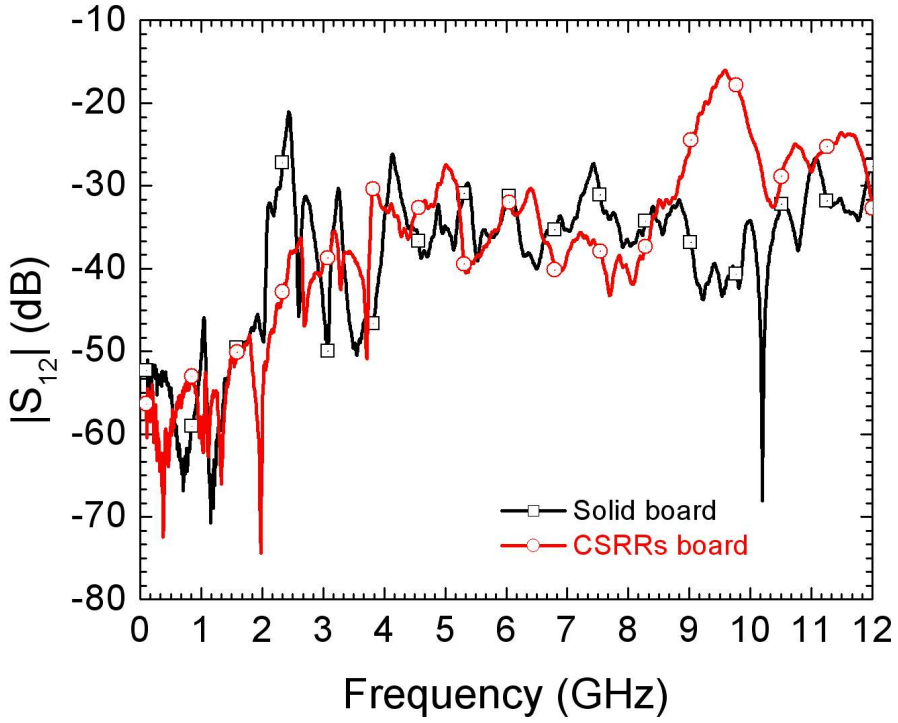

Figure 6.15: EMI radiation for both solid and CSRR boards with monopole probe placed on top and center of PCB.

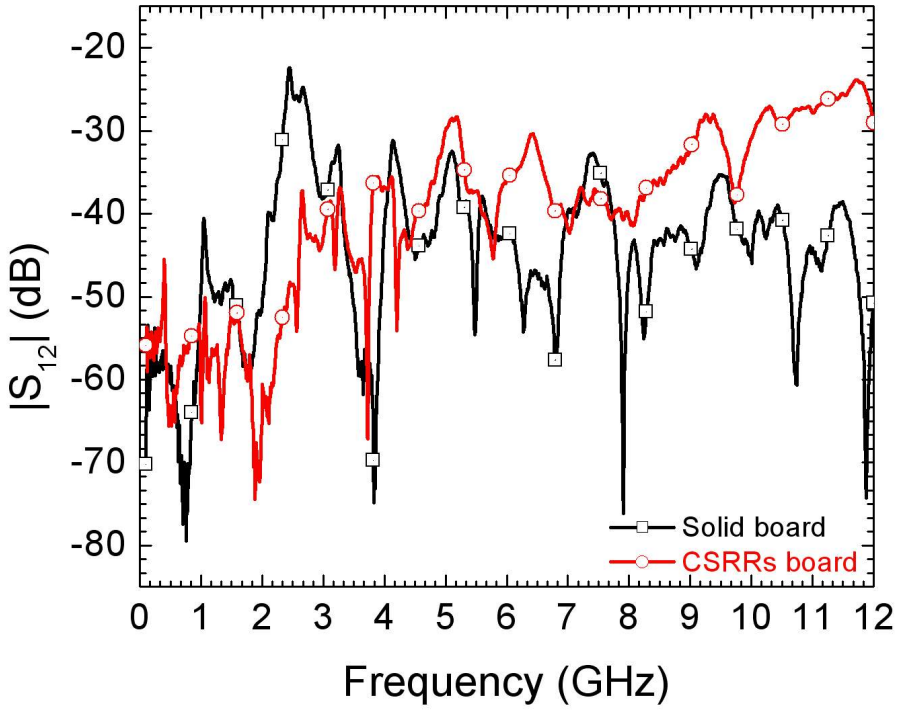

Figure 6.16: EMI radiation for both solid and CSRR boards with monopole probe placed on top along PCB edge.

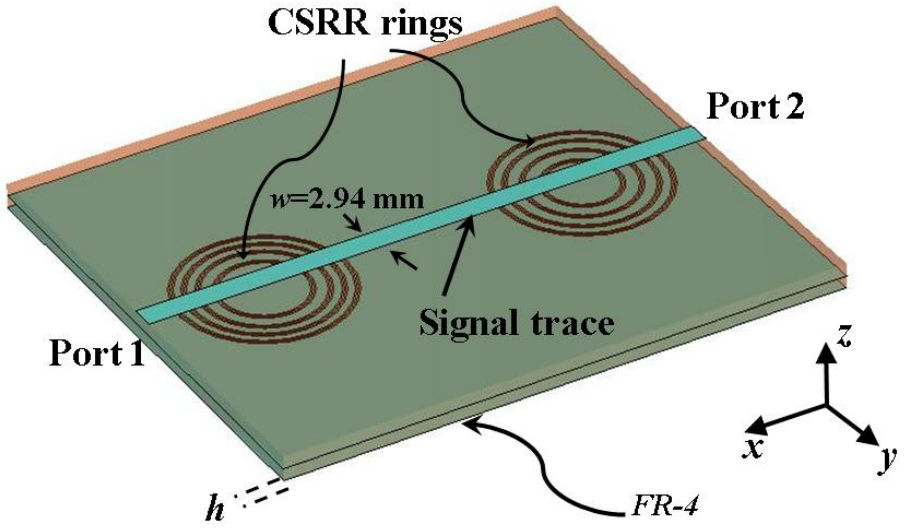

Figure 6.17: 3D model setup for the signal integrity performance. Note that gray area represents metallization.

6.4 Signal Integrity Analysis

In this section, the signal integrity of the proposed power plane with CSRRs is evaluated, and compared with a reference (solid) board. A pseudo-random bit sequence PRBS of $2^N - 1$ bits with N = 7 is launched at port 1 (see Fig. 6.17) through the signal trace, and the output signal is monitored at port 2. This output signal is then wrapped using CST MWS to generate the eye diagram. The transmitted bits sequence has a voltage swing of 1 volt, and is coded at 1 Gbps with a rise/fall time of 100 ps.

Three different cases are considered. Case I (see Fig. 6.18) considers signal integrity for a 3-layer PCB board, where the signal trace is positioned at the center of the third layer and referenced to either a solid board or the proposed CSRRs board. Case II investigates the signal integrity performance when signal trace is off-set by some distance from the center of the third layer and referenced to either solid or CSRRs board. Without loss of generality, a distance of $6.5mm$ is chosen. The third case evaluates the signal integrity for a 2-layer PCB board, where the signal layer is sandwiched between two metallic layers. The width $w = 2.94mm$ of the signal trace for cases I and II is designed to match the microstrip line (signal trace) to a 50 Ω impedance, whereas a trace width of $0.7mm$ is used to match the stripline (case III) to 50 Ω.

Figs. 6.19(a)- 6.19(b) show the generated eye diagrams for case I for the solid and CSRRs boards, respectively. Good eye opening is observed for the proposed CSRRs board. As the signal trace is moved off-the center of the CSRRs board (case II), the eye

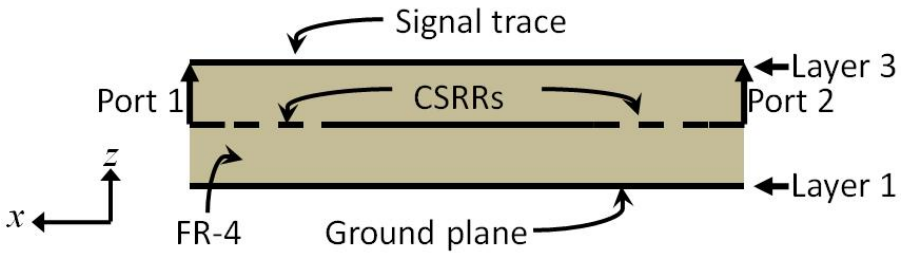

Figure 6.18: Side view for the model setup used to study the signal integrity performance of the proposed power plane with CSRRs.

Table 6.1: Summary of signal integrity performance for three different cases

	Case I	
	Solid board	CSRRs board
MEO (mV)	980	630
MEW (ns)	0.95	0.85
	Case II	
	Solid board	CSRRs board
MEO (mV)	980	700
MEW (ns)	0.93	0.90
	Case III	
	Solid board	CSRRs board
MEO (mV)	950	830
MEW (ns)	0.98	0.96

diagram is expected to improve as shown in Fig. 6.20. This is due to the fact that the signal trace couples less to the CSRR rings where perforations exist, and thus passing the signal more robustly than the signal in case I. The signal integrity performance for all three cases are tabulated as shown in Table. I. The placement of the signal trace within the power plane layers (case III) results in a wide eye opening in comparison to the previous two cases as shown in Fig. 6.21. This is attributed to the mitigated power plane resonances and the strong coupling between the signal trace and the metallic (ground) layer, where perforations are much away from the signal trace. Hence, the signal passes more robustly than the previous two cases.

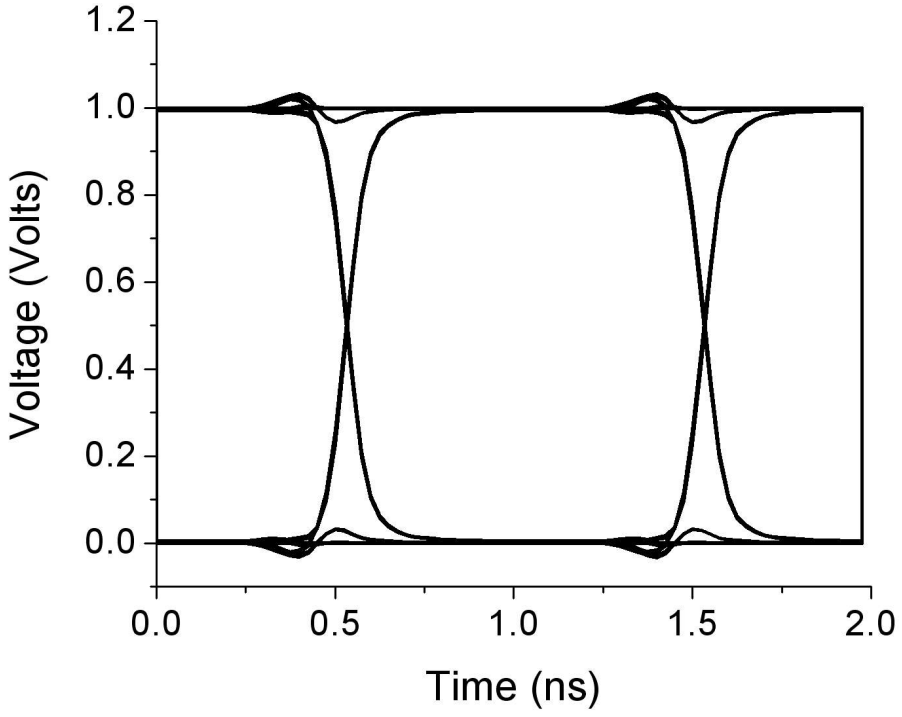

(a)

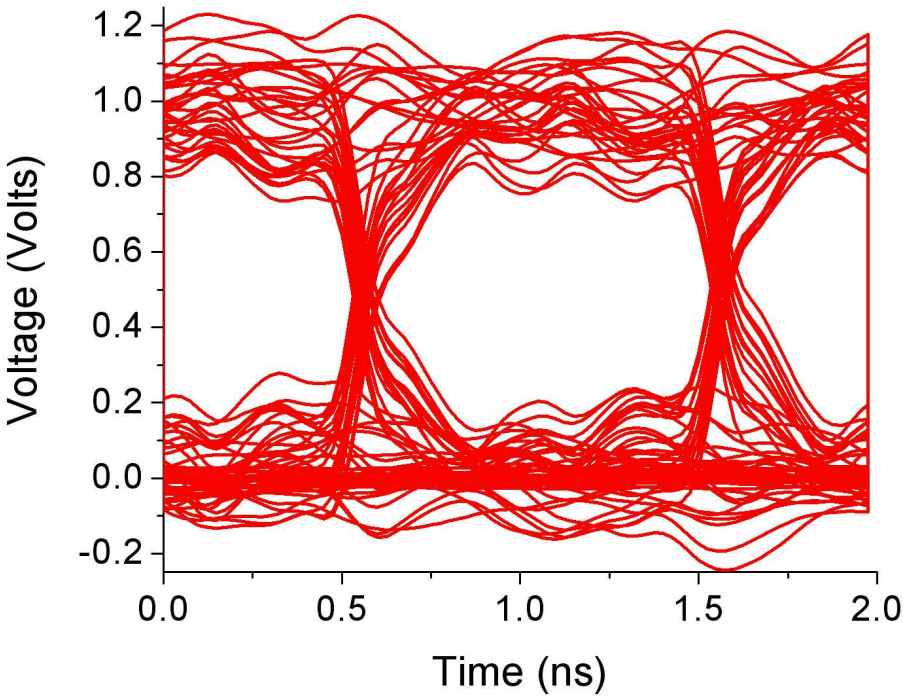

(b)

Figure 6.19: Eye diagrams generated for case I: signal trace placed on top (center) of (a) solid board; and (b) CSRRs board.

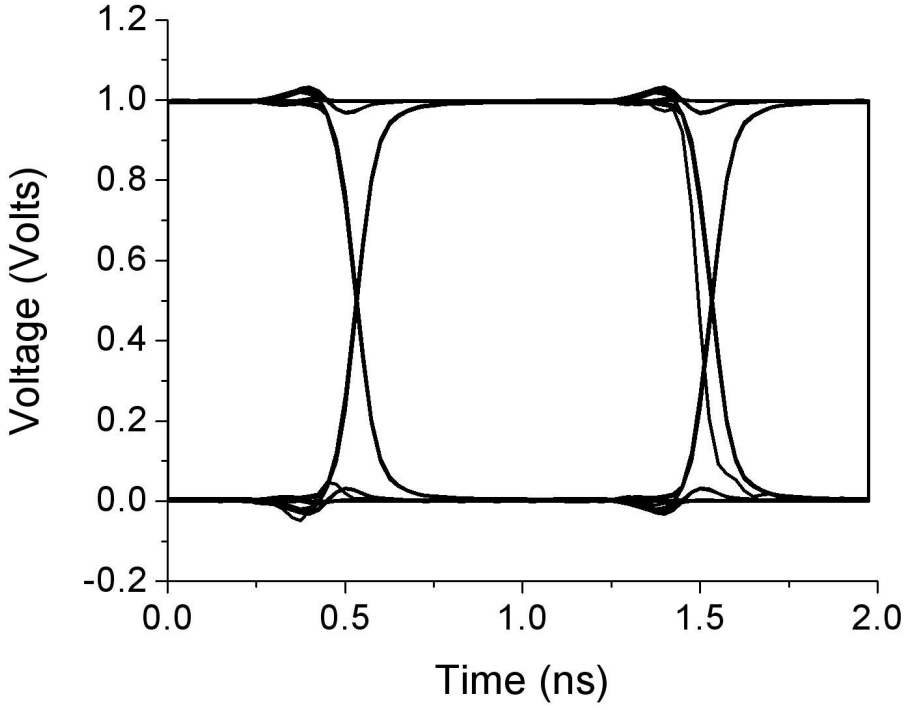

(a)

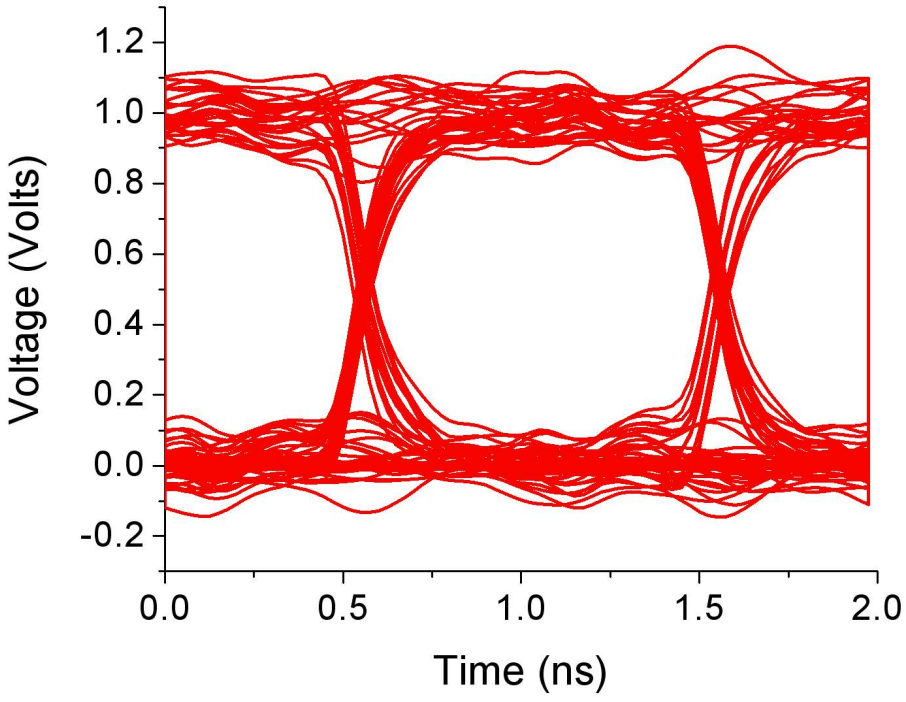

(b)

Figure 6.20: Eye diagrams generated for case II: signal trace placed on top (off-center) of (a) solid board; and (b) CSRRs board.

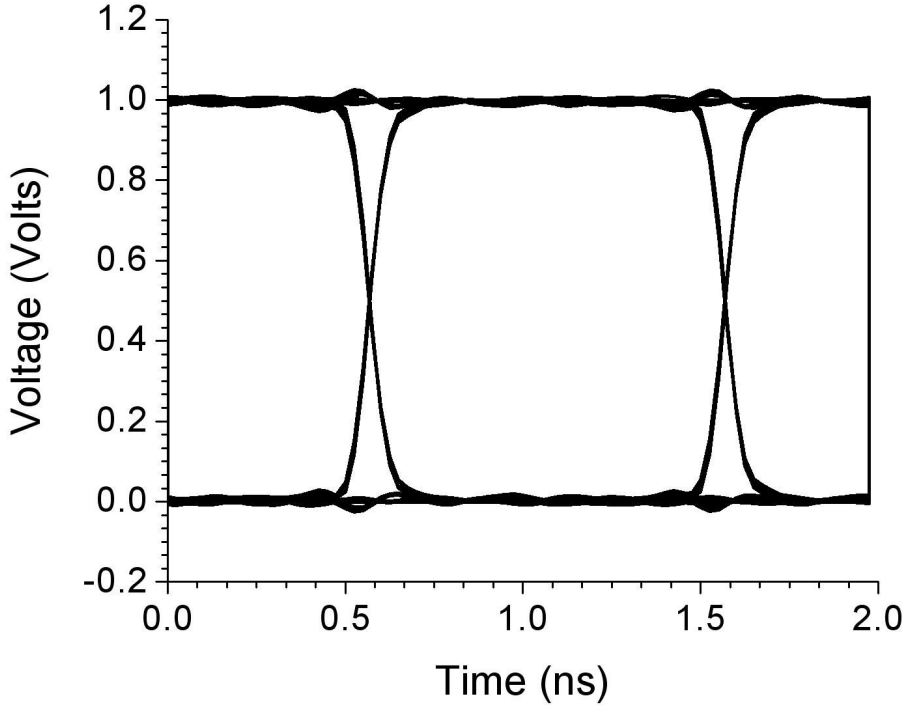

(a)

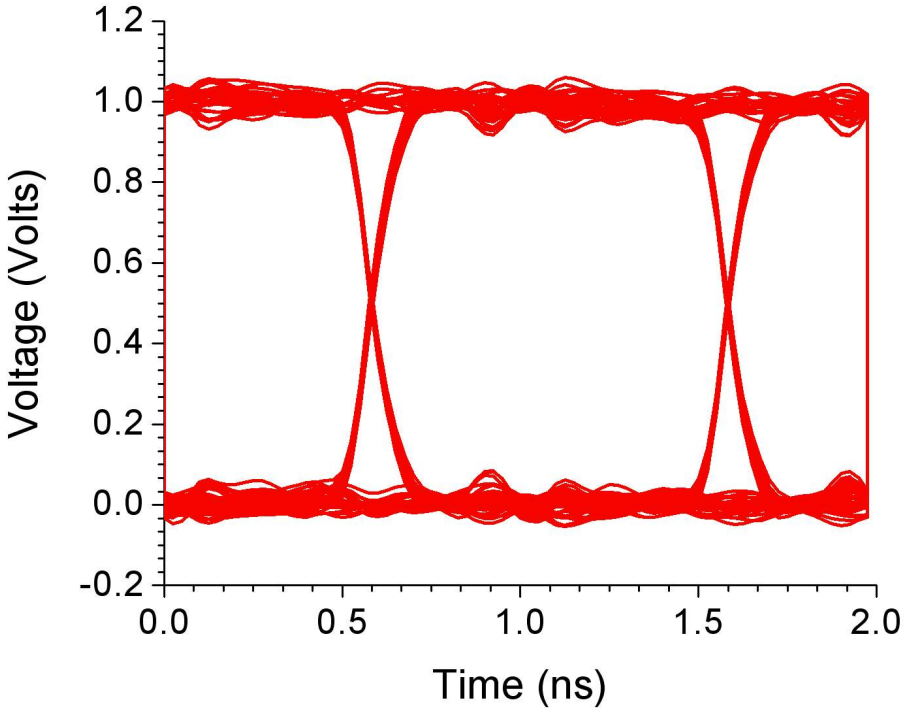

(b)

Figure 6.21: Eye diagrams generated for case III: signal trace placed (off-center) within the power plane of (a) solid board; and (b) CSRRs board.

6.5 Conclusion

In this chapter, complementary split ring resonators (CSRRs) were introduced for the first time to mitigate simultaneous switching noise from power planes for high-speed digital PCBs. The CSRRs are etched on only a single metallic layer of the power plane. It was shown that by concentrically cascading CSRRs around the noise and victim locations along with the placement of an RC wall around the board, ultra wideband switching noise mitigation below -20 dB can be achieved for a frequency range extending from 50 MHz to 12 GHz.

Furthermore, EMI radiation from the proposed power plane with CSRRs was experimentally evaluated. It was revealed that electromagnetic field leakage from the edges of the CSRRs board is mitigated using the proposed technique. EMI radiated emissions are also mitigated with the use of CSRRs, however, due to the perforated resonators, possible EMI radiation could take place from such perforations when placed around the source of noise. This radiation from the perforated rings has to be maintained as low as possible. Most importantly, signal integrity performance of the CSRRs board was studied and evaluated for several cases. It was found that good eye opening for the CSRRs board was maintained, which showed the robustness of the proposed technique.

Chapter 7

Noise Mitigation from Apertures and Enclosures

7.1 Introduction

Novel strategies to reduce radiated electromagnetic emissions from apertures placed in infinite metallic screens using EBG structures are presented. Such structures are inexpensive and result in a significant electromagnetic radiation suppression. The proposed technique comprises loading ribbon of EBG surfaces around the apertures' opening. Numerical full-wave simulations using CST MWS are presented to demonstrate the effectiveness of the proposed technique.

This chapter is organized as follows. Section 7.2 addresses the sources of electromagnetic radiation from apertures and enclosures. In section 7.3, design methodology of EBG structures to mitigate electromagnetic radiation from apertures is outlined. In section 7.4, the proposed aperture geometry with ribbon of EBGs is presented. Numerical results of both near- and far-field radiation through apertures are discussed in section 7.5. Section 7.6 provides a case study from real-world environment to quantify the amount of field leakage from enclosures with apertures. Finally, Section 7.7 concludes the chapter with a brief summary of the findings.

7.2 Radiation from apertures

Consider an arbitrary conducting sheet with an opening (aperture). The electromagnetic field solution to this classical radiation problem will mainly depend on the size of the

aperture. When both sides (length and width) of the aperture are much larger than the free-space wavelength, λ_0, of an incident time-harmonic field, the geometrical theory of optics can be used to solve this problem. On the other hand, when both dimensions of the aperture are much smaller than λ_0, Bethe's theory [80] can be applied to predict the radiation from such small apertures. In this work, the main focus is on what causes radiation from apertures with dimensions such that one side of an aperture is comparable to the operating wavelength, whereas the other side is much smaller than the wavelength.

Assume an electromagnetic transient wave impinging upon an aperture from one side. An important question to ask is what causes radiation from the aperture? The answer to this is summarized qualitatively as below. Part of this transient pulse is expected to go directly through the aperture (the high frequency components). After the initial part of the transient passes through the aperture, some energy starts traveling within the aperture along the directions of the longer dimension. At this stage, the aperture behaves as a driving source (see Fig. 7.1), due to the existence of surface current at its proximity. In Fig. 7.1, an aperture placed in an infinite metallic screen is shown. The size of the aperture, $20mm$ x $2mm$, corresponds to the maximum enhanced radiation of the aperture at a resonance frequency of 7.1 GHz, as shown in Fig. 7.2. The oscillation of the current back and forth along the edges of the longer dimension of the aperture gives rise to what is known as *aperture's resonance*. This resonance phenomenon can be visualized as shown in Figs. 7.1(a)-(c), where three different snapshots are shown for the surface current distribution at the external surface of an infinitely large conducting screen with a single aperture of dimensions $20mm$ x $2mm$. The aperture at its resonance shows significant current that accumulates along the aperture's edges and on the screen itself. This current then gives rise to radiation. In Figs. 7.1(d)-(f), snapshots of the surface current distribution are plotted at the external surface of the conductor surrounding the aperture at a non-resonant frequency; here a frequency of 4.5 GHz is chosen. For the non-resonant frequency, low electromagnetic radiation from the aperture takes place which corresponds to the low current levels surrounding the aperture in comparison to the case of the resonant aperture in Fig. 7.1(c).

Fig. 7.3 shows the E- and H-fields at the aperture's resonance frequency. These snapshots depict a standing-wave pattern behavior of the field at the aperture's opening; a behavior that resembles transmission-line type propagation. One can observe the field strength and standing wave pattern along the aperture's opening, where the H-field and E-field have a maximum and minimum, respectively at the edges of the aperture (see Fig. 7.3(a)).

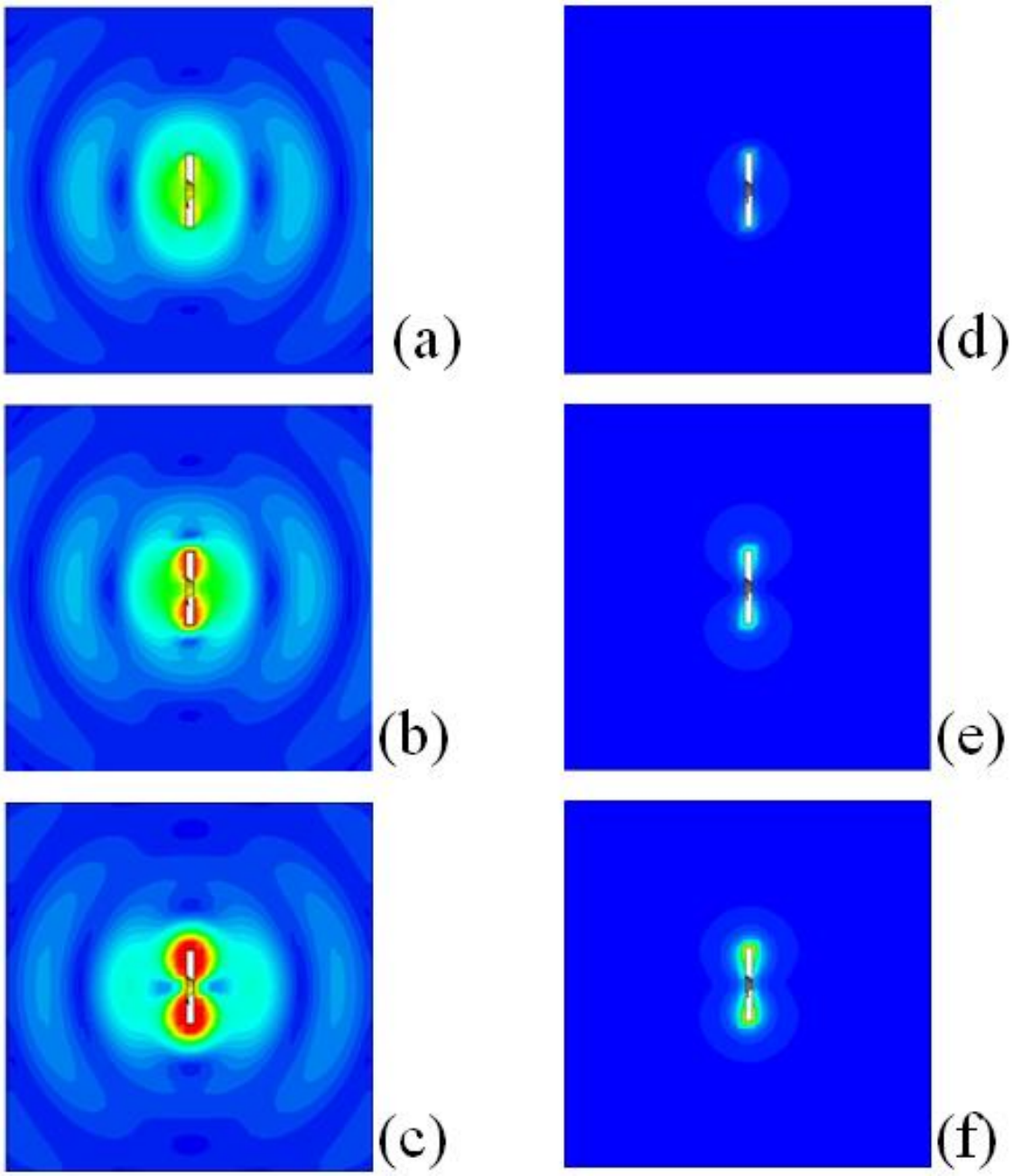

Figure 7.1: Simulation results for the surface current distribution at the external surface of the unloaded metallic screen: with aperture at its enhanced radiation (a, b, c); and non-radiating aperture case (d, e, f).

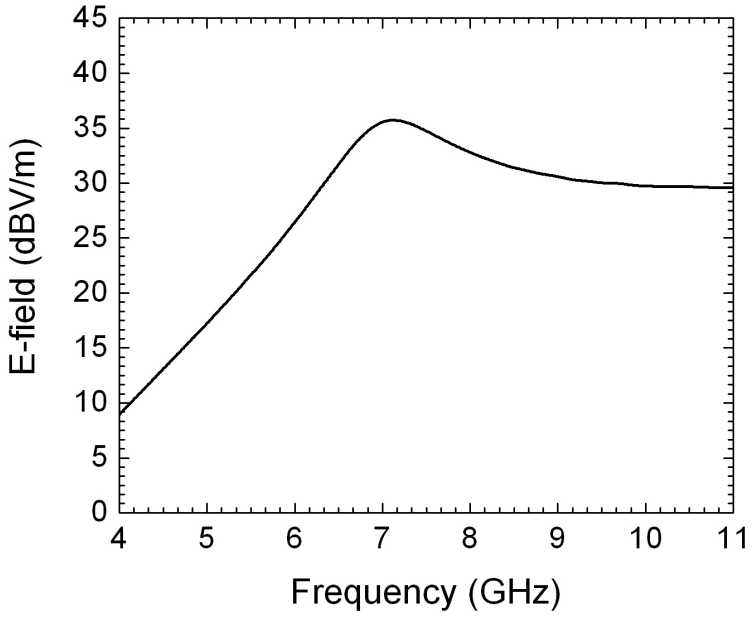

Figure 7.2: Simulation result for the electric field strength captured in the near-field of the aperture.

7.3 Design methodology of EBGs for EMI mitigation through apertures

As discussed in Chapter 3, EBG structures operating in the microwave regime are periodic patterns that are created by metallic inclusions etched on dielectric materials. The major characteristic and unique feature of EBG structures is the exhibition of a frequency band structure with stopbands. At frequencies within the stopband, surface currents propagation is inhibited. Without loss of generality, the mushroom-like EBGs are considered in this work, represented by the schematic shown in Fig. 3.1 in Chapter 3. These structures are characterized by periodic metallic patches connected to a common ground plane by plated through holes (vias).

The filtering mechanism of the EBG structure is demonstrated here through the k-β dispersion analysis to predict the bandgap zone of the EBG structure. A unit-cell with periodic boundary conditions was simulated using the eigen-mode solver of the commercial software CST Microwave Studio (MWS) to identify the bandgap zone of the EBG structure. The design criteria for EBG structures to mitigate aperture's radiation is to construct a bandgap that falls within the aperture's resonance frequency so that the surface current propagation is inhibited within the metallic screen.

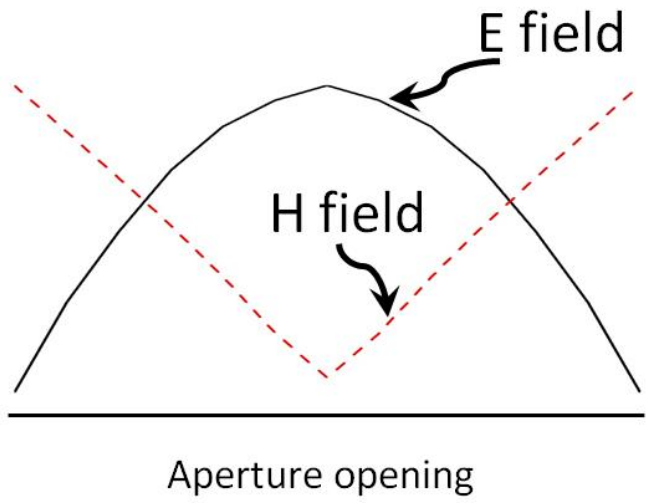

(a)

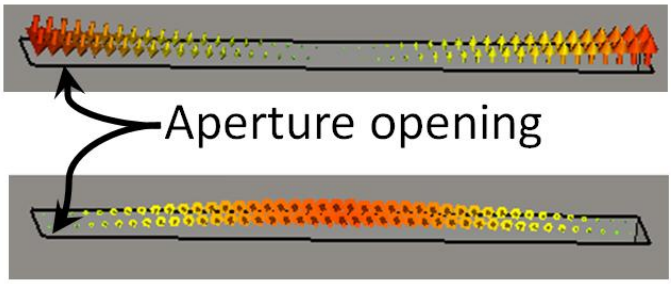

(b)

Figure 7.3: Simulation results for (a) E and H field profiles along the aperture, (b) E and H fields distribution plotted along the aperture's opening showing the standing wave behavior at resonance.

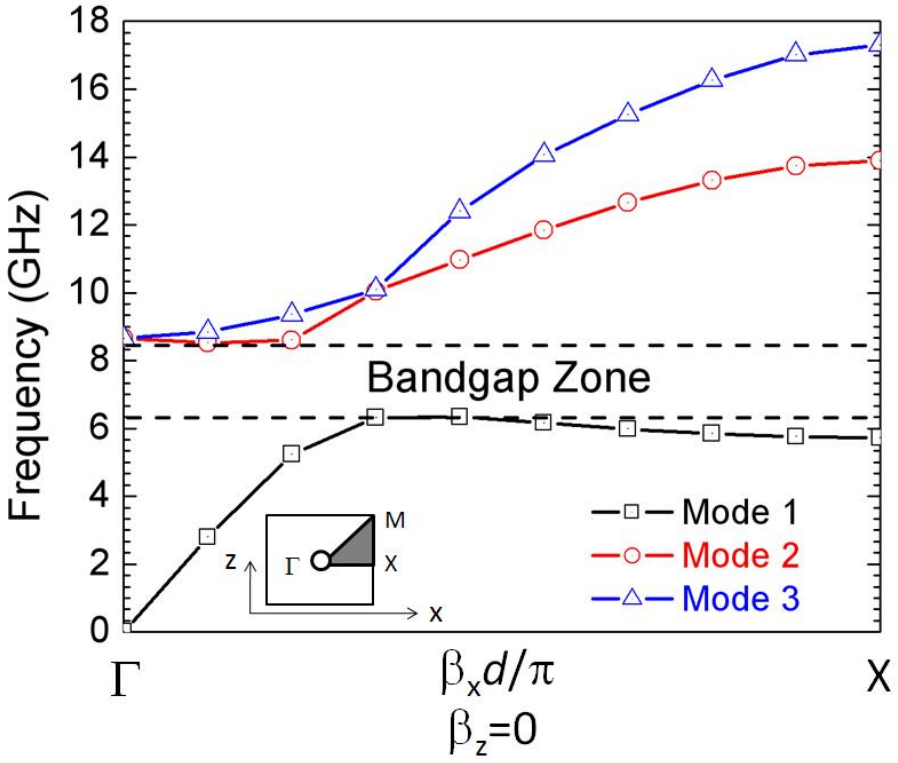

Figure 7.4: Dispersion diagram for an EBG unit-cell with periodic boundary conditions. The inset depicts the irreducible Brillouin zone directions.

The initial parameters of the EBG structure were designed as follows. First, the center frequency of the bandstop region of the EBG structure was chosen as the aperture's resonance frequency of 7.1 GHz. Moreover, the EBG host material (dielectric substrate) was also selected a priori based on availability of materials. Second, the inductance L was calculated using equation (3.4), from which the capacitance C was obtained from the LC product of equation (3.2). The calculated circuit parameters are $L = 1.88$ nH and $C = 0.26$ pF.

Relations (3.4) and (3.5) provide relatively good approximations for the initial design. Consequently, the parameters of the EBG unit cell were fine tuned to cover the resonance frequency of the aperture within the EBG bandgap regime using CST MWS. An eigen-mode analysis was conducted to characterize the bandgap zone of the EBG structure. The parameters of the optimized EBG structure are: $a = 5.2mm$, $g = 0.2mm$, with unit cell periodicity a+g $= 5.4mm$, and substrate with $\epsilon_r = 2.65$ and thickness $h = 1.5mm$. Plated-through vias with diameter of $d = 0.5mm$ are used. Fig. 7.4 shows the dispersion diagram for the Γ-X phase direction. The EBG bandgap zone of the final tuned design covers the frequency range from 6 GHz to 8 GHz.

7.4 The Aperture geometry with EBGs

Fig. 7.5(a) shows the geometry of the aperture measuring $20mm$ x $2mm$ placed in an infinite metallic screen. The screen thickness is $2mm$ (in the y-direction, see Fig. 7.5(a)). A ribbon of EBG surface measuring $36.6mm$ x $52.2mm$, in the x and z directions respectively, was placed around the aperture's opening as shown in Fig. 7.5(b). The performance of the proposed geometry is compared with an aperture without EBGs and an aperture surrounded with lossy resistive sheets (shown in Fig. 7.5(c)) as in [131]. Although various possibilities for the choice of the material parameters for the resistive sheets were made in [131], here, $\mu_r = 1$, $\epsilon_r = 4$, $\sigma = 30\ \Omega^{-1}m^{-1}$ and width of 6 mm were used.

Within the numerical computational domain, the source and monitor points shown in Fig. 7.6 are placed $40mm$ away from the plane of the aperture in opposite directions along an axis normal to the aperture (and structure). The electric field is then captured at the other side of the aperture using field probes. These probes are used to record one particular component of the electromagnetic field at a specified location during the transient analysis. A modified version of the perfectly matched layer (convolution PML) is used in CST MWS to terminate the computational domain, which is capable of simulating infinite conducting screens when positioned normally to the computational domain. Note that with the orientation of the conducting screen, any perfectly conducting sheet that is positioned normal to the computational boundary is effectively stretched to infinity.

7.5 Numerical results

An adaptive hexahedral mesh scheme was adopted during the transient simulations with mesh density of 15 lines per wavelength. The total number of hexahedral mesh cells reached 1,050,512 mesh cells for the loaded aperture with EBGs, 485,760 cells for the resistive coating, and 400,100 mesh cells for the unloaded case.

Fig. 7.7 depicts the numerical results for an x-polarized E-field probe placed in the near-field zone of the aperture's opening for the aforementioned cases. With EBG loading, a reduction of nearly 25 dB at the aperture's enhanced radiation is achieved in comparison to the resistive sheet coating that achieved a reduction of nearly 15 dB. The aperture case without EBGs experienced enhanced radiation captured at the aperture's resonance frequency due to presence of significant current along the aperture as discussed previously in section 7.2.

Figs. 7.8- 7.10 show the far-field radiation from the aperture measured at three different observation points: $160mm$, $250mm$ and $300mm$ away from the aperture's opening.

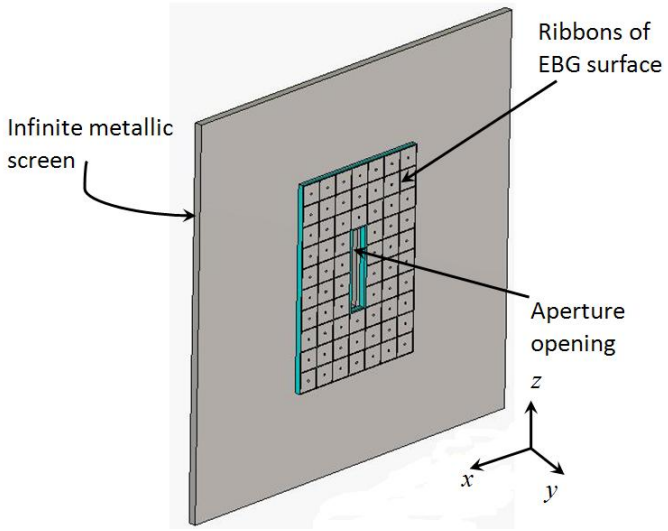

(a)

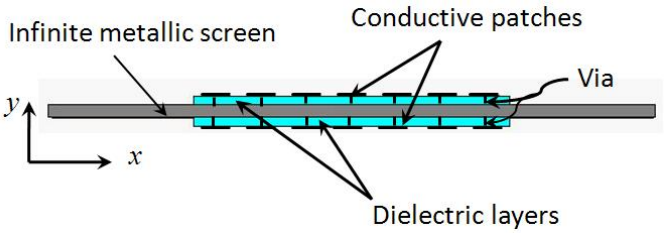

(b)

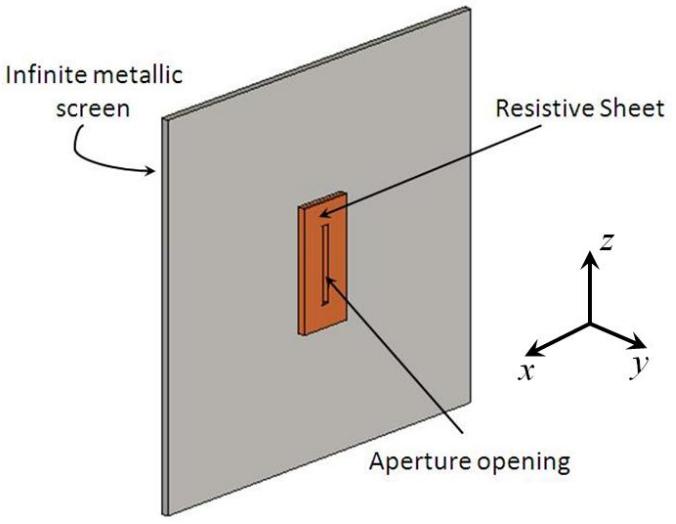

(c)

Figure 7.5: (a) The aperture with 3 layers of EBGs coated around the vicinity of the aperture's opening:(a) perspective view, (b) top view; (c) the loaded aperture case with resistive sheet coating. The aperture measures $20mm$ x $2mm$.

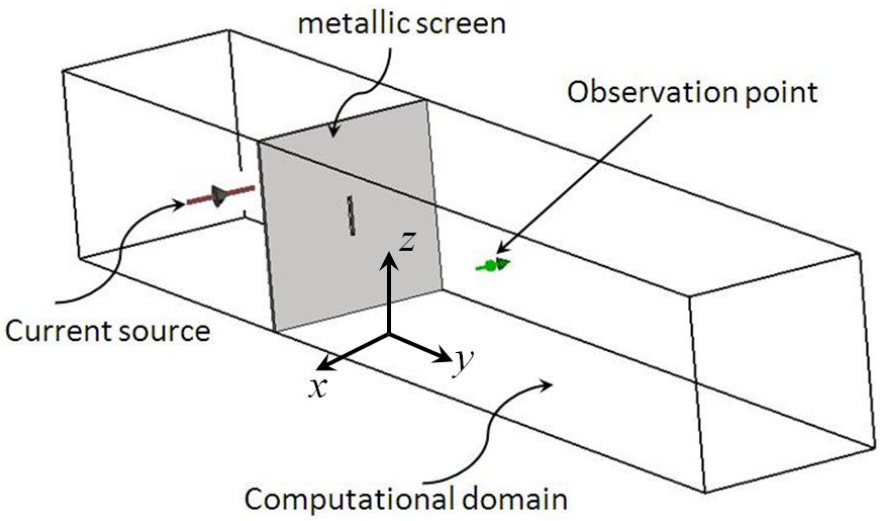

Figure 7.6: Schematic model for the computational domain for the unloaded aperture case.

Within the bandgap zone of the EBG structure, more than 25 dB reduction of field leakage through the aperture is achieved. From the above results, it is observed that the suppression of the near-field electromagnetic radiation from the aperture using EBGs is not as significant as the the suppression achieved by the resistive sheet coating. However, significant suppression of far-field radiation (see Fig. 7.8) is attainable for the aperture with EBGs in comparison to the aperture case with resistive sheets. Nonetheless, EBG structures have advantages over the relatively expensive magnetic and lossy materials when electromagnetic radiation mitigation from apertures and enclosures is concerned. EBG structures are cost effective, easy to design and fabricate, and do not suffer from excessive losses at microwave frequencies as magnetic materials, like ferrites, and other lossy materials experience. However, a drawback to using this particular EBG structure considered here is the frequency bandwidth over which electromagnetic radiation is mitigated.

An interesting observation to point out here is the enhanced radiation at the edges of the bandgap zone obtained from the Brillouin diagram for the EBG structure, as originally observed by Sievenpiper *et al.* [45]. EBG structures at their irreducible Brillouin zone have unique propagating (surface wave) modes over a certain frequency band. Within the bandgap regime of EBGs, no real propagating waves are possible and within which signal propagation is inhibited. However, EBG structures support slow-wave modes that exist at the edges of the bandgap zone as previously noted in [130]. Within the supported slow-wave propagation in EBG structures, the effective wavelength is much smaller than the wavelength in free-space or the dielectric substrate. Hence, it is of fundamental

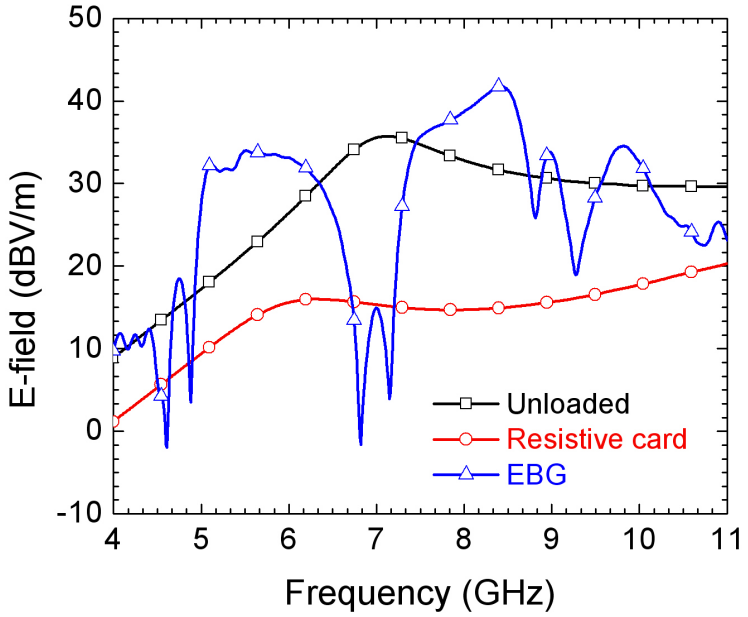

Figure 7.7: Simulation results for the electric field strength captured at a distance of $40mm$ from aperture.

importance that EMI/EMC engineers be aware of the consequence of such modes.

A parametric study based on varying the number of EBG layers in the vicinity of the aperture is also conducted as shown in Fig. 7.11. This is to gain more insight into the effect of EBG layers on the strength of field leakage through apertures. Figs. 7.11(a)-7.11(c) show ribbons of EBGs with 1 layer, 2 and 3 layers, respectively. The near-field radiation properties of the three geometries are presented in Fig. 7.12. With only a layer of EBG surface, the electric field strength at the aperture's resonance was 0.6 dBV/m, while interestingly it reached -13 dBV/m when 2 layers of EBG is used. The third case (see Fig. 7.11(c)) shows field strength of 3 dBV/m with two dips observed at 7.1 GHz and 6.8 GHz.

Fig. 7.13 shows the surface current distribution at the external surface of the metallic screen with EBGs placed around the aperture. Significant reduction of electromagnetic radiation from the aperture with EBGs is visible as compared to the aperture case without EBGs shown in Fig. 7.1, due to the suppressed surface currents.

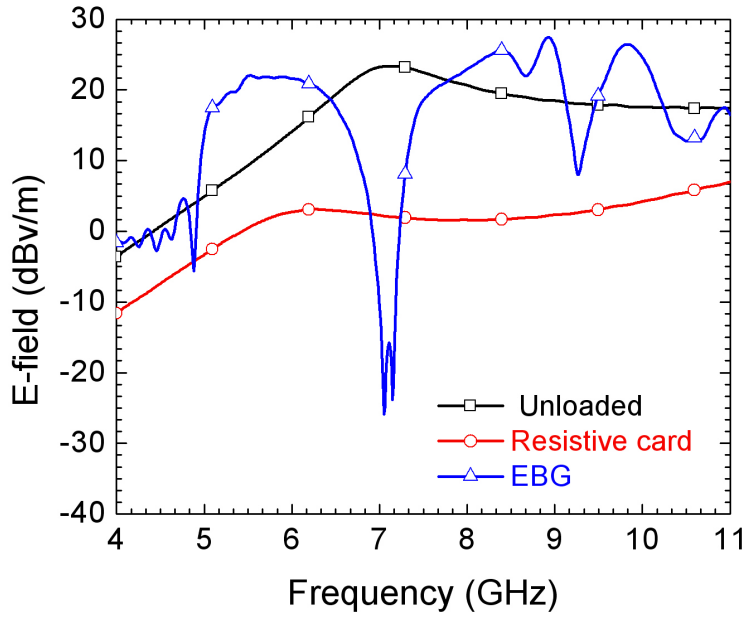

Figure 7.8: Simulation results for the electric field strength captured at a distance of $160mm$ from aperture.

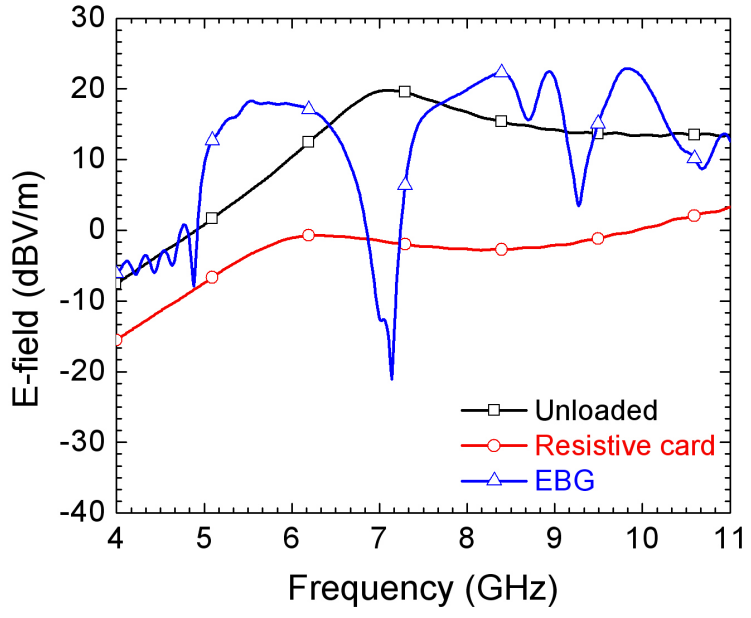

Figure 7.9: Simulation results for the electric field strength captured at a distance of $250mm$ from aperture.

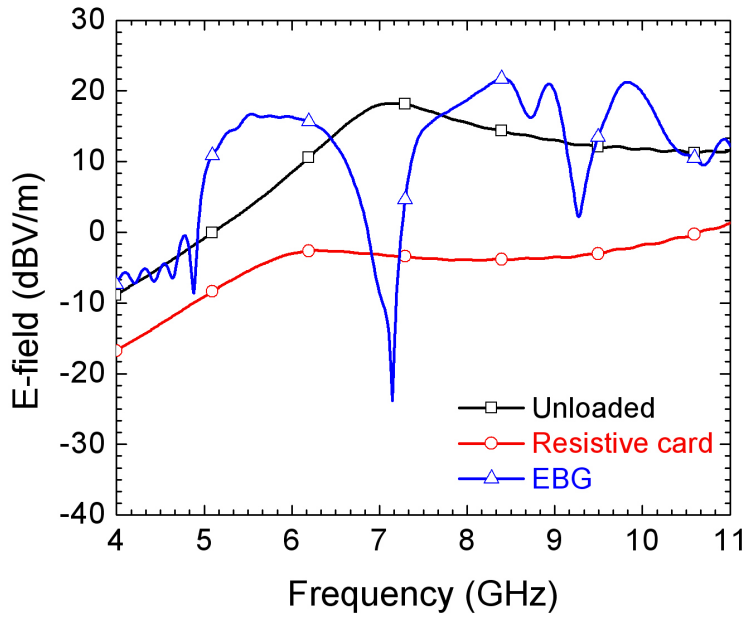

Figure 7.10: Simulation results for the electric field strength captured at a distance of $300mm$ from aperture.

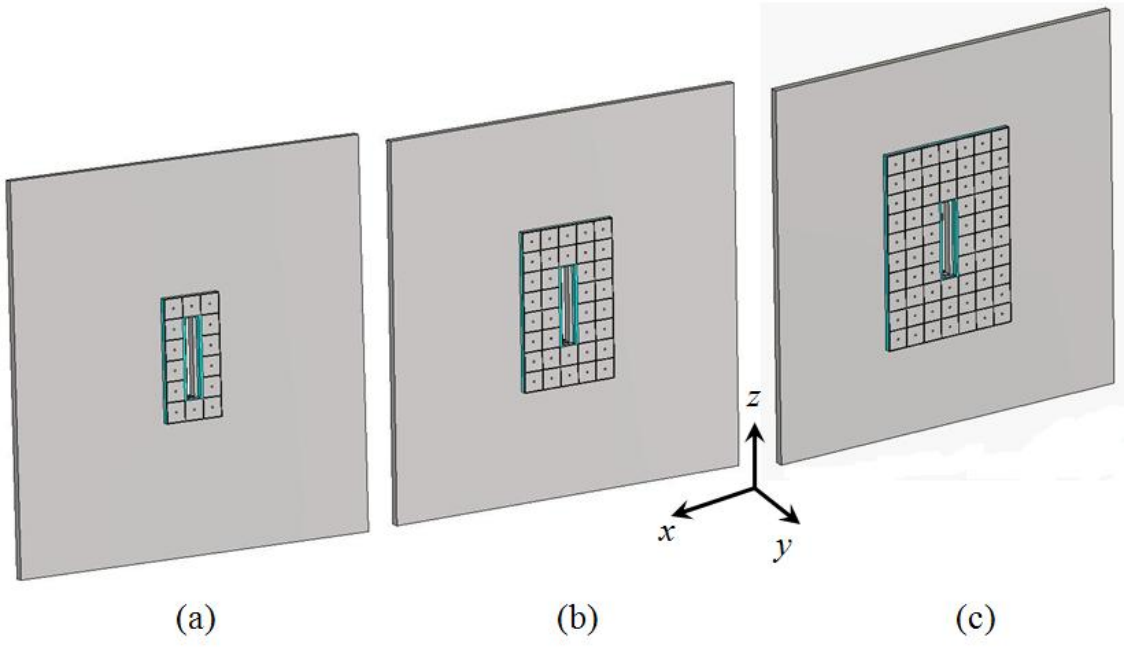

Figure 7.11: The proposed aperture geometry with EBG surfaces having: (a) 1-layer, (b) 2-layers, and (c) 3-layers surrounding the aperture in both sides of the metallic screen.

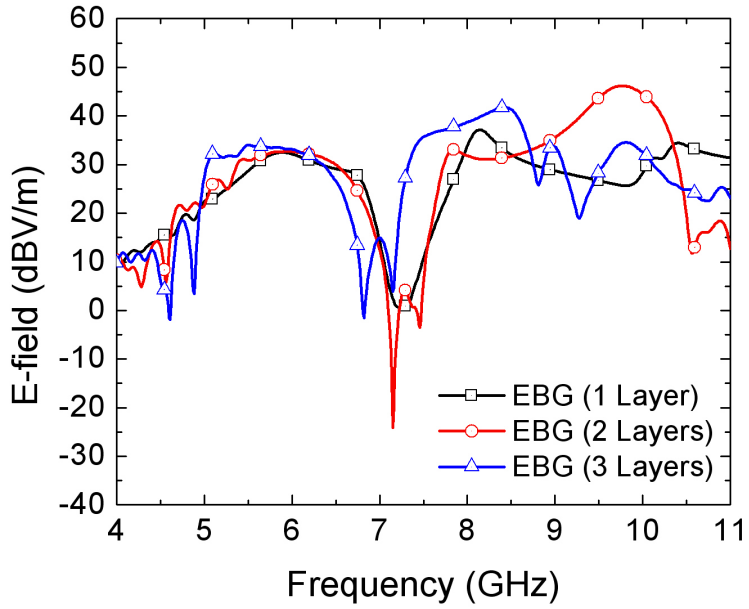

Figure 7.12: A parametric study conducted based on varying the number of EBG surfaces around the aperture. The figure shows simulation results for the electric field strength captured at a distance of 40 mm from aperture's opening.

7.6 Versatility of EBG structures: case studies from real-world environment

Several frequencies that give rise to electromagnetic radiation are often encountered in modern electronic systems. One of which is the frequency of an internal radiator within a system (i.e., secondary radiating source), such as heat sink, connectors, amongst others. Other frequencies that are sources of enhanced radiation are the resonant frequencies of enclosures and those of the slots or apertures present on the enclosures. Once electromagnetic radiation takes place at those frequencies, some of this energy leaks out through apertures, and create currents on the outside environment. Such currents form coupling paths (through cables) eventually result in EMI and unwanted radiated emissions. In fact, the aforementioned sources of radiation are very critical issues for compliance of EMC requirements.

In this section, several case studies from real-world environment are investigated. This will provide additional understanding into the nature of electromagnetic radiation initiated by the aforementioned frequencies. Furthermore, the viability and robustness of EBG structures is demonstrated through the case studies in minimizing electromagnetic

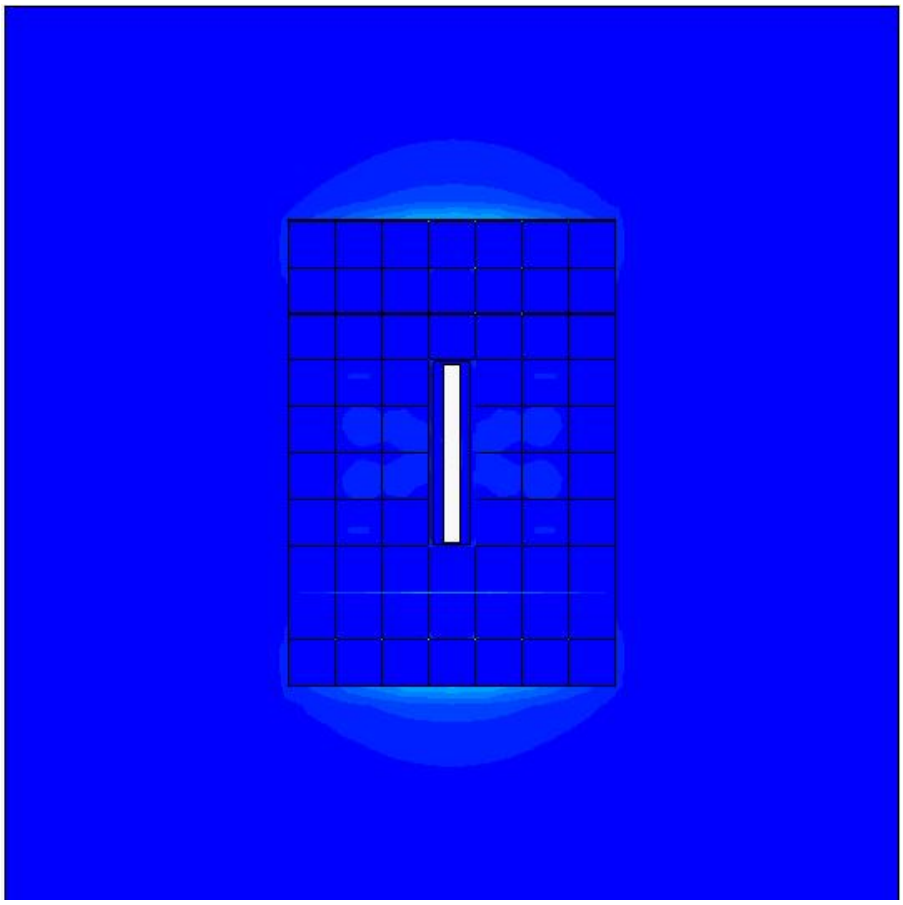

Figure 7.13: Snapshot for the surface current distribution at the external surface of the loaded metallic screen with EBG structure.

radiation from metallic enclosures with openings. Finally, the numerically modeled case studies are validated against a fabricated prototype.

7.6.1 Case I: electromagnetic field leakage through apertures due to internal source of noise

A source of noise is considered that mimics a central processing unit (CPU) signal (i.e., clock) or any of its subsequent harmonics placed inside a metallic enclosure. The enclosure has an opening (aperture). What is of interest in such a scenario is to minimize the electromagnetic field leakage through the aperture due to the source of noise and to immune the enclosure from any external EMI threats, while keeping the aperture size constant. This scenario is described as shown in Fig. 7.14. A source of noise is modeled here as a dipole antenna resonating at 4.8 GHz and placed at the center of the metallic enclosure, $40mm$ distant away from an aperture opening. The metallic enclosure measures $80mm$ x $100mm$ x $45mm$ in x, y, and z directions, respectively. Note that the cut-off frequency of the metallic enclosure is considered below the processor's clock frequency. The aperture has a length of $20mm$ and resonates around 7.0 GHz. In this particular case study, we intentionally seek to minimize electromagnetic radiation due to internal source of noise (clock signal). Thus, the EBG structure has been designed, as was discussed in section 7.3, with its band gap zone covering particularly the source of radiation around 4.8 GHz. As shown in Fig. 7.14, a ribbon of EBG surface is placed around the aperture so that surface currents are mitigated especially along the shorter edges of the opening. An observation point (probe) is placed 40 mm away from the aperture's side to capture the electric field strength in the near-field zone of the enclosure. This case study is compared against a reference case without EBGs.

Fig. 7.15 shows the electric field strength with and without the EBG surface. Significant suppression of electromagnetic radiation starting from 4.5 GHz and even extending to 5 GHz can be seen. More than 10 dB reduction of field leakage is achieved when using EBGs surrounding the perimeter of the aperture.

7.6.2 Case II: Reduction of radiation at aperture's resonance

In this study, the main emphasis is on suppressing radiation coinciding with the resonance frequency of the aperture. Fig. 7.16 shows the numerical results for the electric field strength with and without the placement of EBGs around the aperture's opening. Significant reduction of radiation from the aperture is achieved, covering the bandgap zone (see Fig. 7.4) extending from 6.8 GHz to 7 GHz. It is important to emphasize here

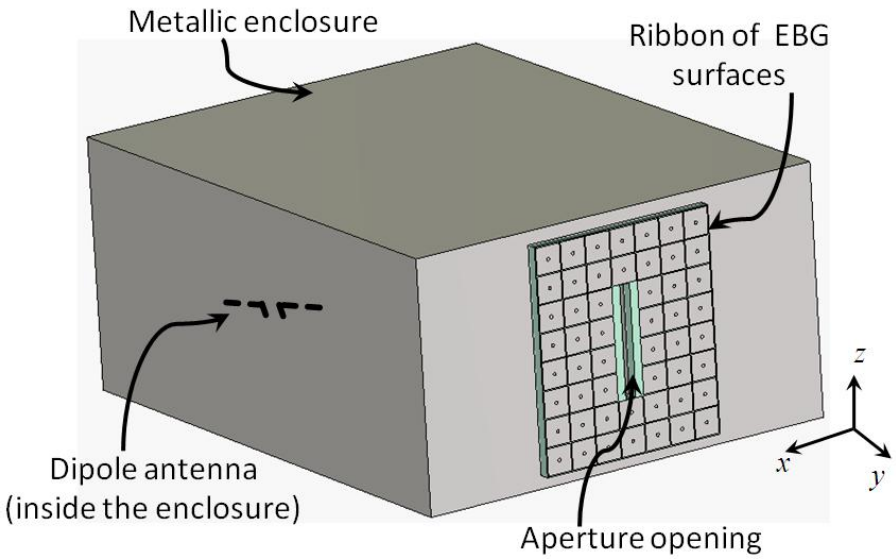

Figure 7.14: Schematic model for the EMI case study with the proposed technique.

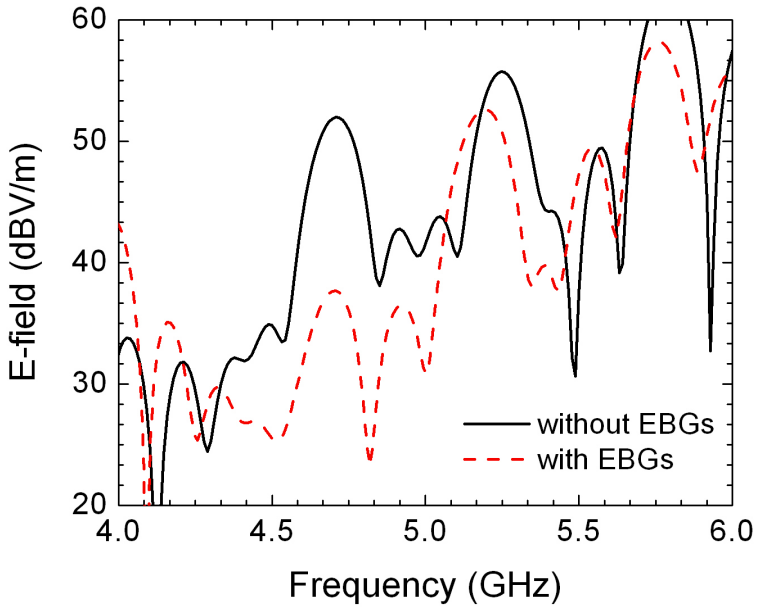

Figure 7.15: Simulation results for the x-polarized E-field captured using a probe in the near-field of the aperture.

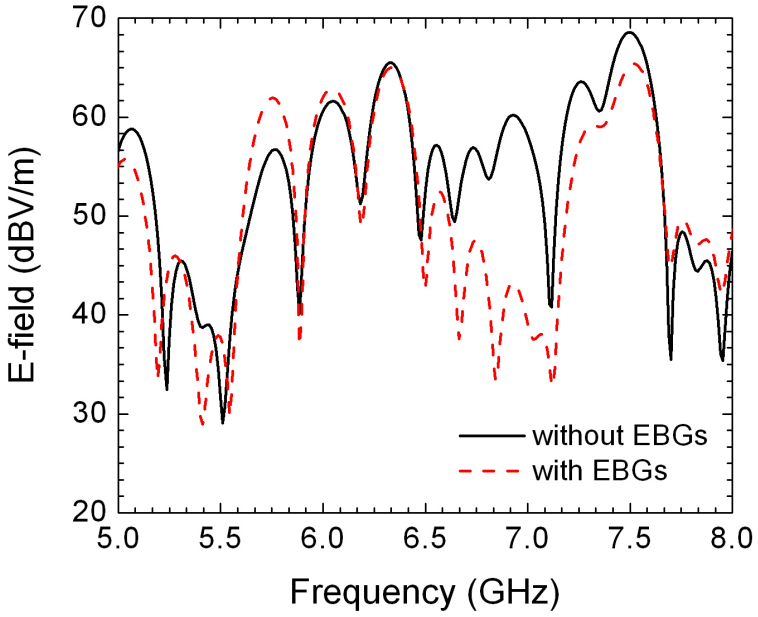

Figure 7.16: Simulation results for the x-polarized E-field captured using a probe in the near-field of the aperture.

that maximum radiation outside the enclosure does not necessarily occur at the frequency where the primary source of energy radiates the most, which in this particular example was a dipole antenna resonating at 3.5 GHz. However, it is possible to have enhanced radiation at other frequency components that will depend on the resonance frequencies of the enclosure (cavity) as well as the aperture's resonance frequency.

7.6.3 Experimental validation

For ease of demonstration, a cubic box of styrofoam ($\epsilon_r \approx 1.03$) was covered by a 1 mm thick aluminum foil with an opening of $20mm$ x $2mm$ representing the aperture. The metallic box measures $80mm$ x $100mm$ x $45mm$. As a source of noise, a monopole antenna was used and placed along one of the enclosure's sides (see Fig. 7.17) $40mm$ away from the aperture. The monopole antenna had a resonance frequency of 7 GHz. The aperture's resonance frequency was approximately 7 GHz. A monopole antenna perpendicular to the aperture was used to capture the energy leaking out of the metallic box through the aperture. For accurate measurement setup, a support (non-conductive) layer was used to sustain the probe in a fixed position $40mm$ away from the aperture and the antenna was placed normal to the aperture's opening. This is to insure capturing the maximum electric field that is radiated by the aperture at resonance. Fig. 7.17 depicts a photo of

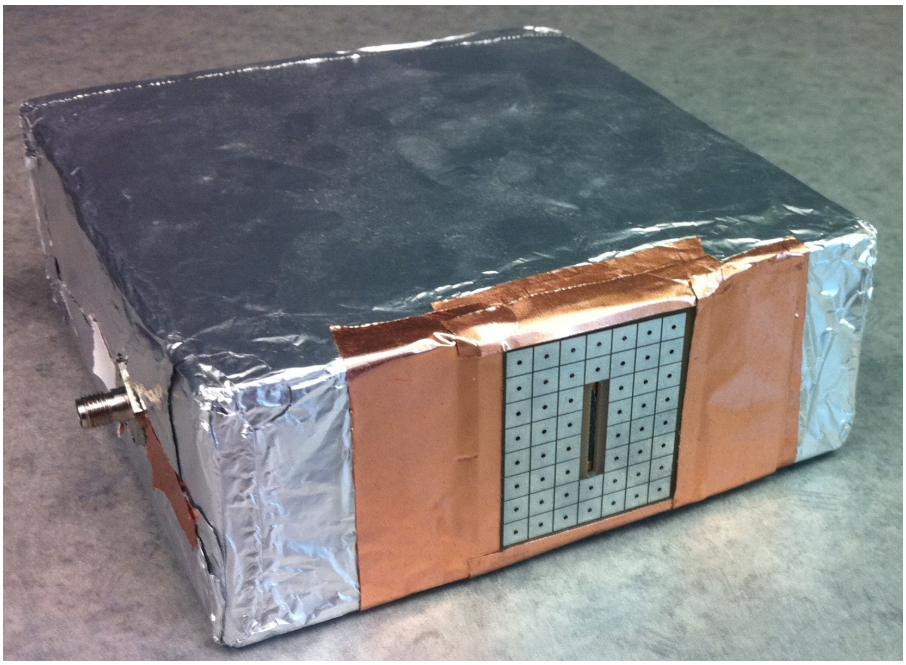

Figure 7.17: A perspective view of the enclosure with EBG ribbon placed around the aperture. Note the location of the source of noise along the side of the enclosure.

the enclosure with a ribbon of EBGs placed around the aperture's opening. The EBG structure was fabricated using a low-loss FR-4 laminate with a thickness $h = 1.5mm$, EBG patches $a = 4.8mm$, gap $g = 0.2mm$, and via diameter $d = 0.8mm$.

The amount of energy leakage is proportional to the transmission coefficient S_{21} between the transmitter (source of noise) and victim location (monopole probe). To ensure that the aluminum covered styrofoam box, in the absence of the aperture acts as a shield, the aperture was initially covered with copper tape and the external radiation was recorded. Fig. 7.18 depicts the S_{21} measured between the internal and external monopole antennas when the aperture was sealed with copper tape. A transmission coefficient of -50dB or lower is observed, a sufficient indication of the shielding effectiveness of the enclosure, especially for the validation purpose intended here.

Fig. 7.19 depicts the measured transmission coefficient for the case with and without EBGs. More than 15 dB reduction of field leakage is achieved around 7.1 GHz with EBG surfaces placed at the external side of the aluminum box as compared to the case without EBGs. This field leakage reduction indicates significant surface current mitigation, and hence reduction in radiation. It is noted that the EBGs considered in this work had a limited bandwidth. It is conceivable that different EBG structures (for example, planar EBGs) can be designed with wider bandgaps. Wideband EBGs are the subject of current

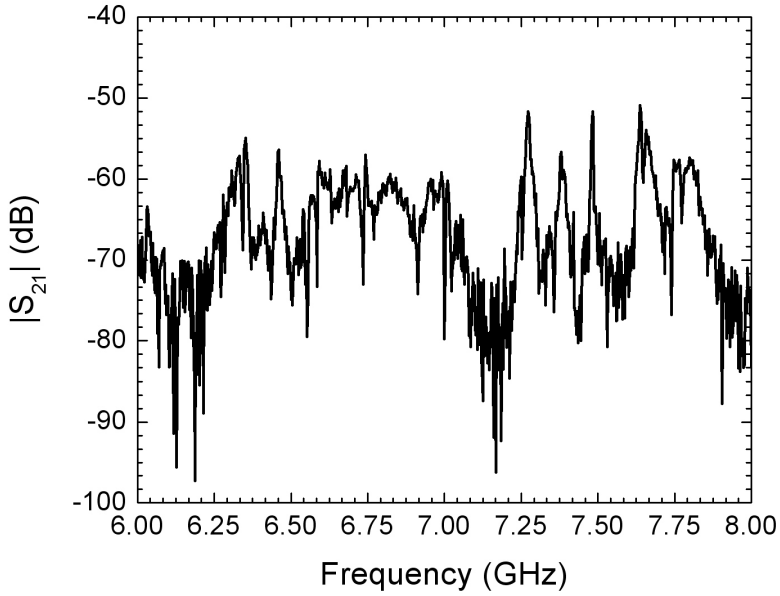

Figure 7.18: Measured transmission coefficient S_{21} for the enclosure when sealing the aperture opening.

research.

7.7 Conclusion

In this chapter, novel use of EBG structures for mitigating electromagnetic field leakage through apertures placed in infinitely large conducting screens and in enclosures was presented. EBG surfaces were loaded in the immediate vicinity of the aperture's opening. Numerical results were presented to validate the concept and provide insight into the underlying phenomenon of electromagnetic radiation from openings.

Through full-wave numerical simulations, it was demonstrated that EBG structures are effective in suppressing electromagnetic radiation from apertures. Qualitatively, it was shown that by using EBGs, more than 15-dB reduction of near- and far-field radiation from the aperture is possible without affecting the aperture's size and shape. This radiation reduction was attainable when using ribbon of EBG surfaces placed around the immediate vicinity of the aperture. Furthermore, a parametric study for the effects of EBG layers on radiation reduction was conducted. To demonstrate the validity and advantages of EBG structures in reducing electromagnetic radiation from apertures and metallic enclosures, several case studies from real-world environment were presented, dis-

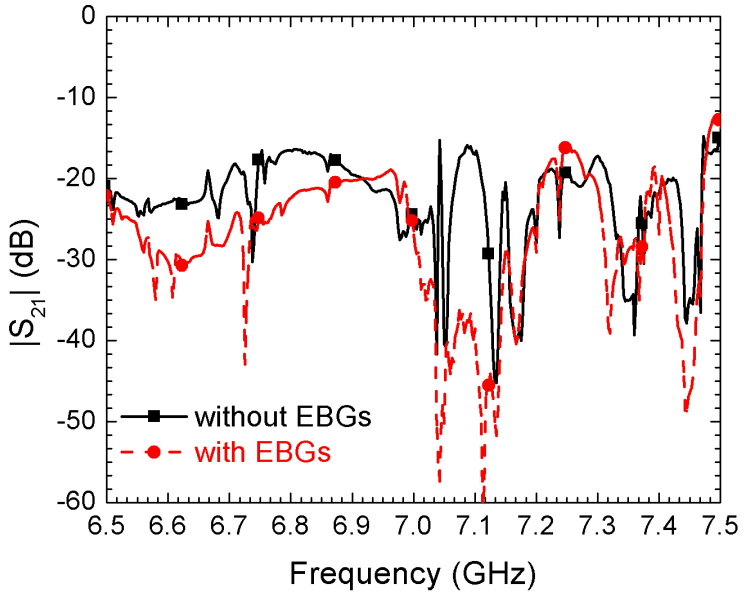

Figure 7.19: Measured transmission coefficient S_{21} for the case study with and without loaded EBGs in presence of the aperture.

cussed, and compared with experimental work. The findings based on this study will prove useful in mitigating EMI/EMC radiated emissions.

Chapter 8

Concluding Remarks

8.1 Summary and Contributions

In summary, sources of electromagnetic coupling and noise in antennas and electromagnetic systems were investigated. A literature review covering state-of-art techniques and methodologies used to mitigate such disturbances were discussed. With focus targeted to decoupling antenna systems, an adequate performance in terms of antenna system matching, far-field patterns has to be maintained.

Several concluded remarks based on the pursued research work in this dissertation are highlighted below. The mechanisms of mutual coupling among high-profile antenna elements are indeed more challenging. This is because of the significant coupling effects arise due to the displacement currents that exist both in the finite chassis and in between the antenna elements. Such currents form strong capacitive coupling path between the radiating elements. Furthermore, the mutual coupling mechanism in low-profile antenna systems is different from the mechanism encountered in high-profile antennas. This is expected, due to the nature of the antennas' profile, and the type of modes that are excited by the dielectric slabs presented in the low-profile antenna systems. The utilization of the developed electromagnetic artificial media for mutual coupling reduction in the pursued antenna systems is envisaged. The findings based on the mutual coupling studies have resulted in several advancements in terms of reducing the mutual coupling effects (more than 20-dB reduction) that can be advantageous to many antenna and communication engineers, improving the antennas' impedance matching, and have maintained good far-field performance. The achieved coupling reduction between high-profile monopole antenna elements when using artificial magnetic materials had resulted in achieving low correlation between the antenna elements as compared to the case without the artificial

magnetic materials.

Simultaneous switching noise and electromagnetic radiation mechanisms in high-speed digital circuits had been addressed. These disturbances arise from power plane resonances that remain a challenging task for EMC engineers. Novel technique based on cascaded complementary resonators was proposed to achieve an ultra-wideband suppression of switching noise, and to overcome the shortcomings of previous methodologies known in literature. Experimental work was performed to assess the robustness of the perforated power plane topology, and to ensure minimal electromagnetic radiation from the perforated PCB boards. Furthermore, signal integrity analysis was studied using the assessment of eye-diagrams for several practical cases. After careful studies, the CSRRs-power plane topology is cost-effective and will prove useful for next generation integrated circuits packaging and power islanding.

Most, if not all, electronic equipment have openings (slots) that are frequently used for air-flow and heat transfer, among other features. Those slots come part of the system, and cannot be avoided in many cases. The slots are efficient radiators, and produce significant electromagnetic radiation, which then couple and interfere either internally and/or externally with nearby electronic devices (secondary radiators). In this dissertation, novel use of EBG structures was proposed with aims to mitigate electromagnetic radiation from apertures and enclosures with openings. The employed EBG structures resulted in significant reduction of electromagnetic field leakage through apertures and enclosures. Practical case studies were numerically studied and experimentally validated.

In this dissertation, the following contributions were accomplished.

- Developed and designed artificial magnetic materials based on the modified SRR (MSSR) inclusion to decouple high-profile monopole antennas. The decoupling layer has improved the matching of the antenna system and significantly reduced the mutual coupling by more than 20-dB between the antenna elements spaced by $\lambda_0/6$.

- Evaluated the performance of the high-profile antenna systems for MIMO systems.

- Introduced analytical models useful to design any sub-wavelength complementary resonator. The formulation predicts the frequency-dependence of the effective electric permittivity ϵ_{eff} of the complementary resonator. Full-wave numerical models were also developed and retrieved to compare with the proposed analytical models.

- Developed novel inclusion based on the sub-wavelength complementary resonators that has high filtering suppression and bandwidth capability.

- Introduced novel structure to decouple low-profile patch antenna elements. The mutual coupling between the patch antennas was numerically evaluated, and experimentally validated.

- Introduced novel technique based on CSRRs for wideband simultaneous switching noise (SSN) mitigation in high-speed printed circuit boards. The designed configuration was evaluated numerically and validated against fabricated prototypes. Good agreement between numerical simulations and measurements was achieved. An ultra-wideband mitigation of SSN was obtained covering frequency band from the sub 1 GHz and extending to 12 GHz. Furthermore, the potential electromagnetic radiated emissions from the perforated boards (i.e., boards with CSRRs) was experimentally investigated.

- Evaluated the signal integrity performance of several developed prototypes using the proposed technique. Robust signal integrity performance was achieved.

- Introduced novel use of EBG structures to mitigate electromagnetic field leakage and undesirable radiation from apertures and enclosures. A case study from real-world environment was also presented, evaluated numerically and validated experimentally.

8.2 Suggested Future Work

The following items will be of interest to pursue

- Provide more accurate models for the engineered complementary resonators. Several approximations had been made to the model proposed in Chapter 3 with satisfactory agreement with numerical retrieved results. Furthermore, investigate other sub-wavelength particles, to name a few spirals, and space-filling particles (Hilbert curves).

- Investigate the mutual coupling between planar slot antennas. These antennas are widely used in aircrafts. The use of artificial complementary resonators to reduce the coupling among slot antenna arrays shall be considered. This has the advantage of avoiding the need for three layers when using embedded EBG structures [132].

- Evaluate the performance of the patch antenna array with the artificial complementary structures in the context of array processing, specifically for direction of arrival (DOA) estimation. Since mutual coupling between the antenna elements leads to

system performance degradation (i.e., radiation pattern distortion), this DOA estimation is of particular interest in order to assess the strength of the antenna system in rejecting particular impinging interference signals.

- Develop artificial magnetic materials to decouple loop antennas for magnetic resonance imaging (MRI) applications. One of the big challenges in MRI imaging is the strong mutual coupling effects that arise due to the close proximity of the coils next to each others. In practice, arrays of such coils are used to produce significant magnetic field to excite the molecules of human body. Due to the encountered coupling, degradation in the matching of the antennas makes the tunability and fabrication of such coils cumbersome for MRI engineers. Furthermore, the strong interaction between the coils reduces the signal-to-noise ratio (SNR) and thus poses some limitations on the quality and resolution of the images when scanning various human body tissues.

- Perform co-simulations incorporating full-wave solvers with circuit simulators for the proposed power planes in Chapter 6 for time-domain analysis and characterization of the simultaneous switching noise.

- Develop transmission line models for enclosures with EBG structures for EMI shielding effectiveness evaluation, and compare with the results of the proposed mitigation technique accomplished in chapter. 7.

Bibliography

[1] S. Shahparnia and O.M. Ramahi. Electromagnetic interference (EMI) reduction from printed circuit boards (PCB) using electromagnetic bandgap structures. *IEEE Trans. Electromagn. Compat.*, 46(4):580–587, Nov. 2004. xii, 18, 20, 23

[2] O.M. Ramahi, V. Subramanian, and B. Archambeault. A simple finite-difference frequency-domain (FDFD) algorithm for analysis of switching noise in printed circuit boards and packages. *IEEE Trans. Adv. Packaging*, 26(2):191–198, May 2003. xii, 17, 19

[3] R. Marqués, F. Martín, and Sorolla, M. *Metamaterials with Negative Parameters: Theory, Design and Microwave Applications.* John Wiley and Sons Inc., 2008. xiii, 38, 39, 66

[4] G. J. Foschini and M. J. Gans. On limits of wireless communications in a fading environment when using multiple antennas. *Wireless Personal Commun.*, 6(3):311–335, 1998. 2

[5] R.G. Vaughan, and J.B. Andersen. Antenna diversity in mobile communications. *IEEE Transactions on Vehicular Technology*, 36(4):149–172, Nov. 1987. 2, 58

[6] Constantine A. Balanis. *Antenna Theory Analysis and Design.* John Wiley and Sons Inc., Third Edit. edition, 1982. 2, 7

[7] R. Janaswamy. Effect of element mutual coupling on the capacity of fixed length linear arrays. *IEEE Antenna Wireless Propagat. Lett.*, 1(1):157–160, 2002. 2

[8] David M. Pozar, and D. Schaubert. *Microstrip antennas: the analysis and design of microstrip antennas and arrays.* John Wiley and Sons Inc., 1995. 2, 12, 13

[9] James E. Buchanan. *Signal and Power Integrity in Digital Systems: TTL, CMOS, and BiCMOS.* McGraw-Hill, 1995. 2, 17

[10] L. Smith. Simultaneous switch noise and power plane bounce for CMOS technology. In *Electrical Performance of Electronic Packaging, San Diego, CA, USA*, pages 163–166, Oct. 1999. 2, 17

[11] Ramesh Senthinathan and John L. Prince. *Simultaneous switching noise of CMOS devices and systems*. Kluwer Academic Publishers, 1994. 2, 3

[12] M. Leone. The radiation of a rectangular power-bus structure at multiple cavity-mode resonances. *IEEE Trans. Electromagn. Compat.*, 45(3):486–492, aug. 2003. 3, 86

[13] A.A. Pistolkors. The radiation resistance of beam antennas. *Proceedings of the Institute of Radio Engineers*, 17(3):562–579, March 1929. 8

[14] E. C. Jordan, and K. G. Balmain. *Electromagnetic Waves and Radiating Systems*. Prentice-Hall Inc., Second Edit. edition, 1988. 8

[15] J. Andersen and H. Rasmussen. Decoupling and descattering networks for antennas. *IEEE Trans. Antennas Propag.*, 24(6):841–846, Nov 1976. 10, 49, 51

[16] Shin-Chang Chen, Yu-Shin Wang, and Shyh-Jong Chung. A decoupling technique for increasing the port isolation between two strongly coupled antennas. *IEEE Trans. Antennas Propag.*, 56(12):3650–3658, Dec. 2008. 10, 49

[17] S. Dossche, S. Blanch, and J. Romeu. Three different ways to decorrelate two closely spaced monopoles for MIMO applications. In *2005 IEEE/ACES International Conference on Wireless Communications and Applied Computational Electromagnetics*, pages 849–852, April 2005. 10, 11

[18] Chi-Yuk Chiu, Chi-Ho Cheng, R.D. Murch, and C.R. Rowell. Reduction of mutual coupling between closely-packed antenna elements. *IEEE Trans. Antennas Propag.*, 55(6), June 2007. 10, 15

[19] M. Sonkki and E. Salonen. Low Mutual Coupling Between Monopole Antennas by Using Two $\lambda/2$ Slots. *IEEE Antenna Wireless Propagat. Lett.*, 9:138–141, March 2010. 10

[20] Tzung-I Lee and Y.E. Wang. Mode-based information channels in closely coupled dipole pairs. *IEEE Trans. Antennas Propag.*, 56(12):3804–3811, Dec. 2008. 11

[21] C. Volmer, J. Weber, R. Stephan, K. Blau, and M.A. Hein. An eigen-analysis of compact antenna arrays and its application to port decoupling. *IEEE Trans. Antennas Propag.*, 56(2):360–370, Feb. 2008. 11

[22] P.J. Ferrer, J.M. Gonzalez-Arbesu, and J. Romeu. Decorrelation of two closely spaced antennas with a metamaterial AMC surface. *Microwave and Opt. Tech. Letts.*, 50(5):1414–1417, May 2008. 11, 54

[23] M. M. Bait-Suwailam, M. S. Boybay, and O. M. Ramahi. Mutual coupling reduction in MIMO antennas using artificial magnetic materias. In *the 13th International Symp. on Antenna Technology and Applied Electromagnetics (ANTEM/URSI)*, pages 1–4, Feb. 2009. 11

[24] M.M. Bait-Suwailam, M.S. Boybay, and O.M. Ramahi. Electromagnetic coupling reduction in high-profile monopole antennas using single-negative magnetic metamaterials for mimo applications. *IEEE Trans. Antennas Propag.*, 58(9):2894–2902, Sept. 2010. 11

[25] R. Marques, F. Mesa, J. Martel, and F. Medina. Comparative analysis of edge- and broadside- coupled split ring resonators for metamaterial design - theory and experiments. *IEEE Trans. Antennas Propag.*, 51(10):2572–2581, Oct. 2003. 11, 31, 32, 51

[26] S.A. Bokhari, J.-F. Zurcher, J.R. Mosig, and F.E. Gardiol. Near fields of microstrip antennas. *IEEE Trans. Antennas Propag.*, 43(2):188–197, Feb. 1995. 12

[27] M.M. Nikolic, A.R. Djordjevic, and A. Nehorai. Microstrip antennas with suppressed radiation in horizontal directions and reduced coupling. *IEEE Trans. Antennas Propag.*, 53(11):3469–3476, Nov. 2005. 12, 15

[28] D.R. Jackson, J.T. Williams, A.K. Bhattacharyya, R.L. Smith, S.J. Buchheit, and S.A. Long. Microstrip patch designs that do not excite surface waves. *IEEE Trans. Antennas Propag.*, 41(8):1026–1037, Aug. 1993. 12, 14

[29] A.K. Bhattacharyya. Characteristics of space and surface waves in a multilayered structure. *IEEE Trans. Antennas Propag.*, 38(8):1231–1238, Aug. 1990. 12

[30] R. Garg, P. Bhartia, I. Bahl and A. Ittipiboon. *Microstrip Antenna Design Handbook*. Artech-House Inc., 2001. 12

[31] R. Munson. Conformal microstrip antennas and microstrip phased arrays. *IEEE Trans. Antennas Propag.*, 22(1):74–78, Jan. 1974. 13

[32] E. Van Lil and A. Van De Capelle. Transmission line model for mutual coupling between microstrip antennas. *IEEE Trans. Antennas Propag.*, 32(8):816–821, Aug. 1984. 13

[33] A. Derneryd. Linearly polarized microstrip antennas. *IEEE Trans. Antennas Propag.*, 24(6):846–851, Nov. 1976. 13

[34] R. Jedlicka, M. Poe, and K. Carver. Mutual coupling between rectangular and circular microstrip elements. In *IEEE Antennas and Propagation Society International Symposium*, volume 18, pages 750–753, Jun. 1980. 13

[35] E. Penard and J.-P. Daniel. Mutual coupling between microstrip antennas. *Electron. Lett.*, 18(14):605–607, Jul. 1982. 13

[36] M. Malkomes. Mutual coupling between microstrip patch antennas. *Electron. Lett.*, 18(12):520–522, Jun. 1982. 13

[37] E. Newman and P. Tulyathan. Analysis of microstrip antennas using moment methods. *IEEE Trans. Antennas Propag.*, 29(1):47–53, Jan. 1981. 13

[38] D. Pozar. Input impedance and mutual coupling of rectangular microstrip antennas. *IEEE Trans. Antennas Propag.*, 30(6):1191–1196, Nov. 1982. 13

[39] M.A. Khayat, J.T. Williams, D.R. Jackson, and S.A. Long. Mutual coupling between reduced surface-wave microstrip antennas. *IEEE Trans. Antennas Propag.*, 48(10):1581–1593, Oct. 2000. 14

[40] G. Shaker, G. Rafi, S. Safavi-Naeini, and N. Sangary. A synthesis technique for reducing mutual coupling between closely separated patch antennas. In *IEEE International Symposium on Antennas and Propagation Society (APS), San Diego, CA*, pages 1–4, July 2008. 14

[41] Chi-Yuk Chiu, Chi-Ho Cheng, R.D. Murch, and C.R. Rowell. Reduction of mutual coupling between closely-packed antenna elements. *IEEE Trans. Antennas Propag.*, 55(6):1732–1738, June 2007.

[42] A. Diallo, C. Luxey, P. Le Thuc, R. Staraj, and G. Kossiavas. Study and Reduction of the Mutual Coupling Between Two Mobile Phone PIFAs Operating in the DCS1800 and UMTS Bands. *IEEE Trans. Antennas Propag.*, 54(11):3063–3074, Nov. 2006. 14

[43] T. Svantesson. Correlation and channel capacity of MIMO systems employing multimode antennas. *IEEE Transactions on Vehicular Technology*, 51(6):1304–1312, Nov. 2002. 14

[44] E. Rajo-Iglesias, O. Quevedo-Teruel, and M. Sanchez-Fernandez. Compact Multimode Patch Antennas for MIMO Applications. *IEEE Antennas and Propagation Magazine*. 14

[45] D. Sievenpiper, Lijun Zhang, R.F.J. Broas, N.G. Alexopolous, and E. Yablonovitch. High-impedance electromagnetic surfaces with a forbidden frequency band. *IEEE Trans. Microw. Theory Tech.*, 47(11):2059–2074, Nov. 1999. 14, 23, 24, 25, 27, 107

[46] Fan Yang and Y. Rahmat-Samii. Microstrip antennas integrated with electromagnetic band-gap (EBG) structures: a low mutual coupling design for array applications. *IEEE Trans. Antennas Propag.*, 51(10):2936–2946, Oct. 2003. 14

[47] M. Coulombe, S. Farzaneh Koodiani, and C. Caloz. Compact Elongated Mushroom (EM)-EBG Structure for Enhancement of Patch Antenna Array Performances. *IEEE Trans. Antennas Propag.*, 58(4):1076–1086, April 2010. 14

[48] E. Rajo-Iglesias, O. Quevedo-Teruel, and L. Inclan-Sanchez. Mutual Coupling Reduction in Patch Antenna Arrays by Using a Planar EBG Structure and a Multilayer Dielectric Substrate. *IEEE Trans. Antennas Propag.*, 56(6):1648–1655, Jun. 2008. 14

[49] E. Rajo-Iglesias, O. Quevedo-Teruel, and L. Inclan-Sanchez. Planar soft surfaces and their application to mutual coupling reduction. *IEEE Trans. Antennas Propag.*, 57(12):3852 –3859, Dec. 2009. 14

[50] H.S. Farahani, M. Veysi, M. Kamyab, and A. Tadjalli. Mutual Coupling Reduction in Patch Antenna Arrays Using a UC-EBG Superstrate. *IEEE Antenna Wireless Propagat. Lett.*, 9:57–59, 2010. 14, 15

[51] P.-S. Kildal. Artificially soft and hard surfaces in electromagnetics. *IEEE Trans. Antennas Propag.*, 38(10):1537–1544, Oct. 1990. 14

[52] Jong-Gwan Yook and L.P.B. Katehi. Micromachined microstrip patch antenna with controlled mutual coupling and surface waves. *IEEE Trans. Antennas Propag.*, 49(9):1282–1289, Sep. 2001. 15

[53] T. Kokkinos, E. Liakou, and A.P. Feresidis. Decoupling antenna elements of PIFA arrays on handheld devices. *Electron. Lett.*, 44(25):1442–1444, 4 2008. 15

[54] Mohsen Salehi and Ahad Tavakoli. A novel low mutual coupling microstrip antenna array design using defected ground structure. *AEU - International Journal of Electronics and Communications*, 60(10):718–723, 2006.

[55] I. Kim, Chang W. Jung, Yongjin Kim, and Young E. Kim. Low-profile wideband MIMO antenna with suppressing mutual coupling between two antennas. *Microwave and Opt. Tech. Letts.*, 50(5):1336–1339, March 2008. 15

[56] K. Buell, H. Mosallaei, and K. Sarabandi. Metamaterial insulator enabled superdirective array. *IEEE Trans. Antennas Propag.*, 55(4):1074–1085, April 2007. 15

[57] P. Mookiah and K.R. Dandekar. Metamaterial-Substrate Antenna Array for MIMO Communication System. *IEEE Trans. Antennas Propag.*, 57(10):3283–3292, Oct. 2009. 15

[58] M.M. Bait-Suwailam, O.F. Siddiqui, and O.M. Ramahi. Mutual Coupling Reduction Between Microstrip Patch Antennas using Slotted-Complementary Split-Ring Resonators. *IEEE Antenna Wireless Propagat. Lett.*, 9:876–878, 2010. 15

[59] T. Kamgaing and O.M. Ramahi. Design and modeling of high-impedance electromagnetic surfaces for switching noise suppression in power planes. *IEEE Trans. Electromagn. Compat.*, 47(3):479–489, Aug. 2005. 16

[60] S. Radu, R.E. DuBroff, T.H. Hubing, and T.P. Van Doren. Designing power bus decoupling for CMOS devices. In *IEEE International Symposium on Electromagnetic Compatibility (EMC)*, volume 1, pages 375–380, Aug. 1998. 18

[61] A. Madou and L. Martens. Electrical behavior of decoupling capacitors embedded in multilayered pcbs. *IEEE Trans. Electromagn. Compat.*, 43(4):549–556, Nov. 2001. 18

[62] Minjia Xu, T.H. Hubing, Juan Chen, J.L. Drewniak, T.P. Van Doren, and R.E. DuBroff. Mitigating power bus noise with embedded capacitance in PCB designs. In *IEEE International Symposium on Electromagnetic Compatibility (EMC)*, volume 1, pages 496–500, Aug. 2001. 18

[63] I. Novak. Reducing simultaneous switching noise and emi on ground/power planes by dissipative edge termination. *IEEE Trans. Adv. Packaging*, 22(3):274–283, Aug 1999. 18

[64] T.M. Zeeff and T.H. Hubing. Reducing power bus impedance at resonance with lossy components. *IEEE Trans. Adv. Packaging*, 25(2):307– 310, May 2002. 18

[65] Xiaoning Ye, D.A. Hockanson, Min Li, Yong Ren, Wei Cui, J.L. Drewniak, and R.E. DuBroff. Emi mitigation with multilayer power-bus stacks and via stitching of reference planes. *IEEE Trans. Electromagn. Compat.*, 43(4):538–548, Nov. 2001. 18

[66] T. Hubing, J. Chen, J. Drewniak, T. Van Doren, Y. Ren, J. Fan, and R. DuBroff. Power bus noise reduction using power islands in printed circuit board designs. In *IEEE International Symposium on Electromagnetic Compatibility*, pages 1–4, May 1999. 18

[67] Microwave Studio, Computer Simulation Technology (CST). http://www.cst.com. 19

[68] T. Kamgaing and O.M. Ramahi. A novel power plane with integrated simultaneous switching noise mitigation capability using high impedance surface. *IEEE Microwave Wireless Comp. Lett.*, 13(1):21–23, Jan 2003. 20, 86

[69] R. Abhari and G.V. Eleftheriades. Metallo-dielectric electromagnetic bandgap structures for suppression and isolation of the parallel-plate noise in high-speed circuits. *IEEE Trans. Microw. Theory Tech.*, 51(6):1629–1639, June 2003.

[70] S. Shahparnia and O.M. Ramahi. Simultaneous switching noise mitigation in PCB using cascaded high-impedance surfaces. *Electron. Lett.*, 40(2):98–100, 22 2004.

[71] S. Shahparnia and O.M. Ramahi. Miniaturised electromagnetic bandgap structures for broadband switching noise suppression in PCBs. *Electron. Lett.*, 41(9):519–520, 28 2005.

[72] T. Kamgaing and O.M. Ramahi. Multiband electromagnetic-bandgap structures for applications in small form-factor multichip module packages. *IEEE Trans. Microw. Theory Tech.*, 56(10):2293–2300, Oct. 2008. 20

[73] Jinwoo Choi, V. Govind, M. Swaminathan, Lixi Wan, and R. Doraiswami. Isolation in mixed-signal systems using a novel electromagnetic bandgap (EBG) structure. In Proc. IEEE 13th Top. Meet. Electr. Perform. Electron. Packag., Portland, OR, pages 199–202, Oct. 2004. 20

[74] Jie Qin, O.M. Ramahi, and V. Granatstein. Novel planar electromagnetic bandgap structures for mitigation of switching noise and emi reduction in high-speed circuits. *IEEE Trans. Electromagn. Compat.*, 49(3):661–669, Aug. 2007. 20, 88

[75] B. Mohajer-Iravani and O.M. Ramahi. EMI Suppression in Microprocessor Packages using Miniaturized Electromagnetic Bandgap Structures with High-k Dielectrics. In *Electromagnetic Compatibility, 2007 IEEE International Symposium*, pages 1–4, 9-13 2007. 20

[76] F. Falcone, T. Lopetegi, J.D. Baena, R. Marques, F. Martin, and M. Sorolla. Effective negative-ϵ stopband microstrip lines based on complementary split ring resonators. *IEEE Microwave Wireless Comp. Lett.*, 14(6):280–282, 2004. 20, 38

[77] J. Bonache, M. Gil, I. Gil, J. Garcia-Garcia, and F. Martin. On the electrical characteristics of complementary metamaterial resonators. *IEEE Microwave Wireless Comp. Lett.*, 16(10):543–545, Oct. 2006. 20

[78] Mohammed M. Bait-Suwailam and O.M. Ramahi. Simultaneous Switching Noise Mitigation in High-Speed Circuits using Complementary Split-Ring Resonators. *Electron. Lett.*, 46(8):563–564, April 2010. 21

[79] Bruce R. Archambeault, Omar M. Ramahi, and Colin Brench. *EMI/EMC Computational Modeling Handbook*. Kluwer Academic Publishers, second edition, 2001. 21

[80] H. A. Bethe. Theory of diffraction by small holes. *Phys. Rev.*, 66(7-8):163–182, Oct. 1944. 22, 100

[81] G. Cerri, R. De Leo, and V.M. Primiani. Theoretical and experimental evaluation of the electromagnetic radiation from apertures in shielded enclosure. *IEEE Trans. Electromagn. Compat.*, 34(4):423–432, Nov 1992. 22

[82] C.H. Kraft. Modeling leakage through finite apertures with TLM. In *Electromagnetic Compatibility, IEEE International Symposium on*, pages 73 –76, 22-26 1994. 22

[83] Min Li, J. Nuebel, J.L. Drewniak, R.E. DuBroff, T.H. Hubing, and T.P. Van Doren. EMI from airflow aperture arrays in shielding enclosures-experiments, FDTD, and MoM modeling. *IEEE Trans. Electromagn. Compat.*, 42(3):265 –275, Aug. 2000.

[84] Min Li, J. Nuebel, J.L. Drewniak, T.H. Hubing, R.E. DuBroff, and T.P. Van Doren. EMI reduction from airflow aperture arrays using dual-perforated screens and loss. *IEEE Trans. Electromagn. Compat.*, 42(2):135–141, May 2000. 22

[85] Ott, H. W. *Noise reduction techniques in electronic systems*. New York: Wiley, second edition, 1998.

[86] C. M. Butler, Y. Rahmat-Samii, R. Mittra. Electromagnetic penetration through apertures in conducting surface. *IEEE Trans. Antennas Propag.*, 26(1):82–93, 1978.

[87] A. Taflove and K. Umashankar. A hybrid moment method/finite-difference time-domain approach to electromagnetic coupling and aperture penetration into complex geometries. *IEEE Trans. Antennas Propag.*, 30(4):617–627, Jul 1982.

[88] Min Li, J. Nuebel, J.L. Drewniak, R.E. DuBroff, T.H. Hubing, and T.P. Van Doren. EMI from airflow aperture arrays in shielding enclosures-experiments, FDTD, and MoM modeling. *IEEE Trans. Electromagn. Compat.*, 42(3):265–275, Aug 2000.

[89] G. Manara, M. Bandinelli, and A. Monorchio. Electromagnetic coupling to wires through arbitrarily shaped apertures in infinite conducting screens. *Microwave and Opt. Tech. Letts.*, 13(1):42–44, April 1996.

[90] T.-L. Wu, H.-H. Chuang, and T.-K. Wang. Overview of Power Integrity Solutions on Package and PCB: Decoupling and EBG Isolation. *IEEE Trans. Electromagn. Compat.*, 52(2):346–356, May 2010. 22

[91] B. Mohajer-Iravani and O.M. Ramahi. Suppression of EMI and Electromagnetic Noise in Packages Using Embedded Capacitance and Miniaturized Electromagnetic Bandgap Structures With High-k Dielectrics. 30(4):776–788, Nov. 2007. 23

[92] D. Qu, L. Shafai, and A. Foroozesh. Improving microstrip patch antenna performance using EBG substrates. *IEE Proc.-Microw. Antennas Propag.*, 153(6):558–563, Dec. 2006. 25

[93] Fan Yang and Y. Rahmat-Samii. Reflection phase characterizations of the EBG ground plane for low profile wire antenna applications. *IEEE Trans. Antennas Propag.*, 51(10):2691–2703, Oct. 2003. 25

[94] L.. Yousefi, B.. Mohajer-Iravani, and O.M. Ramahi. Enhanced bandwidth artificial magnetic ground plane for low-profile antennas. *IEEE Antenna Wireless Propagat. Lett.*, 2007. 25

[95] A. Suntives and R. Abhari. Design of a compact miniaturized probe-fed patch antenna using electromagnetic bandgap structures. In *Antennas and Propagation Society International Symposium (APSURSI), 2010 IEEE*, pages 1–4, 2010. 25

[96] D. F. Sievenpiper. *High-impedance electromagnetic surface*. PhD thesis, University of California at Los Angeles, CA, 1999. 25

[97] L. Brillouin. *Wave Propagation in Periodic Structures:Electric Filters and Crystal Lattices*. McGraw-Hill, 1946. 28

[98] J.B. Pendry, A.J. Holden, D.J. Robbins, and W.J. Stewart. Magnetism from conductors and enhanced nonlinear phenomena. *IEEE Trans. Microw. Theory Tech.*, 47(11):2075–2084, Nov 1999. 29, 30, 32

[99] J. B. Pendry, A. J. Holden, W. J. Stewart, and I. Youngs. Extremely low frequency plasmons in metallic mesostructures. *Phys. Rev. Lett.*, 76(25):4773–4776, Jun 1996. 29

[100] I. S. Schelkunoff and H. T. Friis. *Antennas: Theory and Practice*. John Wiley and Sons Inc., 1952. 30

[101] Richard W. Ziolkowskia and Fabrice Auzanneau. Artificial molecule realization of a magnetic wall. *J. Appl. Phys.*, 82(7):3192–3194, Oct. 1997. 30

[102] R. Marques, F. Medina, and R. Rafii-El-Idrissi. Role of bianisotropy in negative permeability and left-handed metamaterials. *Phys. Rev. B*, 65:144440–6, 2002. 31, 33, 51

[103] K. Buell, H. Mosallaei, and K. Sarabandi. A substrate for small patch antennas providing tunable miniaturization factors. *IEEE Trans. Microw. Theory Tech.*, 54(1):135 –146, Jan. 2006. 31

[104] L. Yousefi and O.M. Ramahi. Miniaturised antennas using artificial magnetic materials with fractal hilbert inclusions. *Electron. Lett.*, 46(12):816 –817, Jun. 2010. 31

[105] Juan D. Baena, Ricardo Marqués, Francisco Medina, and Jesús Martel. Artificial magnetic metamaterial design by using spiral resonators. *Phys. Rev. B*, 69(1):014402, Jan 2004. 31

[106] A. Erentok, P.L. Luljak, and R.W. Ziolkowski. Characterization of a volumetric metamaterial realization of an artificial magnetic conductor for antenna applications. *IEEE Trans. Antennas Propag.*, 53(1):160 – 172, Jan. 2005. 31

[107] J. McVay, N. Engheta, and A. Hoorfar. High impedance metamaterial surfaces using hilbert-curve inclusions. *IEEE Microwave Wireless Comp. Lett.*, 14(3):130–132, 2004. 31

[108] L. Yousefi and O.M. Ramahi. Artificial magnetic materials using fractal hilbert curves. *IEEE Trans. Antennas Propag.*, 58(8):2614 –2622, Aug. 2010. 31

[109] X. Chen and T. M. Grzegorczyk and B. Wu and J. Pacheco and J. A. Kong. Robust method to retrieve the constitutive effective parameters of metamaterials. *Phys. Rev. E*, 70(1):016608.1–016608.7, Jan. 2004. 32, 34, 35, 44, 67, 136

[110] S. Maslovski, P. Ikonen, I. Kolmakov, and S. Tretyakov. Artificial magnetic materials based on the new magnetic particle: Metasolenoid. *Progr. Electromagn. Res. (PIER)*, 54:61–81, Sept. 2005. 32, 33

[111] M. Shamonin, E. Shamonina, V. Kalinin, and L. Solymar. Properties of a metamaterial element: Analytical solutions and numerical simulations for a singly split double ring. *J. Appl. Phys.*, 95(7):3778–3784, Apr. 2004.

[112] R. Marques, F. Mesa, J. Martel, and F. Medina. Comparative analysis of edge- and broadside- coupled split ring resonators for metamaterial design - theory and experiments. *IEEE Trans. Antennas Propag.*, 51(10):2572–2581, Oct. 2003. 32

[113] D. R. Smith, S. Schultz, P. Markoš, and C. M. Soukoulis. Determination of effective permittivity and permeability of metamaterials from reflection and transmission coefficients. *Phys. Rev. B*, 65(19):195104, Apr 2002. 34, 35, 136

[114] Ansoft HFSS. http://www.ansoft.com. 35

[115] J. B. Pendry, A. J. Holden, W. J. Stewart, and I. Youngs. Extremely low frequency plasmons in metallic mesostructures. *Phys. Rev. Lett.*, 76:4773–4776, Jun. 1996. 37

[116] H.G. Booker. Slot aerials and their relation to complementary wire aerials (Babinet's principle). *J. Inst. Elect. Eng., pt. III-A*, 93(4):620–626, May 1946. 38, 39

[117] F. Falcone, T. Lopetegi, M. A. G. Laso, J. D. Baena, J. Bonache, M. Beruete, R. Marqués, F. Martín, and M. Sorolla. Babinet principle applied to the design of metasurfaces and metamaterials. *Phys. Rev. Lett.*, 93(19):197401, Nov. 2004. 39

[118] J.D. Baena, J. Bonache, F. Martin, R.M. Sillero, F. Falcone, T. Lopetegi, M.A.G. Laso, J. Garcia-Garcia, I. Gil, M.F. Portillo, and M. Sorolla. Equivalent-circuit models for split-ring resonators and complementary split-ring resonators coupled to planar transmission lines. *IEEE Trans. Microw. Theory Tech.*, 53(4):1451–1461, Apr. 2005. 39

[119] Inder Bahl and Parakash Bhartia. *Microwave Solid State Circuit Design.* John Wiley and Sons Inc., 2nd edition. 43

[120] W. Wasylkiwskyj and W. Kahn. Theory of mutual coupling among minimum-scattering antennas. *IEEE Trans. Antennas Propag.*, 18(2):204–216, March 1970. 49

[121] Koray Aydin, Irfan Bulu, Kaan Guven, Maria Kafesaki, Costas M Soukoulis, and Ekmel Ozbay. Investigation of magnetic resonances for different split-ring resonator parameters and designs. *New Journal of Physics*, 7:168, 2005. 51

[122] A. Derneryd, and G. Kristensson. Antenna signal correlation and its relation to the impedance matrix. *Electron. Lett.*, 40(7):401–402, April 2004. 58

[123] Hui, H.T., and Lui, H. S. Expression of correlation coefficient for two omindirectional antennas using conventional mutual impedances. *Electron. Lett.*, 44(20):1177–1178, Sept. 2008. 58

[124] S. Blanch, J. Romeu, and I. Corbella. Exact representation of antenna system diversity performance from input parameter description. *Electron. Lett.*, 39(9):705–707, May 2003. 58

[125] J. Thaysen and K. Jakobsen. Envelope correlation in (N, N) MIMO antenna array from scattering parameters. *Microwave and Opt. Tech. Letts.*, 48(5):832–834, May 2006. 58, 59

[126] J. Garcia-Garcia, F. Martin, F. Falcone, J. Bonache, J.D. Baena, I. Gil, E. Amat, T. Lopetegi, M.A.G. Laso, J.A.M. Iturmendi, M. Sorolla, and R. Marques. Microwave filters with improved stopband based on sub-wavelength resonators. *IEEE Trans. Microw. Theory Tech.*, 53(6):1997–2006, June 2005. 66

[127] F. Falcone, T. Lopetegi, M. A. G. Laso, J. D. Baena, J. Bonache, M. Beruete, R. Marqués, F. Martín, and M. Sorolla. Babinet principle applied to the design of metasurfaces and metamaterials. *Phys. Rev. Lett.*, 93(19):197401, Nov 2004. 66, 81

[128] A. B. Abdel-Rahman and A. K. Verma and A. Boutejdar and A. S. Omar. Control of bandstop response of Hi-Lo microstrip low-pass filter using slot in ground plane. *IEEE Trans. Microw. Theory Tech.*, 52(3):1008–1013, March 2004. 66

[129] F. Falcone, T. Lopetegi, J.D. Baena, R. Marques, F. Martin, and M. Sorolla. Effective negative- ϵ stopband microstrip lines based on complementary split ring resonators. *IEEE Microwave Wireless Comp. Lett.*, 14(6):280–282, June 2004. 81

[130] Baharak Mohajer-Iravani and Omar M. Ramahi. Radiating emissions from the planar electromagnetic bandgap (EBG) structures. In *Electromagnetic Compatibil-*

ity (EMC), IEEE International Symposium on, Fort Lauderdale, FL, USA, pages 780–783, 25-30 July 2010. 88, 107

[131] O. M. Ramahi, and Lin Li. Analysis and reduction of electromagnetic field leakage through loaded apertures: a numerical study. *Electromagnetics*, pages 679–693, 2005. 105

[132] K. Payandehjoo and R. Abhari. Employing EBG Structures in Multiantenna Systems for Improving Isolation and Diversity Gain. *IEEE Antenna Wireless Propagat. Lett.*, 8:1162–1165, 2009. 121

Appendix A

Numerical Characterization of artificial engineered structures

The general procedure for analyzing an artificial structure is to initially perform a full-wave simulation of the artificial unit cell in order to determine the scattering matrix components, or the *S-parameters*, which are related to the reflection and transmission coefficients as shown in Fig. A.1.

Then, the refractive index, n, and the impedance, Z, are determined through an S-parameter inversion given by [109], [113]

$$Z_{eff} = \pm\sqrt{\frac{(1+S_{11})^2 - S_{21}^2}{(1-S_{11})^2 - S_{21}^2}}, \tag{A.1}$$

$$e^{(-jn_{eff}k_0d)} = X \pm j\sqrt{1-X^2}, \tag{A.2}$$

$$X = \frac{1}{2S_{21}(1 - {S_{11}}^2 + {S_{21}}^2)}, \tag{A.3}$$

where d is the artificial unit cell dimension. Note that since the artificial materials considered here are passive media, the signs in A.1 and A.2 are selected such that $Real(Z_{eff}) > 0$ and $Im(n_{eff}) < 0$, where *Real* and *Im* are the real and imaginary parts of the effective impedance Z_{eff} and refractive index n_{eff}, respectively.

Then, the effective constitutive parameters ϵ_{eff} and μ_{eff} are computed using

$$\mu_{eff} = n_{eff}Z_{eff}, \tag{A.4}$$

and

$$\epsilon_{eff} = \frac{n_{eff}}{Z_{eff}}. \tag{A.5}$$

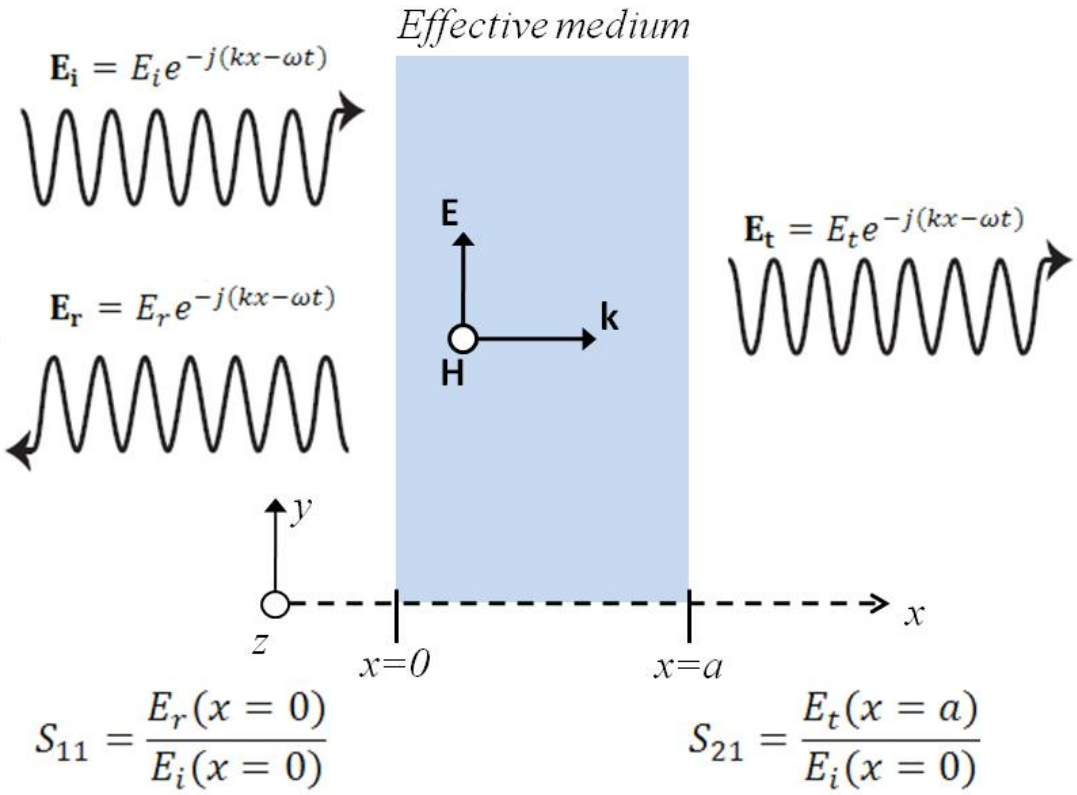

Figure A.1: The equivalent effective medium model used to retrieve the effective constitutive parameters from the scattering parameters. The unknown material is assumed infinite in both y and z directions.

Appendix B

Surface Waves Calculation on Grounded Dielectric Slab

Surface waves are typically those waves that decay exponentially away from dielectric/air interface with most of the field propagating along the dielectric surface. Such waves can usually occur in the interface between two dissimilar materials. In this appendix, surface wave fields on typical grounded dielectric slabs are analyzed. By calculating the electromagnetic fields existing in such structures, the possible surface wave modes can be solved for numerically.

Fig. B.1 depicts the guiding structure under study, consisting of two regions: grounded dielectric slab and the air (free-space) region interfaced with the dielectric slab. In order to solve for the possible surface waves, the fields are separately considered in each region, and then boundary conditions are applied along the interface. The transverse magnetic (TM) case is considered here and the TE case can be solved for in a similar manner.

Assume that the propagation direction is the z-axis and there is no variation along

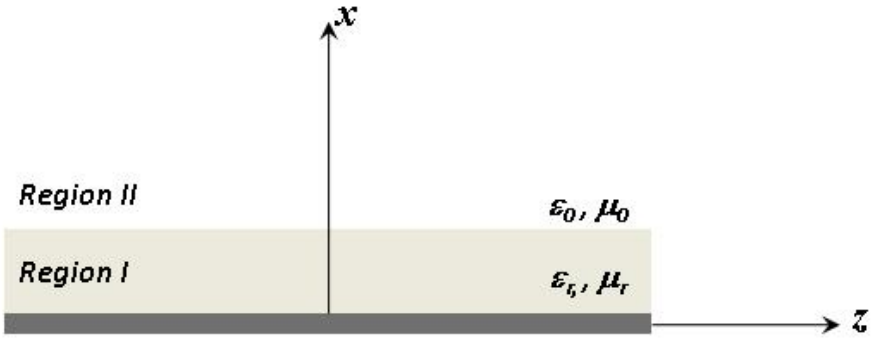

Figure B.1: Typical grounded dielectric slab.

the y-direction ($\frac{\partial}{\partial y} = 0$). The electric field E_z must satisfy the wave equation in each region as

$$(\frac{\partial^2}{\partial x^2} + \epsilon_r k_0^2 - k_z)E_z = 0, \text{for } 0 \leq x \geq d \tag{B.1}$$

$$(\frac{\partial^2}{\partial x^2} + k_0^2 - k_z)E_z = 0, \text{for } d \leq x \geq \infty \tag{B.2}$$

where E_z=$e_z e^{-jk_z z}$, and the wavenumbers in each region are

$$k_c^2 = \epsilon_r k_0^2 - k_z^2 \tag{B.3}$$

$$h^2 = k_z^2 - k_0^2 \tag{B.4}$$

By adding B.3 and B.4, one gets the following relation

$$k_c^2 + h^2 = \epsilon_r k_0^2 - k_0^2 = (\epsilon_r - 1)k_0^2, \tag{B.5}$$

which is in the form of a circle.

The boundary conditions needed are

$$E_z(x, y, z) = 0, \text{at } x = 0 \tag{B.6}$$

$$E_z(x, y, z), \text{is finite as } x \to \infty \tag{B.7}$$

and the continuity of both electric and magnetic fields along the interface, x=d.

The solutions to B.1-B.2 can be expressed as

$$E_z = Acos(k_c x) + Bsin(k_c x), \text{for} \leq x \geq d \tag{B.8}$$

$$E_z = Ce^{-hx} + De^{hx}, \text{for } d \leq x \geq \infty \tag{B.9}$$

Applying the boundary conditions at x=0 and along the interface x=d, the following relations are obtained,

$$Bsin(k_c d) = Ce^{-hd}, \tag{B.10}$$

$$\frac{\epsilon_r B}{k_c} cos(k_c d) = \frac{C}{h} e^{-hd}, \tag{B.11}$$

In order to solve for the propagation constants within the guiding structure, the determinant of B.10-B.11 must be zero. Doing so, one arrives at the following relation

$$k_c tan(k_c d) = \epsilon_r h. \tag{B.12}$$

After solving for B.12 and B.5 simultaneously, the possible propagation constants in the two regions can be obtained in terms of ϵ_r and the free-space wavenumber k_0. For this particular case, newton raphson, a root-searching algorithm, has been adopted. A

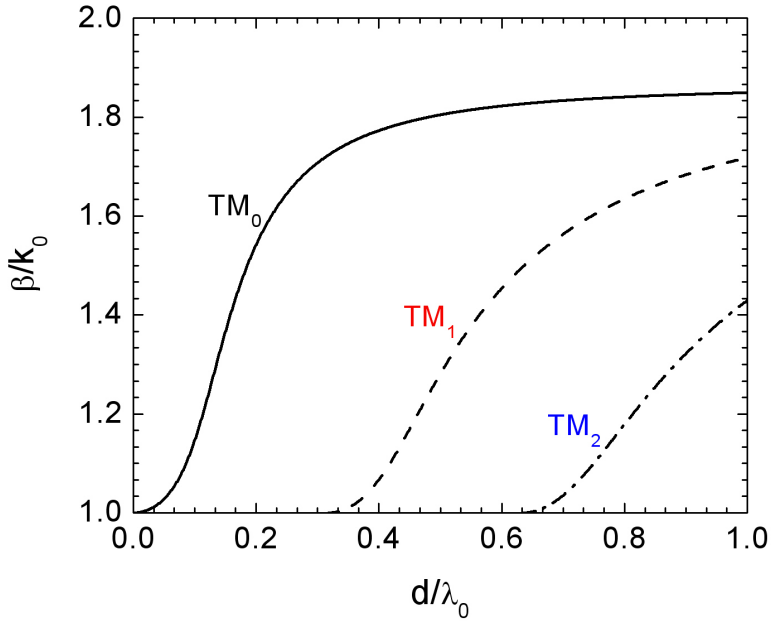

Figure B.2: TM surface wave modes on grounded dielectric slab as function of normalized thickness d/λ.

MATLAB code was implemented to find the propagation constants of the surface wave modes.

Fig. B.2 shows a set of possible TM surface waves propagation constants on the grounded dielectric slab ($\epsilon_r = 3.48$) as function of the normalized dielectric thickness, d/λ, where λ is the operating wavelength. The first mode, TM_0, has no cut-off frequency and thus always present for any dielectric slab thickness. The next TM surface wave mode exists at a thickness d = 0.26λ.